2017

Elucidation Of Protein Interactions And The Re-Tuning Of Porphyrin Electronics For Hydroxylases

Steven Charles Ratigan
University of South Carolina

Recommended Citation

Ratigan, S. C.(2017). *Elucidation Of Protein Interactions And The Re-Tuning Of Porphyrin Electronics For Hydroxylases.* (Doctoral dissertation). Retrieved from https://scholarcommons.sc.edu/etd/4482

ELUCIDATION OF PROTEIN INTERACTIONS AND THE RE-TUNING OF PORPHYRIN ELECTRONICS FOR HYDROXYLASES

by

Steven Charles Ratigan

Bachelor of Arts
The Citadel, 2005

Bachelor of Science
University of South Carolina, 2009

Master of Arts
The Citadel, 2012

Submitted in Partial Fulfillment of the Requirements

For the Degree of Doctor of Philosophy in

Chemistry

College of Arts and Sciences

University of South Carolina

2017

Accepted by:

Thomas Makris, Major Professor

F. Wayne Outten, Committee Member

John Lavigne, Committee Member

Zhengqing Fu, Committee Member

Cheryl L. Addy, Vice Provost and Dean of the Graduate School

DEDICATION

I dedicate this work to my family, who have always been there for me. Without their support, my time in academia would have been much more difficult.

I would also like to thank Dr. David Donnell of The Citadel Dept. of Biology for teaching me everything I know about molecular biology, which proved to be a huge help early on in this program.

ACKNOWLEDGEMENTS

I would like to thank my mentor Dr. Makris for attempting to patiently deal with me for six years in this program. While I swore I would never be one of those people to sum things up with a generic quote, I'm going to do it anyway with "It was the best of times, it was the worst of times" - Charles Dickens

I would also like to thank my fellow labmates. My early years were spent with two very interesting science personalities in Job Grant and Jason Hseih. Job nailed down a framework for analyzing high-valent intermediates in wild-type P450olet and Jason's aminoacyl-CoA was the only batch anybody has been able to make since. Next came Jose Amaya who brought the chill to the lab and basically nailed down a framework for turnover analysis for my GC work. Courtney Wise, one of my former undergrads, followed Jose and dutifully wrote down, in excruciating detail, the procedures for doing anything in the lab. Finally, Olivia Manley arrived a little too late for knowledge to pass either way, but I think she'll figure her stuff out.

I would also like to thank Julia Bian, the only other undergrad that I mentored (besides Courtney) that it has been true honor to work with.

ABSTRACT

Non-Ribosomal Peptide Synthetases (NRPSs) and their exogenous tailoring partners have been heavily studied but not in the context of non-cognate systems. Orf78, a dinuclear iron β-hydroxylase from the lysobacter pathway and homologous to CmlA from the chloramphenicol pathway, is used to test affinities for one native and two non-native T-domains. Results indicate that there is enough difference between Type I and Type II NRPS systems to disfavor common recognition motifs. Additionally, the β-hydroxylase P450sky, from the skyllamycin biosynthetic pathway, is used in conjunction with the NRPS AT-domain NikP1AT from the nikkomycin biosynthetic pathway, in lieu of the homolog P450nikQ. The second portion of the thesis will discuss the creation of a sustainable source of biodiesel products are currently a goal of 'green' programs. The fatty acid decarboxylase P450olet uses the cheaply obtainable hydrogen peroxide as the oxidant to achieve a high-valent iron species. Substitution of the iron for manganese in the porphyrin scaffold raises the redox potential and forms a Mn(IV)-oxo complex that is too weak to perform C-H bond abstractions. Alternatively, substitution of the iron-protoporphyrin IX with iron-mesoporphyrin IX lowers the redox potential, increasing the amount of hydroxylated fatty acid at lower carbon chain lengths but also leads to a decrease in the efficiency in multiple turnover reactions.

TABLE OF CONTENTS

LIST OF TABLES

LIST OF FIGURES

CHAPTER 1

A COMPARISON OF PCP DOMAINS AND THEIR RECOGNITION WITH A DINUCLEAR IRON HYDROXYLASE FROM THE LYSOBACTIN BIOSYNTHETIC PATHWAY

1.1 INTRODUCTION

The necessity to diversify the antibiotic arsenal has never been as crucial as it is now with the current level of antibiotic resistant bacteria causing problematic issues in the realm of public health, particularly *Streptococcal* and *Staphylococcal* species [1-3]. Although attempts are currently being pursued through synthetic means [4-6], the production of more complex antibiotics may be cost-prohibitive, if not synthetically unachievable. One potentially viable route is through modification of the antibiotic machinery, known as non-ribosomal peptide synthetases (NRPS). Such efforts may create opportunities to synthesize a library of compounds built around a structural scaffold that can be subsequently screened for antimicrobial activity. Specifically, the use of a pre-existing NRPS complex, a protein megastructure that produces peptide-based antibiotics through an assembly-line process, may provide a useful tool for the incorporation of non-cognate tailoring enzymes as a means for producing modified versions of current antibiotics. This method has not gained widespread popularity due to its trial-and-error approach and its typically low-yields of product [7]. Alternatively, entire operons have been transplanted from one organism to another with successful production of antibiotic. Although providing new biological platforms for synthesis, pathogenic bacteria may have already developed resistance to these natural products [8]. There has been very little research involving the transplantation of enzymes from one antibiotic biosynthetic pathway to another to generate new products. Homologous enzymes must be identified and characterized to determine their suitability for a non-ribosomal peptide synthetase (NRPS) system that is not natively recognized.

Reviews by Marahiel group give an in-depth explanations of how an NRPS is formed and how they function to create an antibiotic product [9, 10]. Briefly, a NRPS is a modular complex with each module involved with the identification and activation of a particular amino acid that ultimately becomes incorporated into a nascent peptide chain. These modules are further divided into individual domains which are each responsible for a specific aspect of the identification, modification, and transfer of the amino acid into the nascent peptide chain. In a canonical multimodular NRPS system, a single module contains three domains: the Adenylation (A) domain identifies and activates a specific amino acid through an adenylation reaction, the Thiolation (T or PCP) domain tethers the activated amino acid through a thioester bond onto a post-translationally transferred phosphopanthetheine (ppant) and transports the substrate between domains, and the Condensation (C) domain which extends the nascent polypeptide chain. One interesting deviation from this operation that will be discussed here is the modification of the tethered substrate by enzymes that operate *in trans* to the NRPS, such as the β-hydroxylases CmlA and $P450_{sky}$, providing a method to diversify the final product.

The recognition event may depend on either ionic or hydrophobic binding domains present on the surfaces of the enzyme and the T-domain, enzyme specificity for the tethered amino acid, or a combination of both. P450 hydroxylases that operate in this fashion, such as $P450_{NikQ}$ and $P450_{sky}$, are reported to rely on hydrophobic interactions to properly recognize the binding motif of the NRPS, although these residues have yet to be fully elucidated [11, 12]. However, there is potential for greater product diversity if these binding motifs can be solved and incorporated into modules of an NRPS that incorporate non-modified amino acids, allowing for the creation of modified products. The β-hydroxylase Orf78, associated with the lysobactin biosynthetic pathway, is homologous with CmlA from the chloramphenicol biosynthetic pathway. However, the uniqueness of Orf78 lies with its ability to recognize and hydroxylate substrate attached to three individual NRPS modules instead of the singular modification conducted by CmlA. Study of the similarities and recognition flexibilities between the hydroxylase binding motifs will be conducted through comparisons of interactions between Orf78 and native and non-native T-domains and gathering information necessary to successfully modify an NRPS pathway to create a familiar but unique antibiotic-like compound.

Lysobactin is a depsipeptide-based antibiotic isolated from *Lysobacter* sp. SC 14067 (ATCC 53042) [13, 14] (Figure 1.1, bottom). In its biologically active form, it binds to the D-Ala-D-Ala unit of Lipid II during the bacterial biosynthesis of peptidoglycan and inhibits the synthesis of new cell wall in gram-positive bacteria [15]. The inability for the bacteria to synthesize a new cell wall decreases its overall robustness, allowing turgor pressure to weaken the cell from within and ruptures in the cell membrane. This mechanism of bacteriocide places lysobactin in the same category as vancomycin [16] and similar derivatives, such as teixobactin [17] and balhimycin [18]. However, the importance of lysobactin lies in in the fact that its minimum inhibitory concentration is one quarter of vancomycin's on gram-positive bacteria [13], with its strength leading to lower dosages and the hope of a prolonged lifetime prior to eventual ineffectiveness due to the evolution of antibiotic-resistant strains of gram-positive bacteria. Due to the inhibitory effects of the drug to Lipid II, there is no activity towards mammalian cells, making the drug a possible candidate for use against troublesome gram-positive bacteria common in hospitals, such as *Staphylococcus aureus* and *Streptococcus pneumoniae*.

The lysobactin NRPS biosynthesis pathway is organized into eleven modules segregated into two genes, with hydroxylation of two modules on LybA associated with hydrophobic substrates (Phe3 and Leu4) and one module on LybB associated with a weakly acidic substrate (Asn10) [19] (Figure 1.1, top). This contrasts with CmlA, which solely hydroxylates the hydrophobic non-native amino acid L-para-aminobenzoic acid (L-PABA) [20]. This also differs from $P450_{sky}$, a hydroxylase with a heme cofactor that hydroxylates three modules on the skyllamycin biosynthetic pathway associated with three hydrophobic substrates (PCP_{Phe5}, PCP_{Tyr7}, and PCP_{Leu11}) [21]. For Orf78, the diversity of recognized charges on the substrate side-chain may allow for greater flexibility for recognition than with other β-hydroxylases; however, the reasons why some amino acids are hydroxylated while others are not is unclear. The structure of the antibiotic shows the β-hydroxyl group on PCP$_{\text{Phe3}}$ is necessary to form an intermolecular lactone with the C-terminal carboxylate of the nascent peptide chain. However, it is unknown what functions the β-OH groups on PCP$_{\text{Leu4}}$ and PCP$_{\text{Asn10}}$ serve, except at the very least assisting to solubilize the active compound, which is mostly hydrophobic in nature.

Makris *et al*. showed that oxidation kinetics on Type I NRPS systems (CmlA/CmlP$_{\text{AT}}$) can be used as an indirect measurement to determine binding of the substrate carrier to the hydroxylase, with quicker rates indicative of greater oxygen access to the active site of the enzyme [20]. For heme-bound hydroxylases, the dissociation constants with Type II NRPS systems (P450$_{\text{sky}}$/PCP7$_{\text{O-Me-Tyr}}$) [12, 20] were used to show the differences between bound and unbound substrate carriers. However, there is no information concerning cross-recognition for a Type II-associated hydroxylase with non-native Type I or II NRPS systems. Following basic characterization of Orf78, to include iron quantitation and structural features, a comparative analysis of oxidation kinetics between Orf78 and modular components from three different systems will be performed, utilizing the following T-domains: PCP$_{\text{Asn10}}$ from the lysobactin system, CmlP$_{\text{T}}$ from the chloramphenicol system, and PCP$_{\text{Phe6}}$ from the teichoplanin system.

1.2 MATERIALS AND METHODS

Cloning

The *orf78* gene was cloned from the genomic template from Lysobacter sp. 53042 (ATCC). The following primers were utilized for the amplification of the *orf78* gene with Taq polymerase (NEB), where the capitalized regions are the restriction sites for SfaAI and MssI:

forward - 5’-ccatatg*GCGATCGC*caataccactca-3’

reverse - 5’-ccatatg*GTTTAAAC*tcacagaagcag-3’

The amplicon and pVP91A vector were both digested with SfaAI and MssI (Thermo Fisher Scientific), gel-purified, and ligated with T4 DNA ligase (NEB). The insert was verified using the facilities at ACGT, Inc.

The PCP_{Asn10} gene was similarly cloned from the genomic template of Lysobacter sp. 53042 (ATCC). The following primers were utilized for the amplification of the A10T gene with Q5 polymerase (NEB), where the capitalized regions are the restriction sites EcoRI and HindIII:

forward - 5'- cgtatc*CATATG*ctgctgtcgccgccgcagcgcgag -3'

reverse - 5'- cgtatc*AAGCTT*cgccggcaacgccgccccgc -3'

The amplicon and pET21b(+) vector were both digested with EcoRI and HindIII (NEB), gel-purified, and ligated with T4 DNA ligase (NEB). The sequence was verified using the facilities at ACGT, Inc.

Protein Expression and Purification

The *Orf78* plasmid was chemically transformed into BL21(Dε3) cells. A single colony was used to inoculate a starter culture which were used as inoculant for 1 liter flasks of M9 minimal media. The components of the M9 minimal media consists of: 200 mL M9 salts, 2 mL of 1 M $MgSO_4$, 20 mL of 20% glucose, 100 µL of 1 M $CaCl_2$, 12 mL overnight culture, and 1 mL of 100 mg/mL Ampicillin. The culture was induced at an OD_{600}=0.7 with the addition of 150 µM isopropyl β-D-1-thiogalactopyranoside (IPTG; RPI corp.) supplemented with 50 µM $FeCl_3$ with further incubation for 16 hours at 18^{o}C. The cells were lysed, cleared, and purified with Ni-NTA resin equilibrated with 50 mM sodium phosphate, monobasic, 300 mM sodium chloride, pH=7.5, 10 mM imidazole (Buffer A), washed with Buffer A + 10 mM imidazole, and eluted with Buffer A+240 mM imidazole. Following purification, the eluent was dialyzed overnight in 50 mM HEPES, pH=7.5 + 10% glycerol. The protein was concentrated, aliquoted, and stored at -80^{o}C.

The *PCP*$_{Asn10}$ plasmid was chemically transformed into BL21(Dε3) cells. A single colony was used to inoculate a starter culture which were used as inoculant for 1 liter flasks of Luria-Bertani media. The culture was induced at OD_{600}=0.6 with 150 µM IPTG followed by incubation for an additional 16 hours at 37^{o}C. The cells were lysed, cleared, and purified with Ni-NTA column equilibrated with Buffer A, washed with Buffer A + 10 mM imidazole, and eluted with Buffer A + 240 mM imidazole followed by dialysis overnight in 25 mM HEPES, pH=7.5. The dialysate was subsequently loaded onto DEAE resin equilibrated with 25 mM HEPES, pH=7.5. The flow-through, which contains the properly-folded protein, was dialyzed in 100 mM HEPES, pH=7.5, 30% glycerol prior to concentrating, aliquoting, and storage at -80^{o}C.

Size Exclusion Chromatography

Nine milligrams of Orf78 were loaded onto an S-200 size-exclusion column attached to an ATKA FPLC equilibrated with 50 mM HEPES, pH=7.5 and eluted at 0.3 mL/min. The elution profile was matched with a set of protein standards with known molecular weight to determine the oligomeric state of the enzyme.

UV-Vis

All UV-Vis measurements were obtained on an Agilent 8453 UV-Vis spectrophotometer and analyzed on Agilent proprietary software or the OriginPro software package. The concentration of Orf78 was calculated using Beer's Law and the theoretical ε_{280} = 58.8 mM^{-1}cm^{-1}. An azide assay was used to determine the presence of any diiron cluster within the enzyme. 50 µM of Orf78 was incubated in 1 mL of 50 mM HEPES, pH=7.5, 8 M sodium azide for 20 minutes at 4^{o}C. The solution was cleared by centrifugation at 4^{o}C and spectrum taken of the supernatant at 340 nm and 420 nm.

A reductive titration was performed to determine the number of electrons necessary to fully reduce the enzyme from the fully oxidized state. All solutions were buffered in 50 mM HEPES, pH=7.5 degassed with N_2. A 2 mM solution of sodium dithionite was utilized as a reductant. Separately, a solution of 50 uM Orf78 was prepared in an anaerobic cuvette with the addition of 0.5 molar equivalents of methyl viologen. Sodium dithionite was titrated with a gas-tight syringe in 30 µM increments until the charge-transfer band at 340 nm completely bleached and the methyl viologen absorption peaks from 350-395 nm became apparent, indicating full reduction of the enzyme. The data was analyzed on OriginPro 2016 as a plot showing number of electrons against total absorbance at 340 nm.

Electron Paramagnetic Resonance (EPR)

Spectra of the mixed-valent enzyme were collected on an EMXplus X-band EPR (Bruker) at 10K with 5 mW power and a microwave frequency of 9.834 GHz. Each spectrum is a composite of 15 averaged scans per sample. The data were collected and analyzed on either the Bruker Xenon software suite or the SpinCount software package. Determination of the g-values were performed by the use of the equation g = (71.4484v) / B, where magnetic field, B (mT) and the microwave frequency, v (GHz). All solutions were buffered in 50 mM HEPES, pH=7.5 and degassed with N_2. Sample preparation was performed anaerobically with O_2 levels less than 1 ppm.

The visualization of the mixed-valent species involved the preparation of four samples. The sample containing one electron-equivalent to create the mixed-valent species involved the addition of 250 µM sodium dithionite to 400 µL of 400 µM degassed Orf78 + 200 µM methyl viologen and incubated until the solution transformed from purple to clear. The solution was transferred to a quartz cuvette, capped, and frozen in liquid nitrogen for storage. For the formation of the partial mixed-valent species by the addition of 0.8 electron-equivalents, 200 µM of sodium dithionite was added to 400 µM Orf78 + 200 µM methyl viologen and stored as above. For samples containing no mixed-valent species from 0.4 electron-equivalents, 400 µM Orf78 + 200 µM methyl viologen were immediately frozen and stored. For samples containing no mixed-valent species from two electron equivalents, 400 µM sodium dithionite was added to 400 µM Orf78 + 200 µM methyl viologen and frozen off for storage.

Alteration of the temperature can determine the protonation state of the oxygen bridge between the two iron molecules. The mixed-valent species from the fully mixed-valent sample above was measured at a constant power of 5 mW and all spectra are an average of 15 scans. Measurements were taken at temperature points at 4K, 16K, 25K, and 39K.

The sample with highest content of the mixed-valent form was subsequently used for the power saturation experiment. The temperature was kept at a constant temperature of 8K ± 0.75K and the power was increased from 0.07942 mW to 158.9 mW, with each spectrum representing the average of 15 scans. The distance, from peak to trough, of the second g-value was used as a measure of the signal intensity (I) at any given power. The power at half-saturation ($P_{1/2}$) was determined using the following equation:

$$I = I_o * P_{1/2}/(1+P/P_{1/2}))^{b/2}$$

, where I_o is the intensity under unsaturated conditions and b is a homogeneity value assumed to be equal to 1. The data was plotted as log(I/√(P)) as a function of power (mW).

Synthesis of Coenzyme-A derivatives

Bodipy-CoA was synthesized by dissolving 110 nanograms each of Bodipy-FL (Life Technologies) and Coenzyme A (CoA; RPI corp.) in 300 µL DMSO + 1.8 mL 75 mM MES, pH=6 + 100 mM magnesium acetate. The solution incubated on ice in a dark environment for 10 minutes followed by incubation at room temperature in a dark environment for 2 hours while rapidly stirring. Pure product was isolated with several extractions of ice-cold diethyl ether. Excess ether was evaporated under N_2 prior to aliquoting and storage at -20^{o}C.

Synthesis of Phe-CoA involved dissolving 5 mg of Boc-Amino Acid (AA), 4 mg dicyclohexylcarbodiimide (DCC, Sigma Aldrich), and 3 mg N-hydroxysuccinimide (NHS, Sigma Aldrich) with 1 mL acetonitrile and incubating on ice for 10 minutes prior to stirring at room temperature for 24 hours under a nitrogen atmosphere. Following the incubation time, 15 mg of CoA dissolved in 1.5 mL of 40 mM lithium carbonate were added to the solution and incubated on ice for 5 minutes prior to further incubation at room temperature for an additional 2 hours. The addition of H_2O:TIPS:TFA at a ratio of 2.5:2.5:95 was added to deprotect the amine group of the Boc-AA-CoA and the solution was allowed to stir at room temperature for 2 additional hours. The Phe-CoA was purified by several extraction steps with ice-cold diethyl ether, resulting in the precipitation of the desired product. The precipitated product was isolated via centrifugation, dried under N_2, and resuspended in dH_2O to a concentration of 2.5 mM, aliquoted, and stored at -20^{o}C.

SfP recognition of the T-domain

The Phe-PPant is transferred to the T-domain with a 4´-phosphopantetheinyl transferase (SfP) derived from *Bacillus subtilis* and expressed in *E. coli*. After the T-domain is purified, Bodipy-PPant is transferred to test for SfP recognition of the serine residue, as part of the GGxS motif. The reaction is set up with 30 mM magnesium chloride, 60 mM Tris, pH=8.0, 700 mM AA-CoA, 5 µM SfP, and 200 µM apo-PCP$_{\text{Asn10}}$ followed by incubation at room temperature for 1 hour and desalting in 50 mM HEPES, pH=7.5. The sample is then run on a 12% SDS-PAGE gel and, upon completion, viewed under a transilluminator to verify its presence at ~10kDa. If the SfP recognizes the T-domain, then the same procedure is used to transfer Phe-PPant for use in Stopped-flow experiments.

Stopped-flow

Binding between Orf78 and any T-domain was determined by the rate of rebound for the iron-oxo charge-transfer band at 340 nm from the bleached reduced state to its re-emergence when oxidized. The measurement of the oxidation rates for the hydroxylase/NRPS complex was performed on an SX20 Stopped-flow spectrophotometer (Applied Photophysics) for accurate visualization and rate measurements. The temperature of the experiment was set to 4^{o}C and data was collected utilizing a PMT detector set at 340nm with 5000 time points over 500 seconds per measurement.

Syringe A contained 50 µM Orf78 + 25 µM methyl viologen that was fully reduced with excess dithionite in an anaerobic bag and desalted to remove any small molecules. The solution was then transported anaerobically and loaded into the stopped-flow pre-chilled at 4°C. Syringe B contained 50 mM HEPES, 2 mM O_2, and one of the following: apo- PCP_{Asn10}, holo- PCP_{Asn10}, Phe-PCP_{Asn10}, Phe-CmlPAT from the chloramphenicol NRPS, or Phe-PCP_{Tyr6} from the teichoplanin NRPS. The collected data was an average of triplicate traces for each sample and fit to single exponential functions to determine the final rates in Pro-Data Viewer (Applied Photophysics).

1.3 RESULTS

Orf78 contains a dinuclear iron cluster

An analysis of the sequence alignment shows the endogenous ligands present in CmlA are fully conserved in Orf78 (Figure 1.2). A model of Orf78, created using SWISS-MODEL [22] and the published structure of CmlA (PDBID: 4JO0) as a template, putatively confirms an overlap for all residues involved in the ligation of the metal atoms. The first coordination sphere consists of three His, two Glu, and two Asp residues, with one of the Asp forming a µ-1,1 carboxylate bridge between the two irons in the cluster. The presence of a carboxylate bridge is not uncommon, but the bridge is not usually a µ-1,1 configuration, but rather a µ-1,3 carboxylate linkage. Crystallographic studies of other diiron enzymes show at least one µ-1,3 carboxylate bridge, such as the case with Methane Monooxygenase (MMO), Purple Acid Phosphatase (PAP), and Ribonucleotide Reductase (RNR) [23-25]. Specifically, the crystal structure of CmlA confirms the presence of residue D403 forming a µ-1,1-carboxylate bridge between the active site irons. However, the structure also shows the presence of an adventitious acetate anion present from the mother-liquor that may be displacing D403 into a conformation forming a mono-dentate rather than bi-dentate bridge. It is worth noting that this same acetate anion may be responsible for displacing residue D430, which is a viable ligand in range of an iron atom. However, it is unknown whether a similar bridge or solvent ligation pattern is present in Orf78, as attempts to crystallize the protein have been futile.

In similar fashion to that proposed for CmlA, Orf78 purifies as a dimer with two joined 60.8 kDa units (Figure 1.3). Size-Exclusion Chromatography shows the protein elution at around 125 kDa with no peaks associated with monomeric or other oligomeric forms of the enzyme. The crystal structure for CmlA suggests the dimer interaction is derived from a dimerization arm that electrostatically interacts with the same domain on the opposing monomer in a hook-like fashion separate from the active site region of the jelly-roll motif. Similar residues are present at the dimer interface of the model for Orf78, inferring the nature of the dimerization is electrostatic in nature as well.

Iron quantitation with the ferrozine assay consistently yields 1.7-2.3 irons per dimer. These results were confirmed with ICP-MS and show only trace amounts of manganese, zinc, and copper present in the sample. However, the fully-loaded metal count for the dimer should be around four irons per dimer since each active site in the dimer requires occupancy by two iron molecules. Given the minimal media growth conditions supplemented with ample iron (III) chloride, it is not known why complete loading does not occur. Metal reconstitution experiments in both aerobic and anaerobic conditions have also been unsuccessful. Nonetheless, the lack of an appreciable high-spin Fe3+ signal in the as-isolated enzyme, reductive titration of Orf78 with sodium dithionite, and the presence of a mixed-valent signal in EPR demonstrates that almost all of the irons are bound as a cluster.

The UV-Vis spectrum of Orf78 consist of a broad spectral region with weak extinction coefficients extending from 300-450 nm, culminating in a major peak maximum at 340 nm and a minor peak maximum at 420 nm. Similar peaks are observed in other hydroxo-bridged diiron enzymes like CmlA [20], and Hemerythrin (Hr) [26] when in a low-spin, diferric state. The peak at 340 nm manifests through the electronic charge-transfer exchange by the Fe_2-O, which is created by splitting the π-orbital electrons resonating between the two iron atoms via an oxo-bridge [27]. The intensity of the bands is less significant than those of proteins with oxo-bridges, indicating that resonance is weaker due to the oxo-bridge being protonated. An Fe_2-O bridge that forms in a linear fashion will usually absorb at 420 nm and 500 nm. However, at the more acute angles of 114^o to 130^o, the lowest Fe_2-O π-transition state at 500 nm blends with the second lowest state at 420 nm, indicating a less-obtuse bridge form is present with Orf78 [28].

Titrating sodium dithionite to the protein, and subsequent reduction of the diferric cluster, decreases the intensity of the 340 nm and 420 nm peaks, leading to bleaching of the charge-transfer signal through the quenching of its π-orbital resonance effects (Figure 1.4). Reduction is quick, inferring minimal difficulty for electron access to the active site of Orf78. The oxidation of Orf78 from the diferrous state mimics CmlA and human dehydroxypusine hydroxylase by fully oxidizing to the diferric state as observed by a rebound of the bleached 340 nm and 420 nm charge-transfer bands [29]. However, Stopped-flow data shows that oxidation of Orf78 from the diferrous state in the presence of molecular oxygen is a slow process, suggesting difficulty for the molecular oxygen cofactor to gain access to the active site. This, in addition to an increased rate in the presence of Phe-PCP$_{\text{Asn10}}$, suggests the presence of necessary events prior to the activation of O_2 by the reduced enzyme.

The introduction of sodium azide to diferric Orf78 forms an additional π-stabilized bridge, leading to an increase in absorbance for the 340 nm and 420 nm bands (Figure 1.5). Similar spectra are observed with biological non-heme diiron enzymes, such as metHr and Hr [27], and synthetic constructs [30]. However, the concentration requirements of sodium azide necessary for bridge formation is four-fold higher than required for CmlA and binding is not immediate, requiring incubation at 4^oC for longer periods to time to observe maximum peak amplitudes. Two possible reasons for this is that access to the active site for azide is restrictive or the distance between the two iron molecules is not optimal to facilitate formation of the azide bridge.

The EPR spectrum of the diferric state does not induce a signal, which confirms that Orf78 is a S=5/2-5/2 anti-ferromagnetically spin-coupled system (Figure 1.6, top right). The absence of a signal at g=4.3 shows that there is both little free iron in the sample and also that the two irons are not separate S=5/2 systems [31]. Incubation with 0.5 molar equivalents of sodium dithionite produces a S=5/2-2 spin-coupled system with an orthorhombic mixed-valent signal and observable values of g_z=1.96 and g_y=1.86 at low temperature (Figure 1.6, top left). These values are observed in other anti-ferromagnetically spin-coupled systems, like RNR, when one-electron equivalent is added to the diferric enzyme [32]. The g_x value is not observed, presumably blending into an extended g_y signal. This behavior is also observed in the mixed-valent signal for CmlA. There is no signal when the sample is reduced with two-electron equivalents to a diferrous state, indicating a S=2-2 spin-couple. This reinforces the conclusion that the cluster is anti-ferromagnetically coupled since it is also observed in similarly spin-coupled systems, such as MMO and Hr [33, 34].

The intensity of the mixed-valent EPR signal for Orf78 shows a temperature-dependent that suggests the presence of a hydroxo-bridge between the two iron molecules (Figure 1.6, bottom left). Increasing the temperature from 4K to 18K does not significantly alter the amplitude of the signal. However, the signal decreases as the temperature is increased above 18K and is ultimately lost beyond 39K. Similar tendencies are observed in other hydroxo-bridged diiron proteins, like CmlA, MMO, and PAP, which have decreased relaxation times due to the increased acidity of the associated irons [35]. The presence of an oxo-bridge would increase the relaxation time of the π-electron transfer between the two iron atoms, preventing decay of the mixed-valent signal until higher scan temperatures (>100K) are achieved [36].

Changes to the local environment, such as the presence of substrate or cofactors, may alter the sensitivity of the relaxation state for the mixed-valent diiron species and observed through power saturation studies [37]. As the power increases, the relaxation state of the electrons sit at a higher energy level and the signal decreases. Power saturation is also informative for determining what power should be used to measure any EPR spectra so there is a reduction in unwanted g-value broadening and signal reduction. For Orf78, a plot of the power saturation curve shows a $P_{1/2}$ equal to 93.2mW ± 8.6mW (Figure 1.7), so a high amount of power is needed to saturate the signal at 10K and overcome the relaxation times of the mixed-valent signal. Plotting ln($P_{1/2}$) for this value as a function of temperature (K^{-1}) gives a value of 4.53 at 10K, which is slightly higher than CmlA (~3.8) and the hydroxo-bridged diiron Mitochondrial Alternative Oxidase (~4.9) [20, 38]. The values are assumed to be close enough to associate similar power saturation values of Orf78 for all temperature ranges. Ideally, more points would be preferred, but the slope, and the corresponding J value, of the plot can be inferred due to the homology of the two enzymes and is assignable as a hydroxo-bridge in the mixed-valent form.

Similarity of PCP domains

Three PCPs for the lysobactin biosynthetic pathway, PCP_{Phe3}, PCP_{Leu4}, and PCP_{Asn10}, provide substrate that are all β-hydroxylated prior to their incorporation into the nascent peptide chain. A protein sequence alignment (Clustal Omega) of the three contain a sequence identity of 40%-60% (Table 1.1). It has been theorized that this is due to gene duplication followed by mutation of pre-existing modules, creating a useful and cheap mechanism to expand the library of NRPS products [39, 40]. However, the three PCP domains that facilitate β-hydroxylation of amino acids in the skyllamycin biosynthetic pathway (incorporated in *sky30* and *sky31*) have a sequence identity of 38%-60% [21]. Although the identity range is wider than the lysobactin pathway, variations for both systems are mostly localized in the flanking regions of the four-helix bundle of the PCPs. It is unclear what effects these flanking regions have on the overall function of the module or their role in recruiting their respective β-hydroxylases. Incorporation of $\mathrm{PCP}_{\mathrm{Phe6}}$, the only PCP in the teicoplanin biosynthetic pathway (incorporated in *dbv17*) that is β-hydroxylated by the diiron hydroxylase Orf12, into the sequence alignment with the lysobactin PCPs lowers the sequence identity to 30% [41]. However, a strong conservation of residues exists within the core regions containing helices α2 and α3, which are presumed to contain the binding motifs to the hydroxylase. Modeling the three PCPs from lysobactin to the PCP from teichoplanin illuminate overlaps across all four helices, suggesting that the PCPs for both systems adopt similar four-helix bundles in their active forms (Figure 1.8).

Insertion of $\mathrm{CmlP}_{\mathrm{T}}$ from the Chloramphenicol biosynthetic pathway (incorporated in *orf8*) [42], a Type II NRPS which contains a β-OH L-PAPA, into the sequence alignment with the four Type I PCPs drops the sequence identity to 20%. The homology among all five T-domains also exemplifies this, as there is a large drop-off in similarity upon the addition of the $\mathrm{CmlP}_{\mathrm{T}}$ PCP (Figure 1.9). A model of $\mathrm{CmlP}_{\mathrm{T}}$ with any of the Type I PCPs above show incompatibility with the Type II systems, as the conformation adopts a two-helix bundle in lieu of four. The main discrepancy is the presence of random coil, which did not conform to the outfitted model, so does not conform to the four helix motif for the Type I systems. This may infer that hydroxylases from Type I NRPS systems may not recognize Type II NRPS systems and vise versa.

Despite the poor conservation between all five PCPs, certain aspects of the core motif, mainly Lx[5]Gx[5]Fx[2]GGxSx[4]Q, remain consistent. In all cases, residues for SfP recognition are similar enough on all five PCPs to allow the transfer of Bodipy-PPant [43]. The majority of conserved residues are also hydrophobic, suggesting the interaction between the T-domain and the hydroxylase are driven by Van der Waals forces or are less reliant on electrostatics for their direct connection with each other. The PCP TycC3 from the tyrocidine biosynthetic pathway contains a leucine residue that is presumably associated with the interaction between the itself and Sfp [44], although there are PCPs where the SfP recognition site could not be elucidated [45]. Mutation of this leucine from TycC3 inhibited recognition of SfP for the T-domain, but it is unknown whether similar behavior occurs with hydroxylase/T-domain interactions. Residues on the flanking ends of the PCPs may assist with protein-protein interaction or they may provide subtle positioning of the four-helix bundle so residues near the SfP recognition site can interact with the hydroxylase. Site-directed mutations demonstrate that alterations of the α-helices of the PCP will destabilize the interaction between the PCP and Sfp [46].

Oxidation rates of PCPs with Orf78

A study of diferrous CmlA and its NRPS system shows an association between the rate of oxidation of the enzyme and the presence of aminoacylated- or non-amionoacylated NRPS and molecular oxygen, which conclude that a notable difference exists concerning oxygen-gating by the enzyme [20]. In the absence of NRPS, the rate of oxidation for CmlA is slow at 0.005 s^{-1}. The rate is relatively unchanged upon the introduction of apo- or holo-NRPS, with an observed rate of 0.01 s^{-1}. The rate of oxidation increases to 12 s^{-1} in the presence of aminoacylated NRPS, suggesting that proper binding and channel access for O_2 in CmlA occurs only in the presence of aminoacylated-NRPS.

This experiment was reproduced with Orf78 to determine the rate of oxidation for the enzyme in the presence of native and non-native PCPs. Since phenylalanine is one of the native substrates recognized by Orf78 and the aromatic ring is similar to the native tyrosine substrate for PCP_{Tyr6} and the native L-PABA substrate for CmlP, recognition is assumed to be driven by the binding motifs on the PCPs and not the tethered amino acid. Poor expression and solubility of PCP_{Asn10} prevents these experiments from being performed under pseudo-first order conditions so the molar excess of PCP was kept at no more than four times greater than Orf78 for all three T-domains.

All rate measurements are shown in Figure 1.10. The oxidation rates for Orf78 in the presence of any apo-PCP and holo-PCP results in a slow rate of oxidation of 0.004 s^{-1}, similar to Orf78 in the absence of PCP and the rates of CmlA under similar circumstances. The lack of a biologically significant rate indicates that either the apo- nor holo- forms of the PCP do not bind or that that they bind but do not properly gate O_2 in the absence of tethered amino acid. Orf78 in the presence of Phe-PCP_{Asn10} shows fits with a double exponential, with an initial phase of 0.2 s^{-1} followed by a second phase of 0.005 s^{-1}. The initial phase may be a mixture of the PCP binding event and quick oxidation and a slow oxidation rate due to unbound enzyme, and artifact of the experiment not adhering to pseudo-first order conditions. The second phase is likely O_2 gating into Orf78 unbound to PCP_{Asn10}. The rates of Orf78 in the presence of Phe-PCP_{Tyr6} and Phe-$CmlP_T$ is monophasic with an oxidation rate of 0.004 s^{-1}, matching the oxidation rate of Orf78 in the absence of PCP. This suggests there is another factor other than substrate recognition that is inhibiting binding of the hydroxylase to the PCP, such as the proposed incompatibility with $CmlP_T$ proposed earlier or the presence of higher dissociation constants between Orf78 and non-native T-domains.

1.4 DISCUSSION

It is necessary to study monooxygenases homologous to CmlA enhance the flexibility of enzyme choice when engineering a biosynthetic gene cluster. This choice may allow for the recognition of certain modules in a semi-specific manner and is important when attempting to build libraries of antibiotic-like compounds. Ideally, the selection of a hydroxylase for an engineered NRPS system would be dependent on its solubility *in-vivo*, redox partners, and its ability to properly recognize and utilize cofactors required to perform the necessary chemistry. Experiments *in-vitro* with Orf78 attempt to discern the viability of combining the use of an enzyme from one pathway with PCP components from non-native systems in an effort to discern the specificity of these interactions. However, the results do not favor the use of non-native enzymes with NRPS systems without modifying their components to promote a higher degree of recognition between the two. Although there is an interaction between Orf78 and PCP_{Asn10}, there is no interaction with the non-native aminoacylated-PCPs.

The oxidation rate of the Orf78/Phe-PCP_{Asn10} complex does not reach a level to be considered biologically relevant, as bacterial defenses would be overwhelmed with such slow production. This contrasts with the oxidation rate for CmlA in the presence of L-PAPA-$CmlP_{AT}$ at 12 s^{-1}, rising two orders of magnitude higher than any of the rates associated with Orf78. One argument is that the dissociation constant of the interaction is much higher than published for other hydroxylase/PCP systems, such as $P450_{sky}$ or $P450_{nikQ}$, and ratio of PCP to Orf78 is too low to visualize quick oxidation. This led to a slower rate for the first phase than would otherwise be observed. It is currently unknown if there are additional interactions between the hydroxylase and the A-domain that assist with recognition and helps to guide the interaction. Unfortunately, the rate for CmlA/L-PAPA-$CmlP_T$ is unknown, so a true comparison between Orf78/PCP_{Asn10} and CmlA/$CmlP_{AT}$ cannot be obtained. The inability to clone out any soluble forms of the AT domains from lysobactin system prevented testing that hypothesis with any complexes with Orf78.

The inability to properly model $CmlP_T$ based off of published NMR structures suggests potential problems with interactions between Orf78 and

$CmlP_T$, explaining the absence of reactivity during oxidation experiments with Orf78. However, is should be noted that the Phe-PPant may not sit correctly on the PCP if the para-amino group is influences the interaction of substrate stability on the T-domain and destabilizing its binding to the hydroxylase. In addition, the NRPS from the chloramphenicol pathway is unimodular and may not have sufficient complexity compared to their multimodular counterparts, meaning the modular components of $CmlP_{AT}$ may not be homologous with Type II NRPS systems and cannot interact with Orf78. However, Phe-PCP_{Tyr6} displays a monophasic rate comparable to Orf78 alone with O_2. This is surprising since its sequence aligns the alpha-helical regions well for PCP_{Tyr6} and PCP_{Asn10}. Although the similarity between these two PCPs appear high enough to assume some interaction between the hydroxylase and the Phe-PCP_{Tyr6} domain, this illustrates the subtlety of the structural differences between the PCPs from these two systems and represent the fine-tuning that must occur to properly lock the complex into place.

Although the enzyme purifies as a dimer, the issues concerning the protein-protein interaction between an enzyme with a singly-loaded cluster per dimer an the PCP domain may affect the kinetic rates, although these effects are not known. The incompleteness of iron-loading may be due to iron lability in the unloaded monomer. Alternatively, the unloaded monomer may be forced into a different structural conformation by the loaded monomer and inherently does not load upon dimerization. One example involves the incomplete loading of the dimeric diiron enzyme hp53R2, which fully loads one cluster into one monomer but only partially loads the second cluster in the second monomer due to the loaded monomer exerting conformation dominance over the partially loaded monomer [47]. However, the result for Orf78 differs from CmlA, which purifies with two complete clusters per dimer; so nuances concerning the monomeric influences for the dimeric form may exist for Orf78. If the enzyme solely operates on the NRPS system, as its placement in the lysobactin operon suggests, then there is no need for a two fully-loaded clusters per dimer to do the necessary chemistry, as only one monomer could bind at a time to the larger, multimodular complex. Since the unloaded monomer is presumably distorted in a manner that prevents iron-loading, it is unknown whether PCP_{Asn10} will prioritize the loaded monomer over the unloaded one. Additionally, any PCP bound to the unloaded, non-catalytic monomer will lower the rate of oxidation since the effective concentration of PCP will be lower than previously calculated. The PCP concentration is already poised for sub-pseudo first order kinetics with only a four-fold excess to Orf78, so the effective concentration will be halved at two-fold to Orf78, assuming the PCP binds with equal preference for each monomer. Alternatively, PCP binding to one monomer may inhibit binding to the unbound monomer.

1.5 CONCLUSION

Orf78, the hydroxylase from the lysobactin biosynthetic pathway, was purified and characterized as a dimeric, diiron enzyme. The hydroxylated PCP domains from the lysobactin pathway are compared to view similarities in homology as well as to compare them to non-native hydroxylated PCPs from the

Type I NRPS teicoplanin and Type II NRPS chloramphenicol biosynthetic pathways. Oxidation experiments were performed to test for protein-protein interactions between these PCPs and Orf78, with the only interaction recorded with Orf78's native T-domain, $\text{PCP}_{\text{Asn10}}$. The reasoning for some T-domains being hydroxylated and not others is still an aspect of ongoing research by both our and other labs.

1.6 References

[1] Chambers, H. F., and Deleo, F. R. (2009) Waves of resistance: Staphylococcus aureus in the antibiotic era, *Nat. Rev. Microbiol. 7*, 629-641.

[2] Dohrmann, S., Anik, S., Etesami, N., No, H., Olson, J., Nizet, V., and Okumura, C. Y. (2013) Streptococcal Collagen-Like Protein 1 (Scl-1) Protects Group A Streptococcus From Antimicrobial Molecules, *Mol Biol Cell 24*, 4011-4020.

[3] Shimamoto, J., Doehrmann, S., Etesami, N., Martin, G., Nizet, V., and Okumura, C. (2014) Streptococcal collagen-like protein 1 shields group A Streptococcus from antimicrobial molecules, *FASEB J. 28*.

[4] Dexter, H. L., Williams, H. E. L., Lewis, W., and Moody, C. J. (2017) Total Synthesis of the Post-translationally Modified Polyazole Peptide Antibiotic Goadsporin, *Angew. Chem. 56*, 3069-3073.

[5] Koteva, K., King, A. M., Capretta, A., and Wright, G. D. (2016) Total Synthesis and Activity of the Metallo--lactamase Inhibitor AspergillomarasmineA, *Angew. Chem. 55*, 2210-2212.

[6] Wojtas, K. P., Riedrich, M., Lu, J. Y., Winter, P., Winkler, T., Walter, S., and Arndt, H. D. (2016) Total Synthesis of Nosiheptide, *Angew. Chem. Int. Ed. 55*, 9772-9776.

[7] Winn, M., Fyans, J. K., Zhuo, Y., and Micklefield, J. (2016) Recent advances in engineering nonribosomal peptide assembly lines, *Nat. Prod. Rep. 33*, 317-347.

[8] Awan, A. R., Blount, B. A., Bell, D. J., Shaw, W. M., Ho, J. C. H., McKiernan, R. M., and Ellis, T. (2017) Biosynthesis of the antibiotic nonribosomal peptide penicillin in baker's yeast, *Nat Commun 8*, 1-7.

[9] Finking, R., and Marahiel, M. A. (2004) Biosynthesis of nonribosomal peptides, *Annu. Rev. Microbiol. 58*, 453-488.

[10] Strieker, M., Tanovic, A., and Marahiel, M. A. (2010) Nonribosomal peptide synthetases: structures and dynamics, *Curr. Opin. Struct. Biol. 20*, 234-240.

[11] Wise, C. E., and Makris, T. M. (2017) Recruitment and Regulation of the Non-ribosomal Peptide Synthetase Modifying Cytochrome P450 Involved in Nikkomycin Biosynthesis, *Acs Chem Biol 12*, 1316-1326.

[12] Uhlmann, S., Sussmuth, R. D., and Cryle, M. J. (2013) Cytochrome p450sky interacts directly with the nonribosomal peptide synthetase to generate three amino acid precursors in skyllamycin biosynthesis, *Acs Chem Biol 8*, 2586-2596.

[13] Bonner, D. P., O'Sullivan, J., Tanaka, S. K., Clark, J. M., and Whitney, R. R. (1988) Lysobactin, a novel antibacterial agent produced by Lysobacter sp. II. Biological properties, *J Antibiot (Tokyo) 41*, 1745-1751.

[14] O'Sullivan, J., McCullough, J. E., Tymiak, A. A., Kirsch, D. R., Trejo, W. H., and Principe, P. A. (1988) Lysobactin, a novel antibacterial agent produced by Lysobacter sp. I. Taxonomy, isolation and partial characterization, *J Antibiot (Tokyo) 41*, 1740-1744.

[15] Lee, W., Schaefer, K., Qiao, Y., Srisuknimit, V., Steinmetz, H., Muller, R., Kahne, D., and Walker, S. (2016) The Mechanism of Action of Lysobactin, *J. Am. Chem. Soc. 138*, 100-103.

[16] Gale E.F, C. E., Reynolds P.E., Richmond M.H., Waring M.J. (1981) *The Molecular Basis of Antibiotic Action*, 2nd ed., John Wiley & Sons Ltd, New York, NY.

[17] Ling, L. L., Schneider, T., Peoples, A. J., Spoering, A. L., Engels, I., Conlon, B. P., Mueller, A., Schaberle, T. F., Hughes, D. E., Epstein, S., Jones, M., Lazarides, L., Steadman, V. A., Cohen, D. R., Felix, C. R., Fetterman, K. A., Millett, W. P., Nitti, A. G., Zullo, A. M., Chen, C., and Lewis, K. (2015) A new antibiotic kills pathogens without detectable resistance, *Nature 517*, 455-459.

[18] Frasch, H. J., Kalan, L., Kilian, R., Martin, T., Wright, G. D., and Stegmann, E. (2015) Alternative Pathway to a Glycopeptide-Resistant Cell Wall in the Balhimycin Producer Amycolatopsis balhimycina, *Infect. Dis. 1*, 243-252.

[19] Hou, J., Robbel, L., and Marahiell, M. A. (2011) Identification and Characterization of the Lysobactin Biosynthetic Gene Cluster Reveals Mechanistic Insights into an Unusual Termination Module Architecture, *Chem. Biol. 18*, 655-664.

[20] Makris, T. M., Chakrabarti, M., Munck, E., and Lipscomb, J. D. (2010) A family of diiron monooxygenases catalyzing amino acid beta-hydroxylation in antibiotic biosynthesis, *Proc. Natl. Acad. Sci. USA 107*, 15391-15396.

[21] Pohle, S., Appelt, C., Roux, M., Fiedler, H. P., and Sussmuth, R. D. (2011) Biosynthetic Gene Cluster of the Non-ribosomally Synthesized Cyclodepsipeptide Skyllamycin: Deciphering Unprecedented Ways of Unusual Hydroxylation Reactions, *J. Am. Chem. Soc. 133*, 6194-6205.

[22] Schwede, T., Kopp, J., Guex, N., and Peitsch, M. C. (2003) SWISS-MODEL: an automated protein homology-modeling server, *Nucleic Acids Res. 31*, 3381-3385.

[23] Rosenzweig, A. C., Frederick, C. A., Lippard, S. J., and Nordlund, P. (1993) Crystal-Structure of a Bacterial Nonheme Iron Hydroxylase That Catalyzes the Biological Oxidation of Methane, *Nature 366*, 537-543.

[24] Lindqvist, Y., Johansson, E., Kaija, H., Vihko, P., and Schneider, G. (1999) Three-dimensional structure of a mammalian purple acid phosphatase at 2.2 A resolution with a mu-(hydr)oxo bridged di-iron center, *J. Mol. Biol. 291*, 135-147.

[25] Nordlund, P., and Eklund, H. (1993) Structure and Function of the Escherichia-Coli Ribonucleotide Reductase Protein R2, *J. Mol. Biol. 232*, 123-164.

[26] Kao, W. C., Wang, V. C., Huang, Y. C., Yu, S. S., Chang, T. C., and Chan, S. I. (2008) Isolation, purification and characterization of hemerythrin from Methylococcus capsulatus (Bath), *J. Inorg. Biochem. 102*, 1607-1614.

[27] Reem, R. C., Mccormick, J. M., Richardson, D. E., Devlin, F. J., Stephens, P. J., Musselman, R. L., and Solomon, E. I. (1989) Spectroscopic Studies of the Coupled Binuclear Ferric Active-Site in Methemerythrins and Oxyhemerythrin - the Electronic-Structure of Each Iron Center and the Iron-Oxo and Iron Peroxide Bonds, *J. Am. Chem. Soc. 111*, 4688-4704.

[28] Kurtz, D. M. (1990) Oxo-Bridged and Hydroxo-Bridged Diiron Complexes - a Chemical Perspective on a Biological Unit, *Chem. Rev. 90*, 585-606.

[29] Vu, V. V., Emerson, J. P., Martinho, M., Kim, Y. S., Munck, E., Park, M. H., and Que, L., Jr. (2009) Human deoxyhypusine hydroxylase, an enzyme involved in regulating cell growth, activates O2 with a nonheme diiron center, *Proc Natl Acad Sci U S A 106*, 14814-14819.

[30] Chino, M., Maglio, O., Nastri, F., Pavone, V., DeGrado, W. F., and Lombardi, A. (2015) Artificial Diiron Enzymes with a De Novo Designed Four-Helix Bundle Structure, *Eur. J. Inorg. Chem.*, 3371-3390.

[31] Kamat, S. S., Holmes-Hampton, G. P., Bagaria, A., Kumaran, D., Tichy, S. E., Gheyi, T., Zheng, X., Bain, K., Groshong, C., Emtage, S., Sauder, J. M., Burley, S. K., Swaminathan, S., Lindahl, P. A., and Raushel, F. M.

(2011) The catalase activity of diiron adenine deaminase, *Protein Sci. 20*, 2080-2094.

[32] Davydov, R., Kuprin, S., Graslund, A., and Ehrenberg, A. (1994) Electron-Paramagnetic-Resonance Study of the Mixed-Valent Diiron Center in Escherichia-Coli Ribonucleotide Reductase Produced by Reduction of Radical-Free Protein-R2 at 77-K, *J. Am. Chem. Soc. 116*, 11120-11128.

[33] Fox, B. G., Surerus, K. K., Munck, E., and Lipscomb, J. D. (1988) Evidence for a mu-oxo-bridged binuclear iron cluster in the hydroxylase component of methane monooxygenase. Mossbauer and EPR studies, *J. Biol. Chem. 263*, 10553-10556.

[34] Mccormick, J. M., Reem, R. C., and Solomon, E. I. (1991) Chemical and Spectroscopic Studies of the Mixed-Valent Derivatives of the Nonheme Iron Protein Hemerythrin, *J. Am. Chem. Soc. 113*, 9066-9079.

[35] Davydov, R. M., Smieja, J., Dikanov, S. A., Zang, Y., Que, L., Jr., and Bowman, M. K. (1999) EPR properties of mixed-valent mu-oxo and mu-hydroxo dinuclear iron complexes produced by radiolytic reduction at 77 K, *J. Biol. Inorg. Chem. 4*, 292-301.

[36] Davydov, R., Behrouzian, B., Smoukov, S., Stubbe, J., Hoffman, B. M., and Shanklin, J. (2005) Effect of substrate on the diiron(III) site in stearoyl acyl carrier protein Delta(9)-desaturase as disclosed by cryoreduction electron paramagnetic resonance/electron nuclear double resonance spectroscopy, *Biochemistry-Us 44*, 1309-1315.

[37] Hirsh, D. J., and Brudvig, G. W. (2007) Measuring distances in proteins by saturation-recovery EPR, *Nat Protoc 2*, 1770-1781.

[38] Berthold, D. A., Voevodskaya, N., Stenmark, P., Graslund, A., and Nordlund, P. (2002) EPR studies of the mitochondrial alternative oxidase - Evidence for a diiron carboxylate center, *J. Biol. Chem. 277*, 43608-43614.

[39] Bushley, K. E., Ripoll, D. R., and Turgeon, B. G. (2008) Module evolution and substrate specificity of fungal nonribosomal peptide synthetases involved in siderophore biosynthesis, *BMC Evol. Biol. 8*, 328.

[40] Bushley, K. E., and Turgeon, B. G. (2010) Phylogenomics reveals subfamilies of fungal nonribosomal peptide synthetases and their evolutionary relationships, *BMC Evol. Biol. 10*, 1-23.

[41] Li, T. L., Huang, F. L., Haydock, S. F., Mironenko, T., Leadlay, P. F., and Spencer, J. B. (2004) Biosynthetic gene cluster of the glycopeptide antibiotic teicoplanin: Characterization of two glycosyltransferases and the key acyltransferase, *Chem. Biol. 11*, 107-119.

[42] He, J., Magarvey, N., Piraee, M., and Vining, L. C. (2001) The gene cluster for chloramphenicol biosynthesis in Streptomyces venezuelae ISP5230 includes novel shikimate pathway homologues and a monomodular non-ribosomal peptide synthetase gene, *Microbiology-Sgm 147*, 2817-2829.

[43] Reuter, K., Mofid, M. R., Marahiel, M. A., and Ficner, R. (1999) Crystal structure of the surfactin synthetase-activating enzyme sfp: a prototype of the 4'-phosphopantetheinyl transferase superfamily, *EMBO J. 18*, 6823-6831.

[44] Tufar, P., Rahighi, S., Kraas, F. I., Kirchner, D. K., Lohr, F., Henrich, E., Kopke, J., Dikic, I., Guntert, P., Marahiel, M. A., and Dotsch, V. (2014) Crystal Structure of a PCP/Sfp Complex Reveals the Structural Basis for Carrier Protein Posttranslational Modification, *Chem. Biol. 21*, 552-562.

[45] Mofid, M. R., Finking, R., Essen, L. O., and Marahiel, M. A. (2004) Structure-based mutational analysis of the 4'-phosphopantetheinyl transferases Sfp from Bacillus subtilis: carrier protein recognition and reaction mechanism, *Biochemistry-Us 43*, 4128-4136.

[46] Quadri, L. E., Weinreb, P. H., Lei, M., Nakano, M. M., Zuber, P., and Walsh, C. T. (1998) Characterization of Sfp, a Bacillus subtilis phosphopantetheinyl transferase for peptidyl carrier protein domains in peptide synthetases, *Biochemistry-Us 37*, 1585-1595.

[47] Zhou, B., Su, L., Yuan, Y. C., Un, F., Wang, N., Patel, M., Xi, B., Hu, S., and Yen, Y. (2010) Structural basis on the dityrosyl-diiron radical cluster and the functional differences of human ribonucleotide reductase small subunits hp53R2 and hRRM2, *Mol. Cancer Ther. 9*, 1669-1679.

Figures and Tables

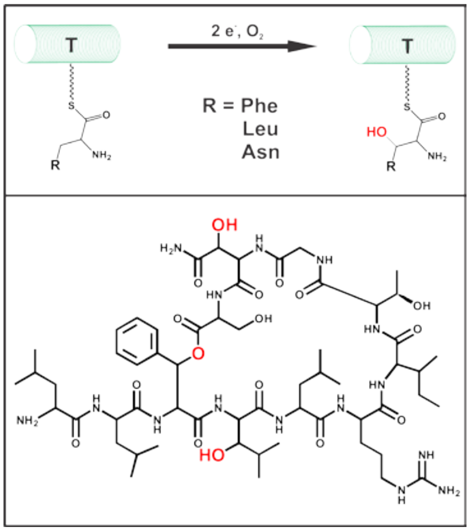

Figure 1.1: Diagrams of the hydroxylation reaction with P450sky and the lysobactin antibiotic. Top panel - a diagram of the pre- and post-hydroxylated PCP with affected amino acids. Bottom panel – a diagram of the depsipeptide antibiotic lysobactin. Red lettering indicates the locations of hydroxylation by Orf78.

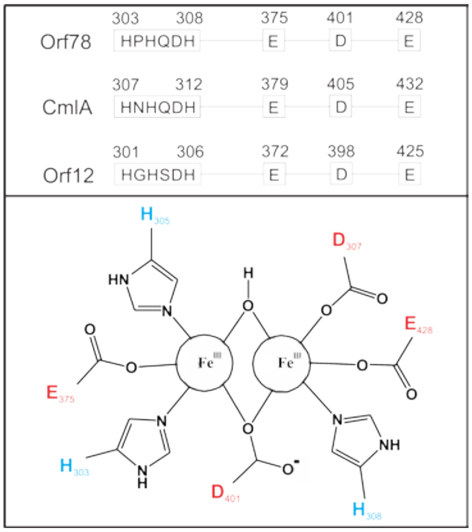

Figure 1.2: Diagrams of Orf78 endogenous ligands and the active-site structure. Top panel – sequence alignment for the endogenous iron ligands in the diiron hydroxylases associated with the biosynthesis of lysobactin (Orf78), chloramphenicol (CmlA), and teicoplanin (Orf12). Bottom panel – a diagram of the proposed active site symmetry for Orf78 based off of the crystal structure of CmlA.

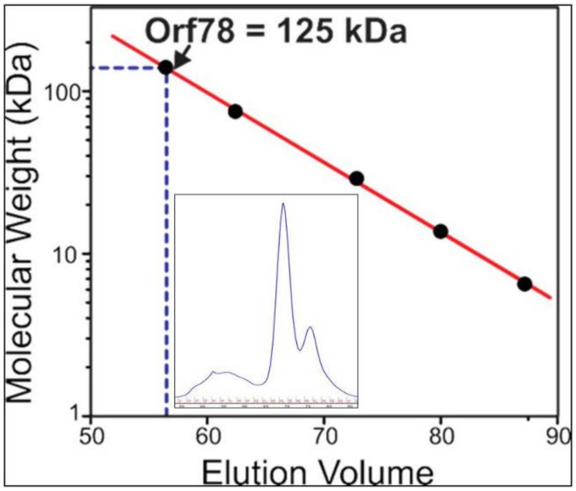

Figure 1.3: Size-exclusion chromatography plot of Orf78. The elution profile is present in the insert. 25 µM protein was directly injected onto the column following purification. The elution profile shows a dimeric form of the enzyme with no peaks suggesting monomeric or other oligomeric forms of the protein, with extraneous peaks eluting earlier and later being contaminants present during purification.

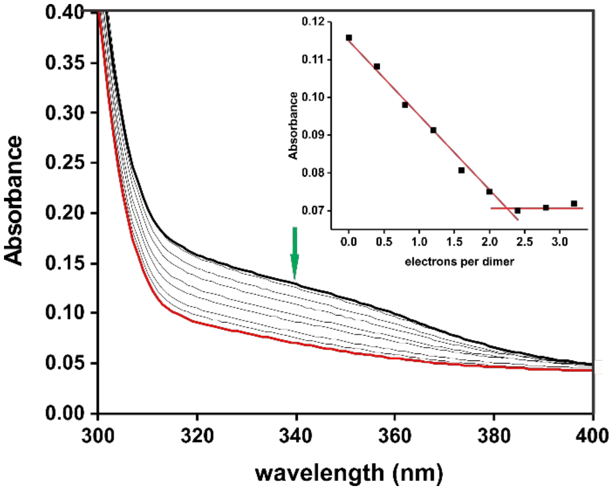

Figure 1.4: Reductive titration of Orf78. The plot shows the bleaching of the band at 340 nm as sodium dithionite reduces the enzyme from the diferric to the diferrous state. The inset shows a plot of the titration points and show the requirement of 2.3 electrons to fully reduce the enzyme, confirming the presence of a diiron cluster.

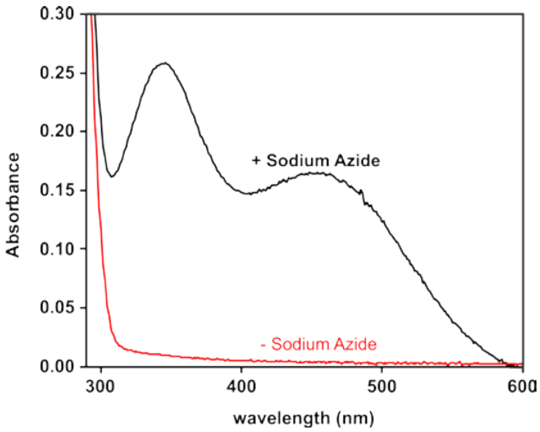

Figure 1.5: Optical spectrum of Orf78 incubated with sodium azide. 3.5 µM enzyme was incubated with 8 M sodium azide, 100 mM HEPES, pH=7.5. The pronounced peaks at 340 nm and 460 nm are due to enhancements of the charge-transfer bands between the two iron atoms caused by the addition a bridging azide molecule.

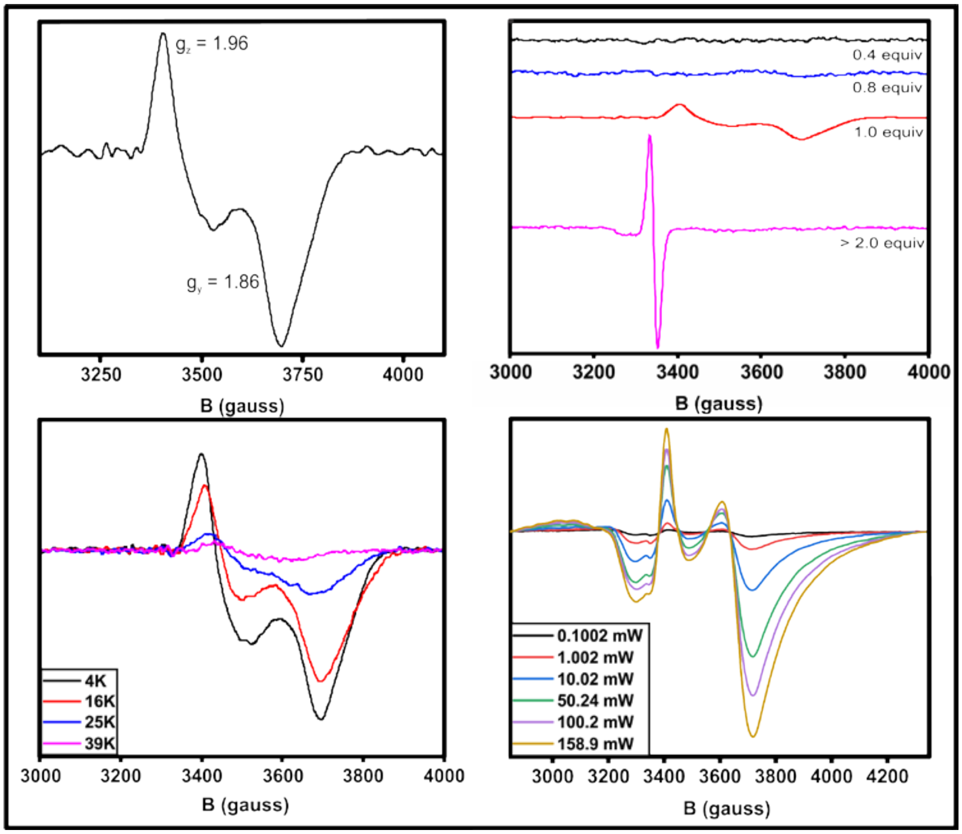

Figure 1.6: EPR spectra of mixed-valent Orf78, dithionite saturation, power saturation, and temperature saturation. Top left – mixed-valent EPR spectrum of 200 µM Orf78. Top right – EPR spectra of Orf78 with 0.4, 0.8, 1.0, and 2.5 molar equivalents of electrons, demonstrating the transition from the diferric to mixed-valent to diferrous state. Bottom left – temperature saturation of the mixed-valent signal. The signal bleaches as temperatures reach 40K, indicating the presence of a hydroxo-bridge between the two iron atoms. Bottom right – three spectra of the mixed-valent sample demonstrating the relationship of signal degradation as a function of increasing power.

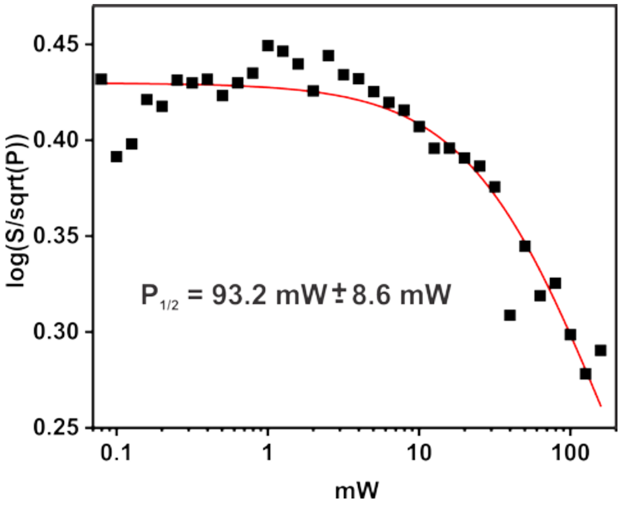

Figure 1.7: Power saturation curve for Orf78 at 10K. The sample consists of 200 µM mixed-valent Orf78. The half-saturation value is 2 mW higher than CmlA, but reasonably similar to justify assignment of the same J coupling constant.

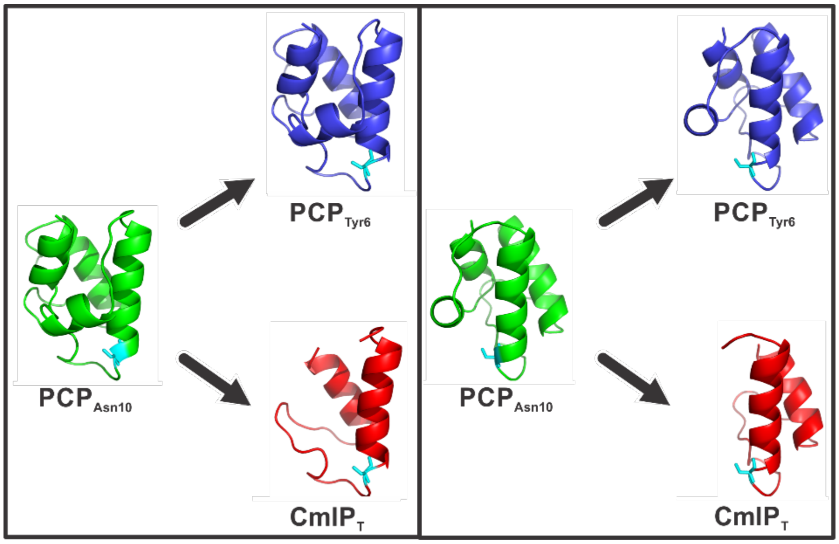

Figure 1.8: Molecular models for PCP_{Asn10}, PCP_{Tyr6}, and $CmlP_T$. Models of PCP_{Tyr6} from the teicoplanin pathway and $CmlP_T$ from the chloramphenicol pathway based off of a model of PCP_{Asn10} from the lysobactin pathway (derived from PDBID# 1DNY). The panel on the right duplicates the models on the left but with a 90° rotation. Note the absence of two terminal helices for CmlPT that do not align in the model.

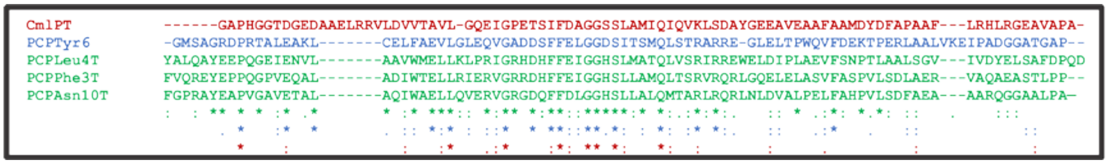

```
CmlPT           ------GAPHGGTDGEDAAELRRVLDVVTAVL-GQEIGPETSIFDAGGSSLAMIQIQVKLSDAYGEEAVEAAFAAMDYDFAPAAF---LRHLRGEAVAPA-
PCPTyr6         -GMSAGRDPRTALEAKL-------CELFAEVLGLEQVGADDSFFELGGDSITSMQLSTRARRE-GLELTPWQVFDEKTPERLAALVKEIPADGGATGAP--
PCPLeu4T        YALQAYEEPQGEIENVL-------AAVWMELLKLPRIGRHDHFFEIGGHSLMATQLVSRIRREWELDIPLAEVFSNPTLAALSGV---IVDYELSAFDPQD
PCPPhe3T        FVQREYEPPQGPVEQAL-------ADIWTELLRIERVGRRDHFFEIGGHSLLAMQLTSRVRQRLGQELELASVFASPVLSDLAER---VAQAEASTLPP--
PCPAsn10T       FGPRAYEAPVGAVETAL-------AQIWAELLQVERVGRGDQFFDLGGHSLLALQMTARLRQRLNLDVALPELFAHPVLSDFAEA---AARQGGAALPA–
                :  : ** * * :* .*       * :* ***:: *:** *:**::*****:* *:.:*:*:.   :: * .:*: *.*: ::   .    :::
                      . *   :*  *       . :: *:* : ::*  * **::**.*: : *: :* *:.   ::   .:*   .   ::           ::
                        *    :            :   :*   .:*    :*: ** *:   *:  :       :     .         :            :
```

Figure 1.9: Sequence alignment for PCPs from lysobactin, teicoplanin, and chloramphenicol pathways. Sequence alignment showing homology among the three hydroxylated PCPs for lysobactin (green), lysobactin PCPs with the addition of the PCP from teicoplanin (blue), and also lysobactin and teicoplanin PCPs with the addition of the PCP from chloramphenicol (red). There is slight drop in homology between the lysobactin and teicoplanin PCPs, both derived from Type I NRPSs. The homology heavily decreases upon the addition of the chloramphenicol PCP, derived from a Type II NRPS.

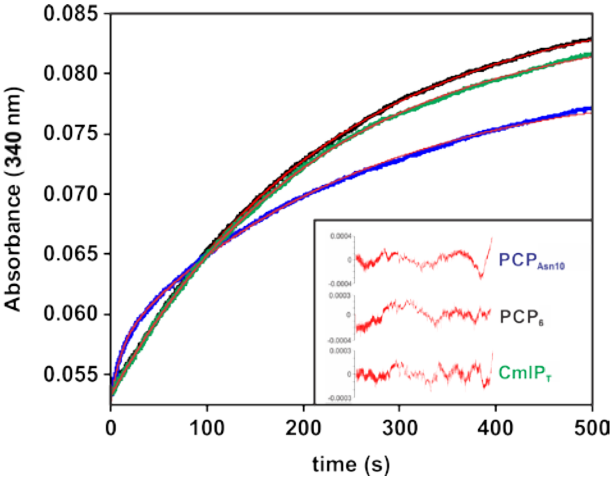

Figure 1.10: Oxidation of reduced Orf78 with aminoacylated PCPs. 25 μM reduced Orf78 was shot against either a four-fold excess of L-phe-PCP$_{Asn10}$, ten-fold excess of L-phe-PCP$_{Tyr6}$, or ten-fold excess of L-phe-CmlP$_T$ and 1 mM O_2. The results are biphasic for Orf78's native PCP, but monophasic for the two non-native PCPs.

Table 1.1: Sequence identity of 3 cognate and 2 non-cognate PCPs for P450sky

	CmlP$_{T}$	PCP$_{Tyr6}$	PCP$_{Leu4}$	PCP$_{Phe3}$	PCP$_{Asn10}$
CmlP$_{T}$	**100.00**	**20.99**	**19.28**	**21.95**	**20.73**
PCP$_{Tyr6}$	**20.99**	**100.00**	**32.18**	**33.33**	**32.18**
PCP$_{Leu4}$	**19.28**	**32.18**	**100.00**	**47.19**	**39.33**
PCP$_{Phe3}$	**21.95**	**33.33**	**47.19**	**100.00**	**57.30**
PCP$_{Asn10}$	**20.73**	**32.18**	**39.33**	**57.30**	**100.00**

The average identity of the three lysobactin PCPs is between 40%-60%. The identity of those three to the teicoplanin PCP drops to 30%. Furthermore, their identity compared to the PCP from Chloramphenicol is further lowered to 20%.

CHAPTER 2

DETERMINATION OF THE ROLE OF A NON-RIBOSOMAL PEPTIDE SYNTHETASE IN THE RECOGNITION OF A NON-COGNATE TAILORING ENZYME

2.1 INTRODUCTION

Bacterial synthesis of antibiotics has been intensively studied over the past three decades, but have not ranged beyond the analysis of individual biosynthetic pathways. As more of the individual components of the machinery are elucidated, the creation of novel synthetic pathways that are transformable into a bacterial host for the mass production of new products are providing a natural change in direction for future research. Alteration of currently understood non-ribosomal peptide synthetase (NRPS) systems provides a basis for this research; however, their use in conjunction with cognate tailoring enzymes may enhance the range of possible products. Although these cognate enzymes have been elucidated in several systems [1-7], their interactions with the NRPS subunits are unclear, as well as their potential interactions with non-native systems. An understanding of how these processes behave may assist in the choice of gene combinations, potentially from multiple pathways, necessary to form newly-designed operons that are capable of synthesizing a new natural product.

The number of biosynthetically derived antibiotics vary greatly due to the system-dependent combinations of both natural and non-natural amino acids that may be incorporated during the peptide synthesis. Each system is driven by NRPS-specific modules that choose, modify, and incorporate the amino acids that form the final product. This leads to a multitude of potential enzymes and domains that specialize in substrate selection and potential chemical modification. A couple of well documented examples include the lactonization of skyllamycin by a thioesterase as well as the incorporation of sugars onto the peptide backbone of vancomycin by methylases [8, 9]. To further narrow the reaction specificity involving sugar incorporation above, dehydrogenases have been observed that are selective for either O- or N-methylation in various pathways [10-13]. To stress the importance of these chemistries, these types of translational and post-translational modifications act as inhibitors of cellular function within a target cell necessitating that the producer counteract the effects of these inhibitors while the antibiotic producer contains immunity to their effects [14, 15], as is the case with the methyltranferase Cfr in *S. aureus*, a protein responsible for the methylation of several residues on the 23S ribosomal RNA that inhibits the binding of chloramphenicol [16].

The creation of a synthetically created antibiotic biosynthesis pathway is a major milestone for researchers, as it will allow for the formation and testing of compounds different from those found in nature. Theoretically, the effects of these compounds would be difficult for bacterial targets to overcome since the scaffold of their resistance machinery cannot compensate for compounds with greatly different chemical properties from those already present. One likely avenue of study is the manipulation of existing pathways that may lead to the discovery of new drugs, including techniques that create a plug-and-play system that can create libraries of similar compounds through modifications of simple yet necessary chemistries that can be tested for antibiotic effectiveness. An example is the incorporation of different chemistries through the use of enzymes that operate as individual *in trans* modifiers, rather than *in cis* domains that are incorporated into the NRPS machinery [5, 17, 18]. For example, hydroxylases such as P450sky (CYP163B3) are expressed as gene product independent of its NRPS within the skyllamycin biosynthetic operon [8]. Not only is the protein more likely to be soluble since it is not excised from a larger complex, but the residues that form the recognition interface may be used to modify an NRPS module for hydroxylation. Attempts to incorporate an enzyme into an NRPS module may lead to instability due to interference with the inter-modular interactions necessary for the incorporation and passing of the amino acids through the NRPS machinery [19, 20]. Therefore, it is best to avoid direct modification of the NRPS modules.

Since the addition of a separate, individual protein is less troublesome than the modification of an existing module, the former became the focus of this research utilizing P450sky from the skyllamycin biosynthetic pathway. Work by Cryle *et al* has demonstrated that P450_{sky} is a monooxygenase that incorporates a hydroxyl group into the beta carbon of L-leucine, O-methyl-L-tyrosine, and L-phenylalanine while appended on the thiolation-domain during the synthesis of skyllamycin [21]. The P450 contains a thiolate-ligated porphyrin cofactor in the protein’s active site that receives electrons from a ferredoxin that docks on the proximal face of the enzyme. The structure of the protein shows a deep channel from the surface residues to the porphyrin (~23 Angstroms). The F and G helices are culpable for the binding of the T-domain, although the exact residues responsible are unknown [22]. Interestingly, the crystal structures published by Cryle et al. suggests that there is minimal conformation change between the unbound state and the bound state (PDB ID: 4PWV, 4LOF; this work). A crystal structure showing P450sky bound to PCP_{Tyr7} of the skyllamycin pathway by way of ligation of an PPant-imidazole ligand to the heme iron suggests that the interactions are driven by hydrophobic residues at the interface (PDB ID: 4PWV).

The overall hydrophobic character of the skyllamycin antibiotic allows for the inhibition of the mechanism involved with the biosynthesis of the bacterial cell wall. However, the presence of multiple hydrophobic residues decreases its solubility - allowing for an evolutionarily viable explanation for the addition of hydroxyl groups to the peptide. Other residues were also tested, mostly consisting of hydrophobic L-, and D-amino acids on all three T-domains. The results concluded that D-amino acids are not hydroxylated and non-cognate amino acids (tryptophan and tyrosine) were only hydroxylated with reduced efficiency. There were no tests on amino acids with charged side chains to determine their effectiveness for hydroxylation. Therefore, the tethered amino acid does appear to play a small, but important, role in the overall recognition of the hydroxylase to the substrate-bound carrier. The structure of the imidazole-ligated T-domain shows interactions with side chains in the channel with the PPant residue that extends toward the active site from the T-domain, enhancing the binding interface. However, there is currently no evidence of complex formation with the apo- or holo-T-domain, as there is no product to test for activity. The understanding of the hydrophobic nature of the interaction is not yet understood, as no experiments have been performed under high-salt conditions.

P450nikQ (CYP162A1), an enzyme that operates *in trans* to the NRPS in the nikkomycin biosynthetic pathway and is homologous to P450sky, interacts with a unimodular NRPS (NikP1) and is responsible for the β-hydroxylation of a tethered histidine residue. Both genes are located within the same operon and are expressed as single proteins. P450$_{\text{nikQ}}$ and P450$_{\text{sky}}$ share an amino acid sequence similarity of 53.3% along with a sequence identity of 33.6%, allowing for a reasonable comparison of the two as homologs. A model of P450nikQ based on the substrate-free P450sky structure (PDB ID: 4L0F), shows a preference of polar residues leading to the active site of the enzyme, whereas P450$_{\text{sky}}$ contributes mostly hydrophobic residues with a preference for phenylalanine. These residues may assist in guiding the tethered amino acid through the channel and may dictate which side chains are acceptable for recognition by the enzyme. The exterior surface of the enzymes shows little in shared similarity, other than a patch of cationic residues on the surface proximal to the porphyrin that presumably binds an unidentified ferredoxin. The binding interfaces for the P450s that are involved with their interactions with the T-domains show little similarity, consisting of residues that often differ in polarity. This is important given that the high amount of similarity between the T-domain for NikP1 and PCP$_{\text{Tyr7}}$, (51.3% identity and 35.5% similarity) would imply that both P450 enzymes would be able to recognize T-domains from each other's systems. This gives credence to the conclusions by Cryle *et al.* concerning hydrophobic forces driving the interaction with the enzyme and the NRPS.

Under canonical conditions involving redox partners, the shift from a low-spin to high-spin state raises the potential of the enzyme, a gating behavior necessary to deter the unnecessary transfer of electrons to enzyme that is not substrate-bound and decreases the production of subsequent radical oxygen species [23]. The rise in potential originates from the movement of an electron from a lower energy orbital to a higher energy orbital, instigating a state of greater reactivity with molecules that are in energetically low triplet state, such as molecular oxygen. P450sky, to the contrary, does not exhibit a spin-shift upon binding with aminoacylated NikP1AT due to its ferric high-spin redox potential resting around -300 mV, lower than CYP101A1 which has potentials for low-spin at -303 mV and high-spin at -173 mV [24, 25]. Among the differences between the homologs, there is a small, observable shift from low-spin to high-spin for P450sky upon the addition of the L-Tyr-PCP_{Tyr7} carrier protein, indicating that the redox potential for the bound species is higher in P450sky. Due to the lack of high-spin for P450nikQ, Wise confirmed through an EPR titration that L-His-NikP1AT binds with P450nikQ, along with the unexpected result of the histidine side group ligating to the iron of the porphyrin. Using this method of analysis, the dissociation constant was judged to be between 50-100 µM and there is currently no evidence suggesting a reason for this high of a K_D.

The formation of peptide-based antibiotics requires a modular system that may be uni- or multimodular, where each module contains multiple domain units that cooperate for the creation of the antibiotic. The skyllamycin biosynthetic pathway involves 11 modules in the creation of the depsipeptide, with each module involved in the activation and incorporation of a specific amino acid. The size of these systems, ranging from 70 kDa for the unimodular nikkomycin NRPS to greater than 1.0 MDa with the 8 module syringomycin NRPS and the 11 module cyclosporine A NRPS, inhibit easy study since solubility may necessitate potential interactions among other modules within the system [26, 27]. Recent studies of these multimodular pathways have focused on excising certain domains or modules and observing the synthesis of small portions of the antibiotic or the conferrence of specificity towards particular amino acids [7, 28, 29]. However, it is difficult to understand the interactions between an enzyme operating *in trans* to a NRPS utilizing such a technique. There may be interactions between the enzyme and areas on the NRPS that may not have been excised for study, either other domains within the same module or even between other modules within the NRPS pathway and the exogenous enzyme. One method to bypass this obstacle is to observe a unimodular system containing a minimum number of domains. In this manner, the interactions between an exogenous enzyme and an NRPS can be studied without the loss of other, more complex interactions.

The biosynthetic mechanism for the creation of these antibiotics begins with tethering an amino acid to a phosphopantetheine (PPant), derived from

Coenzyme A (CoA) and ligated to a Thiolation (T) domain, which assists with transportation of the substrate throughout the module. The importance of the T domain cannot be understated as it inability to determine the substrate leaves it potentially open for the hydroxylation of any amino acid residue that is attached to it or improper protection of the attached amino acid, depending on its positioning post-attachment [5, 21]. The T-domain is subsequently covalently-attached to an Adenylation (A) domain, which activates a specific amino acid to be incorporated into the nascent peptide chain of the antibiotic and attaches the residue to the T-domain [30, 31]. The final covalently-attached domain that is integral for multimodular NRPS systems is the Condensation (C) domain, whose importance lies in accepting the nascent chain from the immediate upstream module and incorporating the amino acid of the current module into the growing chain [29, 32]. The formation of these individual modules must facilitate interactions with the PPant and the active sites of both the A and C domains, which necessitates constant and drastic conformational shifts as the machinery operates to extend the length of the peptide. The final module of the pathway contains a Thioesterase (TE) domain, which cleaves the peptide from the NRPS complex or promotes the formation of a depsipeptide through the formation of an intramolecular ester [33, 34].

The complexity of the multimodular system makes it difficult to synthetically produce biosynthetic pathways, so a more viable route is to study a unimodular system. The status of P450sky as a homolog of P450nikQ qualifies the use of the NikP1 NRPS system for this cross-platform study. NikP1 is a unimodular complex consisting of an A and T domain that activate and, in the presence of $P450_{nikQ}$ and its associated redox partners, β-hydroxylate a histidine residue. Other than data supporting general hydrophobicity, the characteristics describing the interaction between P450nikQ and NikP1 have not been previously elucidated, so it is unclear which surface residues are necessary for their interaction. It is not currently understood if there is a role for electrostatic residues necessary for a catalytically-relevant binding motif.

Wise collected data by size-exclusion chromatography demonstrating that $P450_{nikQ}$ binds in the presence of apo and aminoacylated forms of NikP1, but not the holo form. The solved structure of an excised di-domain derived from the gramicidin biosynthetic pathway (PDBID: 5ES6) show that the holo form is locked into a conformation where the T domain is locked into the A domain, awaiting aminoacylation [35]. This may be informative in discerning which intermediate conformations of the NRPS are available for binding by an exogenous enzyme. The elution times from the SEC are variable depending on whether P450nikQ is interacting with the apo or aminoacylated forms, with the correct molecular weight calculated when bound to the aminoacylated form but an earlier elution time for the apo. This was concluded to be different geometries of the complex formed between P450nikQ and NikP1. However, there have been no studies detailing what these possible conformations could involve.

Although the T-domain is catalytically inert, the presence of a PPant is necessary for the interaction between itself and other modules/tailoring enzymes, even without conformational changes between the apo and holo forms of the protein [22, 36]. Prior to the binding event, the loaded T-domain may coil the PPant around its own four-helix bundle, similar to the behavior of the acyl-PPant attached to acyl carrier proteins [37-39]. This “switchblade” mechanism protects the thioester bond from hydrolysis when present in the reducing, aqueous environment of the cell. This also allows surface residues of the T-domain to remain exposed for recognition by exogenous enzymes. This motif has not been observed in any holo constructs of PCP domains, so the location of the PPant during the intermediates involved between attachment of the PPant and aminoacylation of the T-domain have not been elucidated. The sites of interaction for the amino acid reside itself are not presently understood, but the selectivity for the beta position of the amino acid suggests that the amine may be stabilized by residues in the protein active site. It is currently unknown how dissociation of the enzyme from product-bound NRPS is triggered and if structural changes of the enzyme or NRPS, or a combination of the two, may be involved.

In this chapter, binding affinities between NikP1 and its cognate and non-cognate P450 hydroxylases will be probed. This is done through small molecule titration assays. In addition, EPR data recording the interaction from the perspective of both the porphyrin and the substrate is reported with results suggesting the non-cognate P450sky binds to the A-domain with no affinity to the native L-histidine substrate.

2.2 MATERIALS AND METHODS

Sub-cloning of P450sky

The codon-optimized gene for P450sky was purchased from DNA 2.0 in a pJex vector containing a T5 promoter and C-terminal 8x polyhistidine tag. The sequence included flanking restriction sites in the following pattern, 5'-*NdeI*-P450sky-*XhoI*-3'. The gene was subsequently sub-cloned into a pET21b vector, which included a T7 promoter and an N-terminal 6x polyhistidine tag.

Expression of P450sky

The plasmid was transformed into chemically competent BL21 (DE3) cells that have been previously transformed with pChuA (purchased from Addgene: plasmid #42539; deposited by Alan Jasanoff). This vector allows for the uptake of porphyrin from the media, ensuring that the rate-limiting step in the P450 biosynthesis is not the lack of Fe-Protoporphyrin IX [40]. A single colony was transferred to an overnight starter culture and 10 mL were transferred to inoculate each liter of media, which consists of the following for 500 mL: 12 g tryptone, 1 g peptone, 12 g yeast extract, 0.5% glycerol, 50 mM potassium phosphate, dibasic and potassium phosphate, monobasic, pH=7.1. The following additives were included to enhance native peptide and porphyrin production prior to the induction of the *chuA* plasmid: 10 mM casamino acids, 5 mM δ-aminolevulinic acid, and 1 mM Thiamine-HCl. Antibiotic resistance genes were activated on each plasmid with 50 mg/L kanamycin and 100 mg/L ampicillin. The culture grew at 37°C, 210 rpm until the OD_{600}=0.65, at which point the temperature was reduced to 20°C and 5 mg/L of hemin (in DMSO) was added to each flask. After 30 minutes, both genes were induced with 50 µM IPTG and the culture incubated for an additional 18 hours prior to harvesting. The culture was centrifuged at 6000 rpm for 15 minutes and stored at -80ºC until purified.

Purification of $P450_{sky}$

The cell pellet was resuspended in 250 mL of buffer consisting of 50 mM Sodium phosphate, monobasic, 300 mM Sodium chloride, and 10 mM imidazole (Buffer A). The solution was sonicated seven times on two minute cycles followed by 5 minutes of stirring on ice. The lysate was cleared by centrifugation at 16000 rpm for 35 minutes and the supernatant loaded onto a 50 mL column of Ni-NTA resin pre-equilibrated with Buffer A. The column was washed with Buffer A + 10 mM imidazole followed by elution with Buffer A + 240 mM imidazole. The eluent was concentrated and dialyzed twice in 4 L of 50 mM HEPES, pH=7.5, 10% glycerol.

After dialysis, the protein was loaded onto a 50 mL column containing diethylaminoethyl (DEAE) anion-exchange resin pre-equilibrated with 50 mM HEPES + 5% glycerol (Buffer B). The protein was subsequently washed with Buffer B + 20 mM sodium chloride followed by a gradient elution in Buffer B supplemented with 50 mM – 300 mM sodium chloride over a 300 mL volume. The fractions containing absorbance $A_{417/280}$ >1.1 were pooled and dialyzed twice in Buffer B, concentrated to a manageable volume, and flash-frozen for storage at -80ºC.

Expression of holo-NikP1AT

The expression procedure has been outlined in [24]. Briefly, the plasmid containing the gene-of-interest was transformed into chemically competent BL21 cells co-transformed with *sfp* plasmid. A starter culture was created with a single colony and 10 mL of the starter were inoculated per liter of culture, which consists of Luria-Bertani broth + 50 mg/L of Kanamycin. The cultures were grown at 37°C until an OD_{600}=0.8 was reached, when the temperature was lowered to 18°C. After 30 minutes, the vectors were induced with 200 µM IPTG and the cultures incubated for 20 hours. The culture was then spun down at 6000 rpm for 15 minutes and stored at -80°C.

Purification of holo-NikP1AT

Cells were resuspended in 350 mL of Buffer A and sonicated 10 times with 2 minute cycles with a 5 minute break between cycles. The lysate was cleared by centrifugation at 16000 rpm for 60 minutes and the supernatant was loaded onto a 50 mL Ni-NTA column pre-equilibrated with Buffer A. The column was washed with Buffer A + 10 mM imidazole, eluted with Buffer A + 240 mM imidazole, and 5 mL fractions collected. Protein was isolated by observing the absorbance at A280, with these fractions pooled and concentrated prior to dialyzing twice in 2 L of 100 mM HEPES, pH=7.5 + 10% glycerol. Following dialysis, the protein was further purified using a S-200 Size Exclusion Chromatography (SEC) column equilibrated with 100 mM HEPES, pH=7.5. The purity of the fractions was determined by SDS-PAGE, with the fractions containing the highest purity pooled and concentrated, flash-frozen, and stored at -80°C.

Cloning of PCP_{Tyr7}

The codon-optimized gene for PCP_{Tyr7} was purchased from DNA 2.0 and shipped in a pJex vector containing a T5 promoter and C-terminal Fh8 calcium-dependent protein serving as an HIC affinity tag [41]. The gene was subsequently cloned into a pDB.His.GST vector containing the following sequence: 6xhis-GST-TEV-PCP_{Tyr7} using the following primers (restriction sites are italicized):

Forward: 5'-agagtg*GAATTC*gctccgggtccagac-3'

Reverse: 5'-agagtg*CTCGAG*ttagccaccgatcagcac-3'

The gene was amplified using Pfu polymerase (Addgene plasmid #12509) [42] and a BioRad T100 Thermo Cycler for 35 cycles using the following conditions: denature- 50 sec at 94°C, anneal- 50 sec at 66°C, elongation- 2 min 15 sec at 73°C. The PCR product was gel-purified and digested overnight at 37°C with EcoRI and XhoI. The digest mixture was again gel-purified and ligated to similarly digested vector with T4 DNA ligase (Promega) overnight at room temperature. Plasmid was extracted from several colonies and the integrity of the gene was verified by sequencing at Eton Bioscience, Inc.

Expression of apo-PCP_{Tyr7}

The plasmid was transformed into chemically competent BL21 (DE3) cells and a single colony used to inoculate a starter culture. 10 mL of the starter culture were used as inoculant per 1 L of Luria-Bertani broth and the culture incubated at 37°C until the OD_{600}=0.6. Upon reaching the OD, the temperature was dropped to 30°C and the cultures were incubated for an additional 30 minutes followed by induction with 200 μM IPTG and shaken for 20 hours at 210 rpm. The cells were then centrifuged at 6000 rpm for 15 minutes and stored at -80°C.

Purification of apo-PCP$_{Tyr7}$

The pellet was resuspended in Buffer A and sonicated 10 times with 2-minute cycles and intermittent 5 minute breaks. The lysate was cleared by centrifugation at 16000 rpm for 30 minutes and the supernatant loaded onto a 30 mL Ni-NTA column pre-equilibrated with Buffer A. The column was washed with Buffer A + 10 mM imidazole and the protein eluted with Buffer A + 240 mM imidazole. The eluent was dialyzed twice in 2 L 100 mM HEPES, pH=7.5, 100 mM sodium chloride. The protein was concentrated, flash-frozen, and stored at -80°C.

Synthesis of Bodipy-Coenzyme A

This procedure is a modified version from [43]. 10 mg of Coenzyme A (CoA, Sigma-Aldrich) were dissolved in acetonitrile with 2 mg of Bodipy-FL (Thermo Fisher Scientific) in a dark environment. The reaction was stirred at room temperature for 5 minutes prior to incubation at 4°C for an additional 3 hours. The free Bodipy-FL was extracted several times with a 15-fold excess of ice-cold diethyl ether. The acetonitrile phase was dried in the dark under a stream of nitrogen gas to concentrate the material and evaporate residual diethyl ether. The solution was aliquoted and stored at -80°C.

Verification of T-domain/SfP interaction

Approximately 100 µM of the holo-NikP1AT was mixed in a solution that contained 50 mM HEPES, pH=8.0, 250 µM Bodipy-CoA, 200 nM SfP, and 200 mM magnesium chloride. The reaction was incubated for 1 hour at room temperature and the reaction mixture was separated on a 12% SDS-PAGE gel with the location of the Bodipy-CoA verified via transilluminator at 300 nm. Batches that did not contain Bodipy at the same molecular weight as the protein were used immediately for downstream experiments. Batches that did contain Bodipy at the protein's molecular weight were considered apo- protein and the batch was subsequently treated with free CoA in the presence of SfP.

In a similar manner, the serine residue on the PCP necessary for phosphopantetheine transfer was verified to be exposed using the same technique as holo-NikP1AT. However, unlike the AT domain, SDS-PAGE was used to verify the presence of Bodipy at the molecular weight of the GST-PCP$_{Tyr7}$ fusion product. If Bodipy was not present at the correct molecular weight, the protein batch was discarded with the assumption that it was irreparably misfolded.

Aminoacylation of holo-NikP1AT with L-Histidine

The reaction conditions are modified from previous procedures [24, 44]. A reaction mixture of containing 50 mM HEPES, pH=8.0, 200 mM magnesium chloride, 20 mM L-Histidine, and 200 µM holo-NikP1AT were incubated at room temperature for 1 hour followed by incubation at 4^{o}C for 1 hour. The solution was desalted into 100 mM HEPES, pH=7.5 followed by verification by SEC, which also served as a purification step to remove non-aminoacylated NRPS. The protein was flash-frozen and stored at -80^{o}C.

UV-Vis measurements

All measurements were made on an Agilent 8453 UV-Vis Spectrophotometer using quartz cuvettes (Starna Cells, Inc.) with a path length of 10 mm and a 4 mm slit width with or without an anaerobic screw-cap. The ferric spectrum was obtained by adding 5 µM protein with 50 mM HEPES + 0.3 molar equivalents of methyl viologen and degassing for 15 minutes prior to a spectrum being taken. The reduced species was observed by taking the ferric sample and adding 1.5 - 2 molar equivalents of sodium dithionite. The ferrous-CO complex was produced by adding carbon monoxide to the reduced species and obtaining a spectrum after several seconds. The spectrum of the P450sky/His-NikP1AT complex involved incubating 5 µM of P450sky with 10 µM His-NikP1AT on ice for 1 hour, centrifuging the sample at 4ºC at 16000 rpm for 10 minutes and observing the signal.

Titrations were carried out on P450sky with imidazole and sodium cyanide, two ligands that bind tightly to more traditional P450s, such as CYP101A1. 100 µM imidazole was titrated into 5 µM enzyme and incubated for one minute for each data point, for a total of ten. Separately, 5 mM sodium azide was titrated with 5 µM P450sky and incubated for 1 minute for each data point, for a total of ten. These data were analyzed using OriginPro 8.6 software, with the dissociation constants determined by fitting with the Michaelis-Menten equation.

Characterization of the P450_{sky}/His-NikP1AT complex

In an Eppendorf tube, a mixture of 10 µM P450sky and 100 µM His-NikP1AT were incubated on ice for 2 hours then spun down at 4ºC at 16000 rpm for 5 minutes. The protein mixture was then run through a 0.22 um filter and injected onto an ATKA FPLC (GE Healthcare) equilibrated with 100 mM HEPES, pH=7.5 and 150 mM sodium chloride. The flow rate was set to 0.15 mL/min and a fraction collector was set up to collect in 0.5 mL aliquots. Following the run, the fractions were observed on the UV-Vis at both 280 nm (aromatic residues) and 417 nm (heme). The heme-containing fractions were verified on a 12% SDS-PAGE gel to confirm the presence of both proteins.

Measurement of the P450sky-oxy complex by Stopped-flow

The measurement of the decay rate of the ferrous-oxy complex was performed on an SX20 Stopped-flow spectrophotometer (Applied Photophysics) for accurate visualization and rate measurements. The temperature of the experiment was set to 4ºC and data was collected either utilizing a PDA set up in logarithmic mode for 1 second with 1000 time points or using a PMT detector with 5000 time points. 5 µM of P450_{sky} in 50 mM HEPES, pH=7.5 with the addition of 0.3 molar equivalents of methyl viologen was degassed with nitrogen, reduced with two molar equivalents of sodium dithionite, and loaded onto syringe A, previously washed with sodium dithionite followed by degassed buffer. Syringe B consists of 50 mM HEPES, pH=7.5 supplemented with 2 mM O_2. The data was visualized as well as fit to a single exponential using Applied Photophysics Pro-Data SX software.

EPR measurements

Spectra of the low-spin enzyme were collected on an EMXplus X-band EPR (Bruker) at 16K with 12 mW power and a microwave frequency of 9.834 GHz. 20 scans from 400-4000 gauss were averaged to obtain a final spectrum. The data were collected and analyzed on either Bruker Xenon software suite or the SpinCount software package. Determination of the g-values were performed by the use of the equation g = (71.4484v) / B, where magnetic field, B (mT) and the microwave frequency, v (GHz). Ferric samples were set up with 200 µL of 800 µM protein as-purified, pipetted into an iron-free quartz EPR tube, and flash-frozen in liquid nitrogen. Ferrous samples involved 200 µL of 400 µM enzyme and reduced anaerobically in the presence of 0.3 molar equivalents of methyl viologen and excess sodium dithionite.

Crystal structure of substrate-free P450sky

The as-purified enzyme was diluted to a 5 mg/mL concentration for use in the crystallography wells. The mother-liquor consists of 225 mM ammonium chloride, 20% PEG 6000 and drops were set up using a hanging-drop method with 2 µL mother-liquor followed by the addition of 2 µL of protein. The trays were then stored at 25^{o}C with crystals forming after an average of 7 days in the form of thick plates approximately 500 µm in length. The crystals were incubated in 25% glycerol as a cryo-protectant and flash-frozen in liquid nitrogen for shipping to SER-CAT at the Argonne National Laboratory. Data were collected on beamline 22ID using a 1 second exposure time per frame. A total of 180 frames were collected and used for data reduction. The diffraction images were integrated by Dr. Lesa Offermann, whom also performed molecular replacement on the data using a previously solved P450sky structure (PDBID: 4L0E) as a template. The process of structure refinement was carried out with winCOOT and Phenix [45].

2.3 RESULTS

Small ligand binding of $P450_{sky}$

The purified protein exhibits a Soret maximum at 417 nm (Figure 2.1), typical of low-spin P450s [23]. The $A_{417/280}$ is around 1.5, indicating a pure sample of enzyme as determined by SDS-PAGE. The extinction coefficient was determined to be 118 $mM^{-1}cm^{-1}$ as determined by the pyridine hemochromagen assay [46], in close agreement with the 115 $mM^{-1}cm^{-1}$ extinction coefficient observed for some other P450s, e.g. CYP101A1 [47].

The addition of small molecule ligands can gauge the accessibility of the heme-active site of the enzyme to the outside environment. The addition of imidazole to P450sky results in a change of the Soret maximum from 417 nm to 424 nm (Figure 2.2), which is the typical for the addition of a nitrogen-containing ligand bound to the distal site of a thiolate-bound heme [48]. The calculated K_D for imidazole is 732 μM, which is roughly two orders of magnitude larger than for P450s that recognize and metabolize a variety of small molecules [49, 50]. The K_D of P450sky in the presence of L-His-NikP1AT is 703 μM, demonstrating no effective change in small molecule entry and binding in the pocket (Figure 2.3). The addition of a smaller and anionic ligand, such as cyanide, also demonstrates difficulty in accessing the active site of the protein. The Soret of the enzyme shifts from 417 nm to 430 nm (Figure 2.4). Fitting this spectroscopic change results in a K_D of 19.8 mM, which is around one order of magnitude higher than prototypical P450s, such as CYP101A1 or CYP102A1 [51, 52]. This low affinity for small molecules may be insightful given the necessity for an enzyme/PCP complex for amino acid hydroxylation. It is possible that, in the absence of T-domain binding, that access through the active-site channel is restricted.

SEC profiles for the P450sky/L-His-NikP1AT complex

A complex is formed between $P450_{sky}$ and the loaded NikP1AT didomain, with elution peaks for P450sky at 58 mins, L-His-NikP1AT at 54 mins, and the complex at 48 mins, which generates a shoulder that pre-elutes with the AT domain. However, the additive molecular weight of the complex is off the column is smaller than what is calculated. The elution profile resembles the timing for the P450nikQ/apo-NikP1AT complex rather than the P450nikQ/L-His-NikP1AT complex. This suggests that P450sky is either interacting with the A-domain in a non-catalytic manner reminiscent of the P450nikQ/apo-NikP1AT interaction or this method of binding inherently favors a different geometry with the complex. As previously mentioned, there is no change in the spin-state with L-His-NikP1AT when incubated with P450sky, so the complex may not be catalytically relevant due to the lack of any interaction with the T-domain (Figure 2.5).

Binding of P450sky with apo-PCP_{Tyr7}

There appears to be no binding between the apo-PCP_{Tyr7} and P450sky. This may be due to multiple factors, including that the T-domain is still attached to the GST solubility tag or, as mentioned earlier, an inability for T-domain binding in a form other than the aminoacylated state. However, the ability for SfP to recognize the core of the protein in order to transfer the PPant to the serine residue shows that the serine's surrounding residues are available for recognition. Aside from solubility issues stemming from cleavage of the solubility tag from the T-domain, there is difficulty discerning between 50 kDa and 60 kDa on an S-200 SEC column and facilitates the necessity for a larger tag in order to notice the difference between the bound and unbound forms of P450sky. The inability to bind to the apo T-domain suggests that there may be non-catalytic binding with the A-domain of the aminoacylated NikP1AT didomain and that the A-domain provides some level of recruitment for the P450 after the transfer of the PPant by the pathway's native phosphopantetheinyl transferase. This also supports observations made with the nikkomycin system, which demonstrates no complex formation between P450nikQ and the holo-didomain (possibly due to a different modular conformation), but some type of complex formation with the apo- and aminoacylated-didomain.

The addition of excess L-His-NikP1AT to P450sky does not exhibit any recognizable optical changes. For example, no shift from a low-spin to high-spin state is observed, which P450sky undergoes with native T-domains if loaded with the cognate amino acid substrate [21]. This may be due to the enzyme not binding in a catalytically relevant way but also may be that P450sky does not acquire a spin-shift with histidine. The three residues that are natively metabolized (phenylalanine, O-methyltyrosine, and leucine) are not charged, so it is unknown how the effects of a weakly basic residue will affect the substrate entry into the active site and/or how it is oriented in the distal pocket. An array of free amino and fatty acids, of which included L-tyrosine, L-tryptophan, L-leucine, L-glycine, L-β-alanine, L-methionine, and L-histidine were added in >100-fold excess and results in no spin-shift regardless of the polarity or shape of the molecule (Figure 2.6). This is confirmed by the works of Cryle and Walsh that only a loaded T-domain, possibly specific to the skyllamycin pathway, will cause a spin-shift and subsequent catalysis by the enzyme.

Optical Characterization of P450sky

In order to quantify how much P450 enzyme is in an actively useful form is generally determined through the binding of a hard ligand, such as the spectrum in Figure 2.1 showing the ferrous-CO complex. The dissociation constant for CO to P450 enzymes are in the low nanomolar range and the k_{off} is extremely slow [53-55]. Upon binding, the Soret band of P450sky shifts from 417 nm to 450 nm, with approximately 80% of the enzyme successfully completing this transition. The Qx and Qy components of the Q-bands merge into one broad peak, indicative of the presence of an intact thiolate ligand [49, 56, 57]. However, unlike CYP101A1 which maintains a stable P450 spectrum, the 450 nm spectrum quickly decays with the Soret band transitioning to 420 nm, indicating a displacement of the iron-thiolate ligand. This is similar to P450nikQ, which quickly achieves an 85% transition of the Soret to 450 nm and quickly depletes. This may also indicate that more enzyme is active, but the initial spectrum is unable to be ascertained due to the time between the addition of sodium dithionite and the initialization of the first spectrum on the UV-Vis.

The fully reduced spectrum in Figure 2.1 displays a Soret shift from 417 nm to 410 nm, which is similarly observed in other P450s as well as P450nikQ [58, 59]. The ferrous form of the enzyme is, as expected, highly sensitive to the presence of molecular oxygen, with the Soret immediately shifting from 410 nm back to its ferric location at 417 nm. However, when the formation of the ferrous-oxy complex was observed (Figure 2.7), the wavelength of the Soret remained at 417 nm, but with a greatly reduced extinction coefficient reminiscent of human cytochrome P450 3A4 [60], which is also observed to have a redox potential lower than average at -200 mV in a similar spin-state [61]. This differs from most P450s, which shows a shift in the Soret band to the vicinity of 430-435 nm, as is also the case with P450nikQ [58, 62]. Therefore, this may be a normal occurrence for P450s with unusually low redox potentials. In addition to the decreased 417 nm extinction coefficient for the reduced species, the rate of autoxidation is also several orders of magnitude greater than with most other p450s [60, 63-65], with a ferrous-oxy decay rate of 147 s^{-1}. It is currently unknown why the rate of ferrous-oxy autoxidation is high in P450sky compared to other P450 enzymes.

Electronic Paramagnetic Resonance spectroscopy of P450sky

P450sky shows a clean S=1/2 signal indicative of a ferric P450 as-purified, with g-values of 2.42, 2.24, and 1.92 (Figure 2.7). These are expected in unbound, low-spin P450 enzymes [66-69]. However, there is a small shoulder attached to the g_z signal that has a value of 2.48, but could be due to the presence of imidazole that remained following dialysis [70, 71]. There are also peaks at 2.04 and 2.00 indicative of a contaminant copper(II) signal present within the cavity at the time of data collection and not due to its presence in the sample itself [72]. Unfortunately, there is no data concerning the bound P450sky/L-His-NikP1AT complex available at this time. Should there be a shift in the g-values, then it would be likely that the substrate is present in the active site, with the histidine residue ligating to the heme.

2.4 DISCUSSION

Multiple NRPS systems have been studied in the context of their own operon products, such as the P450-based β-hydroxylation chemistry performed by the nikkomycin system [18, 24], the diiron monooxygenase β-hydroxylation chemistry performed by the chloramphenicol system [17], as well as P450-based aryl crosslinking reactions for the vancomycin-derived antibiotics [73-75]. While the study of these as closed systems has reached its pinnacle, there is untapped potential concerning the cross-reactivity of exogenous enzymes to their non-native NRPS counterparts. These studies involving individual components of various systems would be ideal since each system may have issues concerning solubility, expression, or rarity of substrate that may prohibit the study of these systems *in vitro* or *in vivo* due to the cost necessary to work around these issues. One potential issue preventing the immediate use of these types of systems is the unknown compatibility and recognition between components of two different systems. However, the idea of combining components from homologous systems with similar enzymes or chemistries may prove to be a good starting point for future research.

The identification of a homologous pair of systems became the primary priority, with emphasis on systems that perform the same chemistry. In this case, both the skyllamycin and nikkomycin pathways work with P450 enzymes that utilize the canonical mechanism associated with CYP101A1, by hydroxylating their respective amino acids at the β-carbon and maintaining a reliance on redox partners for 1+1 electron transfer [76]. The two P450s share a 34% identity and a 53% similarity, so they share a high enough likeness to each other that they can be used in this experiment (EMBOSS needle alignment). While the P450s are homologous, the NRPS systems are not, as P450sky works with three different modules incorporated in multi-modular NRPS and $\text{P450}_{\text{nikQ}}$ operates with a unimodular NRPS. However, this difference in NRPS structure provides an advantage, as the NikP1 gene is a single, soluble protein that contains only a di-domain for the module instead of three or more that are present in each protein for Sky30-32. Unfortunately, since the residues necessary for complex recognition are unknown for both systems, the surfaces of the two P450s cannot be properly compared for compatibility.

Several notable points have been made by Wise *et al*. concerning the behavior of the nikkomycin system. For instance, SEC elution profiles show that the unbound apo- and L-His-NikP1AT elute at the same point in time while the holo-NRPS elutes at a later time point. P450nikQ was demonstrated to interact with NikP1AT if the NRPS is in either its apo or aminoacylated form. However, it was noted that there appears to be two forms of this interaction, with the $\text{P450}_{\text{nikQ}}$/apo-NikP1AT complex eluting from an S-200 size exclusion column later and at a smaller calculated molecular weight than expected compared to P450nikQ/L-His-NikP1AT (Figure 2.8), which elutes at the properly calculated molecular weight. P450nikQ shows no apparent affinity for holo-NikP1AT, but this is justified with the different elution pattern from unbound holo-NikP1AT in comparison to apo- and L-His-NikP1AT. There is currently no evidence suggesting whether the same binding pattern would apply with P450nikQ to the apo-, holo-, or aminoacylated-PCP domain.

Work presented by Ullmann and Cryle on the skyllamycin system have demonstrated a lack of affinity between the P450 and the apo- or holo-PCP domain [36]. There is data that compares the binding of the P450 with its three associated PCPs that have been aminoacylated with various hydrophobic and bulky amino acids, as well as enantiomers of the recognized amino acids for each T-domain [21]. The results show that the tethered amino acid does alter the recognition of the hydroxylase with the T-domain to some degree, demonstrating that the amino acid to some extent assists targeting by the hydroxylase to the NRPS to form a β-hydroxylation product, which may be involved in downstream processes like an intramolecular Fischer condensation-leading to a pharmacologically-active depsipeptide.

Comparison of these points may assist in explaining the results of the chromatogram between P450sky and L-His-NikP1AT (Figure 2.9). For instance, the similarity in the elution profiles compared to P450nikQ and apo-NRPS may suggest that the PCP is not the sole force in the recognition motif, assuming that the apo-NRPS is still in a position that is favorable to receive a PPant, rather than binding to the hydroxylase and preventing the ability to become catalytically relevant. In addition, histidine, a weakly basic amino acid, is not tethered to any of the PCPs that are recognized by P450sky, which prefers hydrophobic or neutral amino acids [21]. The method of entry for the tethered amino acid through the channel of the P450 is currently unknown and inhibits our knowledge concerning the importance of amino acid recognition. Therefore, the T-domain may not be interacting with the hydroxylase, which would also support the lack of an observable spin-shift upon the addition of excess NRPS to P450sky. It would be interesting to observe the effect of transplanting one of the PCP domains associated with the skyllamycin pathway in the place of the PCP attached to NikP1AT and again run SEC to see if the elution of the complex occurs at a similar place as with P450nikQ/L-His-NikP1AT.

The maintenance of the P450nikQ/NikP1 complex in the presence of high salt has been determined to be driven predominantly by hydrophobic forces. So, in the homologous P450sky/NikP1 system, it may be inferred that the interaction is also driven by hydrophobic forces. Granted, the concentration of sodium chloride during the SEC run is 150mM, compared to the 500mM present with the P450nikQ interaction, but the evidence that the exterior of the protein have a similar charge density gives credence that the interaction of P450sky with NikP1 is driven by hydrophobicity. The interaction between CmlA and CmlP, albeit a different system with different tertiary and quaternary structure for the hydroxylase, do not maintain a complex throughout an SEC run. There is also no sign of a complex with the use of a native-PAGE gel either. This could allude to a greater variety of interaction events between systems concerning a mixed use of electrostatic or hydrophobic forces driving the interaction.

2.5 CONCLUSION

In summary, P450sky is a homolog of P450nikQ and behaves in a similar manner, with substrate recognition dependent on attachment to a recognized PCP domain. P450sky from the skyllamycin pathway is demonstrated to interact with the NRPS di-domain from the nikkomycin pathway, a cross-system interaction that may prove interesting when designing custom NRPS biosynthetic pathways. However, the interaction does not appear to create a P450sky/L-His-NikP1AT complex that is catalytically relevant. This is most likely due to the hydroxylase interacting with the A-domain, but with little or no recognition for the PCP domain of the NikP1 module. The mode of binding, whether hydrophobic or electrostatic, is unknown, but similarity between the two hydroxylases may infer that the interaction between P450sky and NikP1 may also be hydrophobic. The future direction of this project would transplant a hydroxylated PCP from the skyllamycin into the nikkomycin NRPS and test for functionality, either with SEC or through substrate turnover experiments.

2.6 REFERENCES

[1] Reimmann, C., Patel, H. M., Serino, L., Barone, M., Walsh, C. T., and Haas, D. (2001) Essential PchG-dependent reduction in pyochelin biosynthesis of Pseudomonas aeruginosa, *J Bacteriol 183*, 813-820.

[2] O'Brien, D. P., Kirkpatrick, P. N., O'Brien, S. W., Staroske, T., Richardson, T. I., Evans, D. A., Hopkinson, A., Spencer, J. B., and Williams, D. H. (2000)

Expression and assay of an N-methyltransferase involved in the biosynthesis of a vancomycin group antibiotic, *Chem Commun*, 103-104.

[3] Stachelhaus, T., and Walsh, C. T. (2000) Mutational analysis of the epimerization domain in the initiation module PheATE of gramicidin S synthetase, *Biochemistry-Us 39*, 5775-5787.

[4] Linne, U., and Marahiel, M. A. (2000) Control of directionality in nonribosomal peptide synthesis: role of the condensation domain in preventing misinitiation and timing of epimerization, *Biochemistry-Us 39*, 10439-10447.

[5] Chen, H., and Walsh, C. T. (2001) Coumarin formation in novobiocin biosynthesis: beta-hydroxylation of the aminoacyl enzyme tyrosyl-S-NovH by a cytochrome P450 NovI, *Chem Biol 8*, 301-312.

[6] Miller, D. A., and Walsh, C. T. (2001) Yersiniabactin synthetase: probing the recognition of carrier protein domains by the catalytic heterocyclization domains, Cy1 and Cy2, in the chain-initiating HWMP2 subunit, *Biochemistry-Us 40*, 5313-5321.

[7] Walsh, C. T., Chen, H. W., Keating, T. A., Hubbard, B. K., Losey, H. C., Luo, L. S., Marshall, C. G., Miller, D. A., and Patel, H. M. (2001) Tailoring enzymes that modify nonribosomal peptides during and after chain elongation on NRPS assembly lines, *Curr Opin Chem Biol 5*, 525-534.

[8] Pohle, S., Appelt, C., Roux, M., Fiedler, H. P., and Sussmuth, R. D. (2011) Biosynthetic gene cluster of the non-ribosomally synthesized

cyclodepsipeptide skyllamycin: deciphering unprecedented ways of unusual hydroxylation reactions, *J Am Chem Soc 133*, 6194-6205.

[9] Wright, G. D. (2003) Mechanisms of resistance to antibiotics, *Curr Opin Chem Biol 7*, 563-569.

[10] Aharonowitz, Y., and Friedrich, C. G. (1980) Alanine dehydrogenase of the beta-lactam antibiotic producer Streptomyces clavuligerus, *Arch Microbiol 125*, 137-142.

[11] Hoehn, P., Ghisalba, O., Moerker, T., and Peter, H. H. (1995) 3'-Demethoxy-3'-hydroxystaurosporine, a novel staurosporine analogue produced by a blocked mutant, *J Antibiot (Tokyo) 48*, 300-305.

[12] Billich, A., and Zocher, R. (1987) N-Methyltransferase Function of the Multifunctional Enzyme Enniatin Synthetase, *Biochemistry-Us 26*, 8417-8423.

[13] Tercero, J. A., Espinosa, J. C., Lacalle, R. A., and Jimenez, A. (1996) The biosynthetic pathway of the aminonucleoside antibiotic puromycin, as deduced from the molecular analysis of the pur cluster of Streptomyces alboniger, *J Biol Chem 271*, 1579-1590.

[14] Davies, J., and Wright, G. D. (1997) Bacterial resistance to aminoglycoside antibiotics, *Trends Microbiol 5*, 234-240.

[15] Wright, G. D. (2005) Bacterial resistance to antibiotics: enzymatic degradation and modification, *Adv Drug Deliv Rev 57*, 1451-1470.

[16] Long, K. S., Poehlsgaard, J., Kehrenberg, C., Schwarz, S., and Vester, B. (2006) The Cfr rRNA methyltransferase confers resistance to Phenicols,

Lincosamides, Oxazolidinones, Pleuromutilins, and Streptogramin A antibiotics, *Antimicrob Agents Chemother 50*, 2500-2505.

[17] Makris, T. M., Chakrabarti, M., Munck, E., and Lipscomb, J. D. (2010) A family of diiron monooxygenases catalyzing amino acid beta-hydroxylation in antibiotic biosynthesis, *Proc Natl Acad Sci U S A 107*, 15391-15396.

[18] Chen, H., Hubbard, B. K., O'Connor, S. E., and Walsh, C. T. (2002) Formation of beta-hydroxy histidine in the biosynthesis of nikkomycin antibiotics, *Chem Biol 9*, 103-112.

[19] Mootz, H. D., Schwarzer, D., and Marahiel, M. A. (2000) Construction of hybrid peptide synthetases by module and domain fusions, *Proc Natl Acad Sci U S A 97*, 5848-5853.

[20] Schneider, A., Stachelhaus, T., and Marahiel, M. A. (1998) Targeted alteration of the substrate specificity of peptide synthetases by rational module swapping, *Mol Gen Genet 257*, 308-318.

[21] Uhlmann, S., Sussmuth, R. D., and Cryle, M. J. (2013) Cytochrome p450sky interacts directly with the nonribosomal peptide synthetase to generate three amino acid precursors in skyllamycin biosynthesis, *ACS Chem Biol 8*, 2586-2596.

[22] Haslinger, K., Brieke, C., Uhlmann, S., Sieverling, L., Sussmuth, R. D., and Cryle, M. J. (2014) The structure of a transient complex of a nonribosomal peptide synthetase and a cytochrome P450 monooxygenase, *Angew Chem Int Ed Engl 53*, 8518-8522.

[23] Schenkman, J. B., and Jansson, I. (2006) Spectral analyses of cytochromes P450, *Methods Mol Biol 320*, 11-18.

[24] Wise, C. E., and Makris, T. M. (2017) Recruitment and Regulation of the Non-ribosomal Peptide Synthetase Modifying Cytochrome P450 Involved in Nikkomycin Biosynthesis, *ACS Chem Biol 12*, 1316-1326.

[25] Lewis, D. F. V., and Hlavica, P. (2000) Interactions between redox partners in various cytochrome P450 systems: functional and structural aspects, *Bba-Bioenergetics 1460*, 353-374.

[26] Guenzi, E., Galli, G., Grgurina, I., Gross, D. C., and Grandi, G. (1998) Characterization of the syringomycin synthetase gene cluster. A link between prokaryotic and eukaryotic peptide synthetases, *J Biol Chem 273*, 32857-32863.

[27] Finking, R., and Marahiel, M. A. (2004) Biosynthesis of nonribosomal peptides, *Annu Rev Microbiol 58*, 453-488.

[28] Stachelhaus, T., Mootz, H. D., and Marahiel, M. A. (1999) The specificity-conferring code of adenylation domains in nonribosomal peptide synthetases, *Chem. Biol. 6*, 493-505.

[29] Belshaw, P. J., Walsh, C. T., and Stachelhaus, T. (1999) Aminoacyl-CoAs as probes of condensation domain selectivity in nonribosomal peptide synthesis, *Science 284*, 486-489.

[30] Ackerley, D. F., Caradoc-Davies, T. T., and Lamont, I. L. (2003) Substrate specificity of the nonribosomal peptide synthetase PvdD from Pseudomonas aeruginosa, *J Bacteriol 185*, 2848-2855.

[31] Winn, M., Fyans, J. K., Zhuo, Y., and Micklefield, J. (2016) Recent advances in engineering nonribosomal peptide assembly lines, *Nat Prod Rep 33*, 317-347.

[32] Clugston, S. L., Sieber, S. A., Marahiel, M. A., and Walsh, C. T. (2003) Chirality of peptide bond-forming condensation domains in nonribosomal peptide synthetases: the C5 domain of tyrocidine synthetase is a (D)C(L) catalyst, *Biochemistry-Us 42*, 12095-12104.

[33] Kohli, R. M., Takagi, J., and Walsh, C. T. (2002) The thioesterase domain from a nonribosomal peptide synthetase as a cyclization catalyst for integrin binding peptides, *Proc Natl Acad Sci U S A 99*, 1247-1252.

[34] Trauger, J. W., Kohli, R. M., and Walsh, C. T. (2001) Cyclization of backbone-substituted peptides catalyzed by the thioesterase domain from the tyrocidine nonribosomal peptide synthetase, *Biochemistry-Us 40*, 7092-7098.

[35] Reimer, J. M., Aloise, M. N., Harrison, P. M., and Schmeing, T. M. (2016) Synthetic cycle of the initiation module of a formylating nonribosomal peptide synthetase, *Nature 529*, 239-242.

[36] Kokona, B., Winesett, E. S., von Krusenstiern, A. N., Cryle, M. J., Fairman, R., and Charkoudian, L. K. (2016) Probing the selectivity of beta-hydroxylation reactions in non-ribosomal peptide synthesis using analytical ultracentrifugation, *Anal Biochem 495*, 42-51.

[37] Blatti, J. L., Beld, J., Behnke, C. A., Mendez, M., Mayfield, S. P., and Burkart, M. D. (2012) Manipulating fatty acid biosynthesis in microalgae for biofuel through protein-protein interactions, *PLoS One 7*, e42949.

[38] Vance, S., Tkachenko, O., Thomas, B., Bassuni, M., Hong, H., Nietlispach, D., and Broadhurst, W. (2016) Sticky swinging arm dynamics: studies of an acyl carrier protein domain from the mycolactone polyketide synthase, *Biochem J 473*, 1097-1110.

[39] Nguyen, C., Haushalter, R. W., Lee, D. J., Markwick, P. R., Bruegger, J., Caldara-Festin, G., Finzel, K., Jackson, D. R., Ishikawa, F., O'Dowd, B., McCammon, J. A., Opella, S. J., Tsai, S. C., and Burkart, M. D. (2014) Trapping the dynamic acyl carrier protein in fatty acid biosynthesis, *Nature 505*, 427-431.

[40] Lelyveld, V. S., Brustad, E., Arnold, F. H., and Jasanoff, A. (2011) Metal-Substituted Protein MRI Contrast Agents Engineered for Enhanced Relaxivity and Ligand Sensitivity, *J Am Chem Soc 133*, 649-651.

[41] Costa, S. J., Coelho, E., Franco, L., Almeida, A., Castro, A., and Domingues, L. (2013) The Fh8 tag: a fusion partner for simple and cost-effective protein purification in Escherichia coli, *Protein Expr Purif 92*, 163-170.

[42] Goldman, S., Kim, R., Hung, L. W., Jancarik, J., and Kim, S. H. (1998) Purification, crystallization and preliminary X-ray crystallographic analysis of Pyrococcus furiosus DNA polymerase, *Acta Crystallogr D Biol Crystallogr 54*, 986-988.

[43] La Clair, J. J., Foley, T. L., Schegg, T. R., Regan, C. M., and Burkart, M. D. (2004) Manipulation of carrier proteins in antibiotic biosynthesis, *Chem Biol 11*, 195-201.

[44] Huang, Q., Zhou, X. L., Hu, Q. H., Lei, H. Y., Fang, Z. P., Yao, P., and Wang, E. D. (2014) A bridge between the aminoacylation and editing domains of leucyl-tRNA synthetase is crucial for its synthetic activity, *Rna 20*, 1440-1450.

[45] Adams, P. D., Afonine, P. V., Bunkoczi, G., Chen, V. B., Davis, I. W., Echols, N., Headd, J. J., Hung, L. W., Kapral, G. J., Grosse-Kunstleve, R. W., McCoy, A. J., Moriarty, N. W., Oeffner, R., Read, R. J., Richardson, D. C., Richardson, J. S., Terwilliger, T. C., and Zwart, P. H. (2010) PHENIX: a comprehensive Python-based system for macromolecular structure solution, *Acta Crystallogr D Biol Crystallogr 66*, 213-221.

[46] Barr, I., and Guo, F. (2015) Pyridine Hemochromagen Assay for Determining the Concentration of Heme in Purified Protein Solutions, *Bio Protoc 5*.

[47] Gunsalus, I. C., and Wagner, G. C. (1978) Bacterial P-450cam methylene monooxygenase components: cytochrome m, putidaredoxin, and putidaredoxin reductase, *Methods Enzymol 52*, 166-188.

[48] Dawson, J. H., Andersson, L. A., and Sono, M. (1982) Spectroscopic investigations of ferric cytochrome P-450-CAM ligand complexes. Identification of the ligand trans to cysteinate in the native enzyme, *J Biol Chem 257*, 3606-3617.

[49] Bui, S. H., McLean, K. J., Cheesman, M. R., Bradley, J. M., Rigby, S. E., Levy, C. W., Leys, D., and Munro, A. W. (2012) Unusual spectroscopic and ligand binding properties of the cytochrome P450-flavodoxin fusion enzyme XplA, *J Biol Chem 287*, 19699-19714.

[50] Muralidhara, B. K., Negi, S., Chin, C. C., Braun, W., and Halpert, J. R. (2006) Conformational flexibility of mammalian cytochrome P450 2B4 in binding imidazole inhibitors with different ring chemistry and side chains. Solution thermodynamics and molecular modeling, *J Biol Chem 281*, 8051-8061.

[51] Sono, M., and Dawson, J. H. (1982) Formation of Low-Spin Complexes of Ferric Cytochrome P-450-Cam with Anionic Ligands - Spin State and Ligand Affinity Comparison to Myoglobin, *J Biol Chem 257*, 5496-5502.

[52] Girvan, H. M., Levy, C. W., Williams, P., Fisher, K., Cheesman, M. R., Rigby, S. E., Leys, D., and Munro, A. W. (2010) Glutamate-haem ester bond formation is disfavoured in flavocytochrome P450 BM3: characterization of glutamate substitution mutants at the haem site of P450 BM3, *Biochem J 427*, 455-466.

[53] Debey, P., Balny, C., and Douzou, P. (1973) Low temperature studies of microsomal cytochrome P450 flash photolysis experiments, *FEBS Lett 35*, 86-90.

[54] Gray, R. D. (1982) Kinetics and mechanism of carbon monoxide binding to purified liver microsomal cytochrome P-450 isozymes, *J Biol Chem 257*, 1086-1094.

[55] Oertle, M., Richter, C., Winterhalter, K. H., and Di Iorio, E. E. (1985) Kinetics of carbon monoxide binding to phenobarbital-induced cytochrome P-450 from rat liver microsomes: a simple bimolecular process, *Proc Natl Acad Sci U S A 82*, 4900-4904.

[56] Chenge, J. T., Duyet, L. V., Swami, S., McLean, K. J., Kavanagh, M. E., Coyne, A. G., Rigby, S. E. J., Cheesman, M. R., Girvan, H. M., Levy, C. W., Rupp, B., von Kries, J. P., Abell, C., Leys, D., and Munro, A. W. (2017) Structural Characterization and Ligand/Inhibitor Identification Provide Functional Insights into the Mycobacterium tuberculosis Cytochrome P450 CYP126A1, *J Biol Chem 292*, 1310-1329.

[57] McLean, K. J., Warman, A. J., Seward, H. E., Marshall, K. R., Girvan, H. M., Cheesman, M. R., Waterman, M. R., and Munro, A. W. (2006) Biophysical characterization of the sterol demethylase P450 from Mycobacterium tuberculosis, its cognate ferredoxin, and their interactions, *Biochemistry 45*, 8427-8443.

[58] Luthra, A., Denisov, I. G., and Sligar, S. G. (2011) Spectroscopic features of cytochrome P450 reaction intermediates, *Arch Biochem Biophys 507*, 26-35.

[59] Egawa, T., Hishiki, T., Ichikawa, Y., Kanamori, Y., Shimada, H., Takahashi, S., Kitagawa, T., and Ishimura, Y. (2004) Refolding processes of cytochrome P450cam from ferric and ferrous acid forms to the native conformation. Formations of folding intermediates with non-native heme coordination state, *J Biol Chem 279*, 32008-32017.

[60] Denisov, I. G., Grinkova, Y. V., Baas, B. J., and Sligar, S. G. (2006) The ferrous-dioxygen intermediate in human cytochrome P450 3A4. Substrate dependence of formation and decay kinetics, *J Biol Chem 281*, 23313-23318.

[61] Das, A., Grinkova, Y. V., and Sligar, S. G. (2007) Redox potential control by drug binding to cytochrome P450 3A4, *J Am Chem Soc 129*, 13778-13779.

[62] Couture, M., Stuehr, D. J., and Rousseau, D. L. (2000) The ferrous dioxygen complex of the oxygenase domain of neuronal nitric-oxide synthase, *J Biol Chem 275*, 3201-3205.

[63] Grinkova, Y. V., Denisov, I. G., Waterman, M. R., Arase, M., Kagawa, N., and Sligar, S. G. (2008) The ferrous-oxy complex of human aromatase, *Biochem Biophys Res Commun 372*, 379-382.

[64] Ost, T. W., Clark, J., Mowat, C. G., Miles, C. S., Walkinshaw, M. D., Reid, G. A., Chapman, S. K., and Daff, S. (2003) Oxygen activation and electron transfer in flavocytochrome P450 BM3, *J Am Chem Soc 125*, 15010-15020.

[65] Zhang, H., Gruenke, L., Arscott, D., Shen, A., Kasper, C., Harris, D. L., Glavanovich, M., Johnson, R., and Waskell, L. (2003) Determination of the rate of reduction of oxyferrous cytochrome P450 2B4 by 5-deazariboflavin adenine dinucleotide T491V cytochrome P450 reductase, *Biochemistry-Us 42*, 11594-11603.

[66] Peisach, J., and Blumberg, W. E. (1970) Electron paramagnetic resonance study of the high- and low-spin forms of cytochrome P-450 in liver and in liver microsomes from a methylcholanthrene-treated rabbit, *Proc Natl Acad Sci U S A 67*, 172-179.

[67] Tsai, R., Yu, C. A., Gunsalus, I. C., Peisach, J., Blumberg, W., Orme-Johnson, W. H., and Beinert, H. (1970) Spin-state changes in cytochrome P-450cam on binding of specific substrates, *Proc Natl Acad Sci U S A 66*, 1157-1163.

[68] Kumaki, K., Sato, M., Kon, H., and Nebert, D. W. (1978) Correlation of type I, type II, and reverse type I difference spectra with absolute changes in spin state of hepatic microsomal cytochrome P-450 iron from five mammalian species, *J Biol Chem 253*, 1048-1058.

[69] Davydov, R., Im, S., Shanmugam, M., Gunderson, W. A., Pearl, N. M., Hoffman, B. M., and Waskell, L. (2016) Role of the Proximal Cysteine Hydrogen Bonding Interaction in Cytochrome P450 2B4 Studied by Cryoreduction, Electron Paramagnetic Resonance, and Electron-Nuclear Double Resonance Spectroscopy, *Biochemistry-Us 55*, 869-883.

[70] Morita, H., Yoshikawa, H., Takizawa, T., Shirai, M., Akahori, F., and Yoshimura, T. (2006) The formation of g=2.49-species of cytochrome P450 in the rat liver by PCB126 oral administration: identification of heme axial ligands by EPR spectroscopy, *Biosci Biotechnol Biochem 70*, 2974-2981.

[71] Conner, K. P., Cruce, A. A., Krzyaniak, M. D., Schimpf, A. M., Frank, D. J., Ortiz de Montellano, P., Atkins, W. M., and Bowman, M. K. (2015) Drug modulation of water-heme interactions in low-spin P450 complexes of CYP2C9d and CYP125A1, *Biochemistry-Us 54*, 1198-1207.

[72] Chandra, S., and Sangeetika, X. (2004) EPR, magnetic and spectral studies of copper(II) and nickel(II) complexes of schiff base macrocyclic ligand derived from thiosemicarbazide and glyoxal, *Spectrochim Acta A Mol Biomol Spectrosc 60*, 147-153.

[73] Woithe, K., Geib, N., Zerbe, K., Li, D. B., Heck, M., Fournier-Rousset, S., Meyer, O., Vitali, F., Matoba, N., Abou-Hadeed, K., and Robinson, J. A. (2007) Oxidative phenol coupling reactions catalyzed by OxyB: a cytochrome P450 from the vancomycin producing organism. implications for vancomycin biosynthesis, *J Am Chem Soc 129*, 6887-6895.

[74] Cryle, M. J., Meinhart, A., and Schlichting, I. (2010) Structural characterization of OxyD, a cytochrome P450 involved in beta-hydroxytyrosine formation in vancomycin biosynthesis, *J Biol Chem 285*, 24562-24574.

[75] Peschke, M., Brieke, C., and Cryle, M. J. (2016) F-O-G Ring Formation in Glycopeptide Antibiotic Biosynthesis is Catalysed by OxyE, *Sci Rep 6*, 35584.

[76] Holden, M., Mayhew, M., Bunk, D., Roitberg, A., and Vilker, V. (1997) Probing the interactions of putidaredoxin with redox partners in camphor

P450 5-monooxygenase by mutagenesis of surface residues, *J Biol Chem 272*, 21720-21725.

Figures

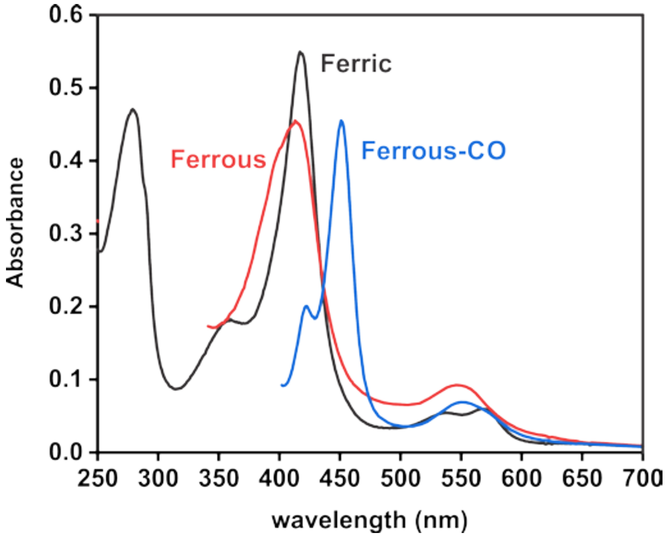

Figure 2.1: Optical characterization of P450sky. 5 µM of enzyme is present for the ferric (black), ferrous (red), and ferrous-CO (blue) complex of P450sky. The ferrous species was determined with 0.3 molar equivalents of methyl viologen (shown as a shoulder at 395 nm) and excess sodium dithionite. The ferrous-CO species was taken with the addition of CO to anaerobic ferric enzyme with methyl viologen and the addition of excess sodium dithionite.

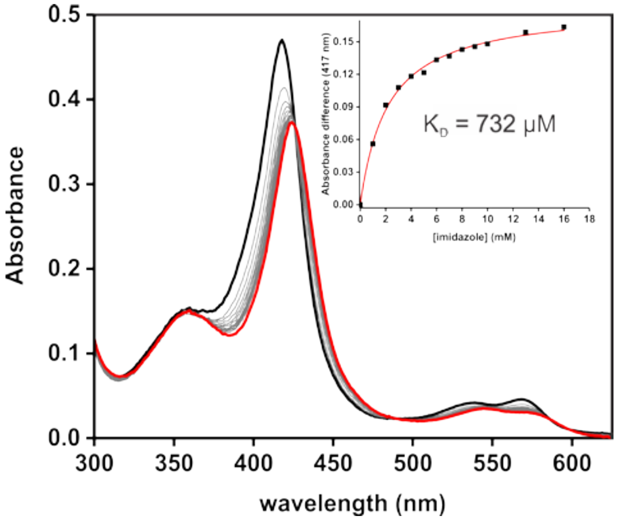

Figure 2.2: Determination of the KD of imidazole through the optical change of the Soret of P450sky. The dissociation constant was determined using 4.5 µM of unbound P450sky. Fitting the shift in the spectrum from 417 nm to 424 nm with a Michaelis-Menten plot gives a K_D = 732 µm. This suggests that the channel to the active site of the enzyme is closed to small molecule ligands when unbound to recognized T-domain.

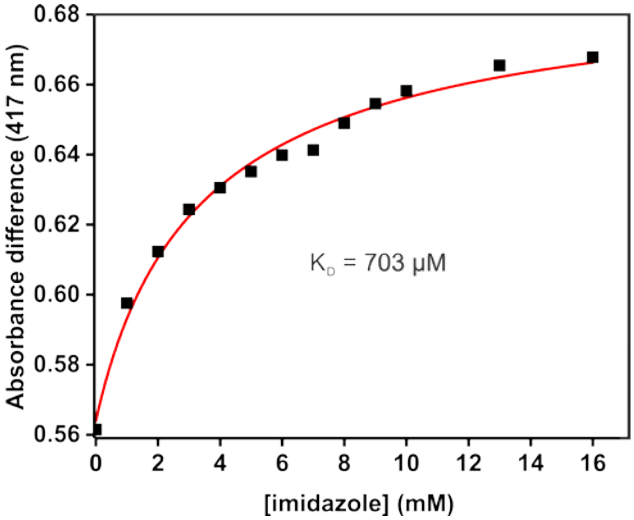

Figure 2.3: Determination of the K_D of imidazole in the presence of P450sky and L-his-NikP1AT through the optical change of the Soret of P450sky. The dissociation constant determined with the 5 µM P450sky and 50 µM L-His-NikP1AT, as in Figure 2. There is negligible change in the K_D, suggesting the lack of binding to the P450 to the T-domain of the NRPS.

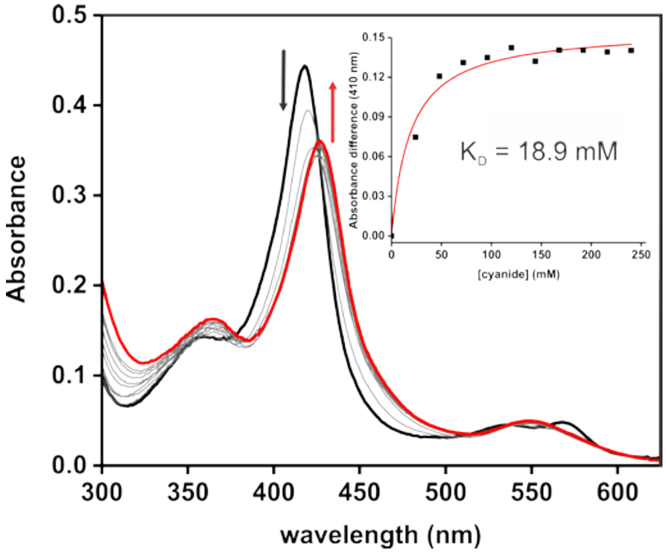

Figure 2.4: Determination of the K_D of cyanide through the optical change of the Soret of P450sky. The dissociation constant was calculated with 4.5 µM of non-NRPS bound P450sky. The shift from 417 nm to 430 nm is expected for the binding of a carbon ligand to the porphyrin. The high K_D = 18.9 mM suggests the channel of the active site is both closed and/or does not prefer anionic charges entering guiding the entrance into the channel. A spectrum of a cyanide titration in the presence of NRPS-bound P450sky was not taken.

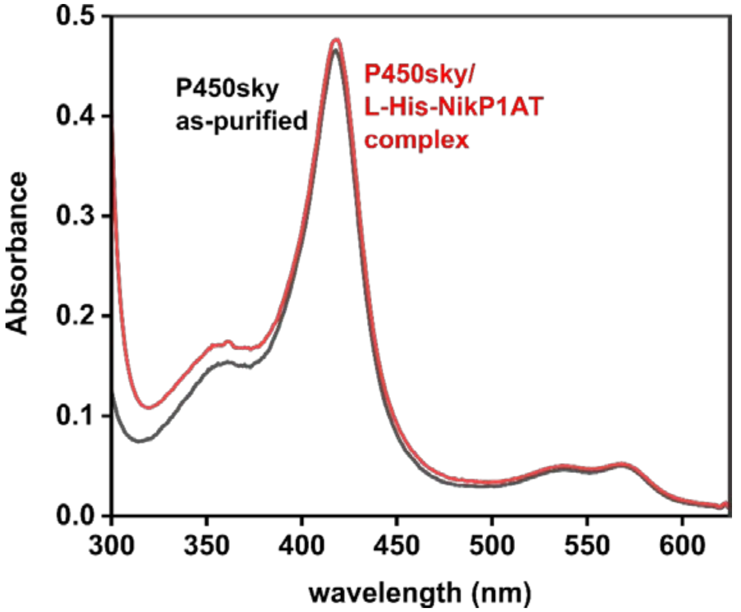

Figure 2.5: Optical spectra of P450sky and P450sky in the presence of L-his-NikP1AT. Overlay shows 5 µM P450sky without (black) and bound (red) to 75 µM L-his-NikP1AT. Note the lack of high-spin formation at 392 nm and static Q-bands from 500-600 nm.

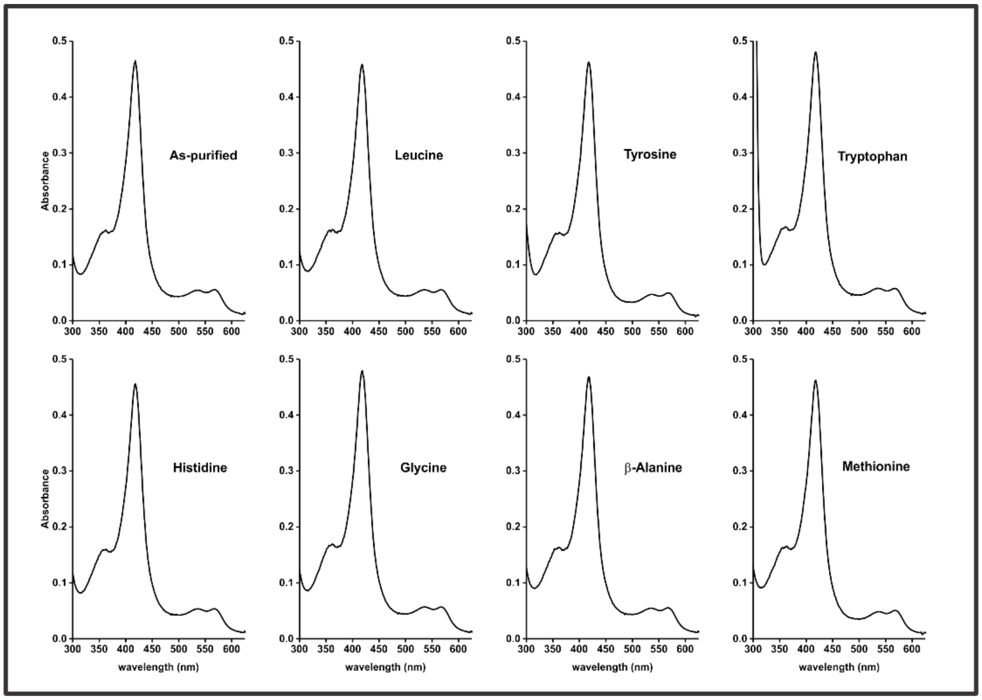

Figure 2.6: Optical spectra of P450sky with amino acids. The profiles show 4.5 µM – 5 µM P450sky incubated with at least >100-fold free amino acids. Note the lack of spin-shift in the Soret maximum, indicating that free amino acid either not entering the active site or is not displacing the water ligand from the porphyrin of the enzyme.

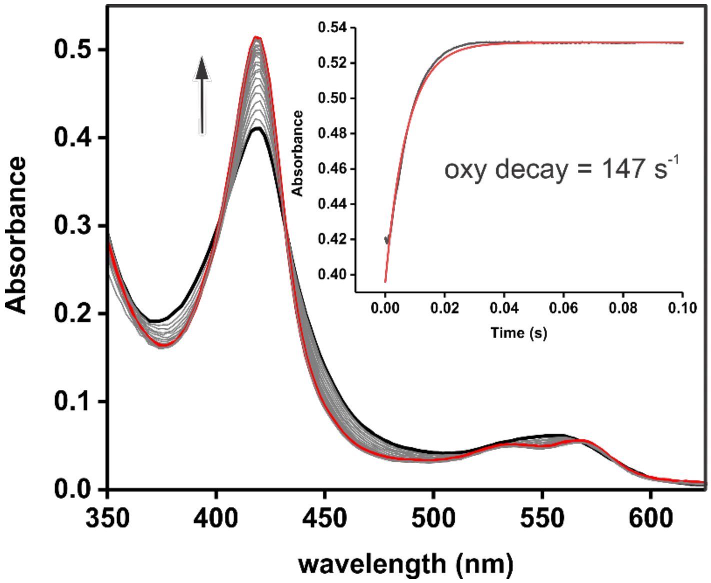

Figure 2.7: Decay of the P450sky oxy complex. The complex was formed with 5 µM ferrous P450sky mixed with 1 mM molecular oxygen on the Stopped-flow. There is no hyspochromic shift generally observed with formation of a ferrous-oxy complex, usually present in the the 430-440 nm range. In contrast, the extinction coefficient decreases with no shift in the Soret. The Q-bands split from a single peak back to the two recognized in the ferric spectrum. The rate of autoxidation more quickly than in other P450s.

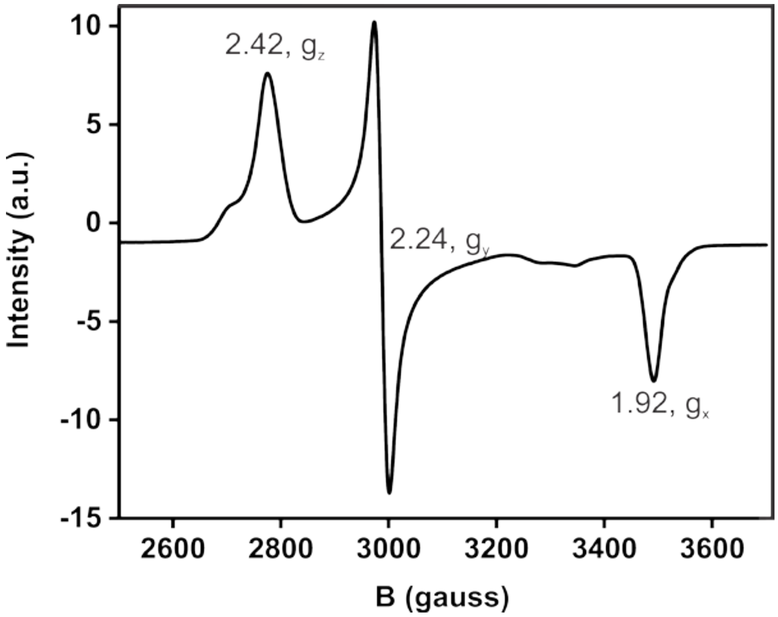

Figure 2.8: EPR of ferric, low-spin P450sky. The spectrum shows 400 µM unbound P450sky using X-band EPR. The g-values align with other P450 spectra in a low-spin state. Peaks between 3250 and 3350 gauss are products of a copper contaminant in the cavity of the instrument.

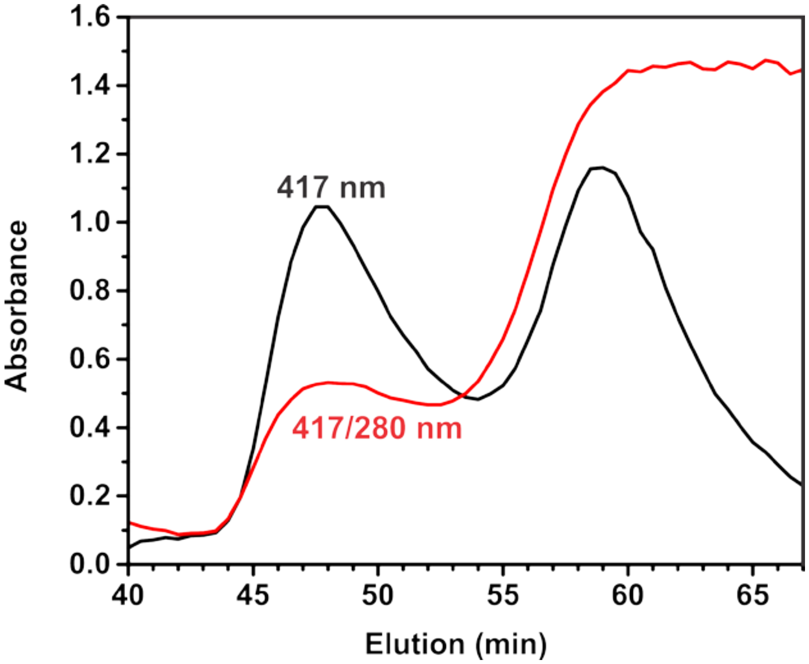

Figure 2.9: Size-exclusion chromatograph of the P450nikQ/L-his-NikP1AT complex. The profiles show P450nikQ (black) and the P450nikQ/L-His-NikP1AT complex (red) at a 1:10 mixture. The elution peak at 48 minutes is around 125 kDa. The elution peak at 58 minutes represents is around 50 kDa, representative of the presence of free P450. The decrease in the 417/280 nm ratio at 48 minutes for the complex is due to the aromatics present in the NRPS that is co-eluting with the P450. The absorbance increases for the ratio at 58 minutes, which is the ratio observed with purified P450nikQ.

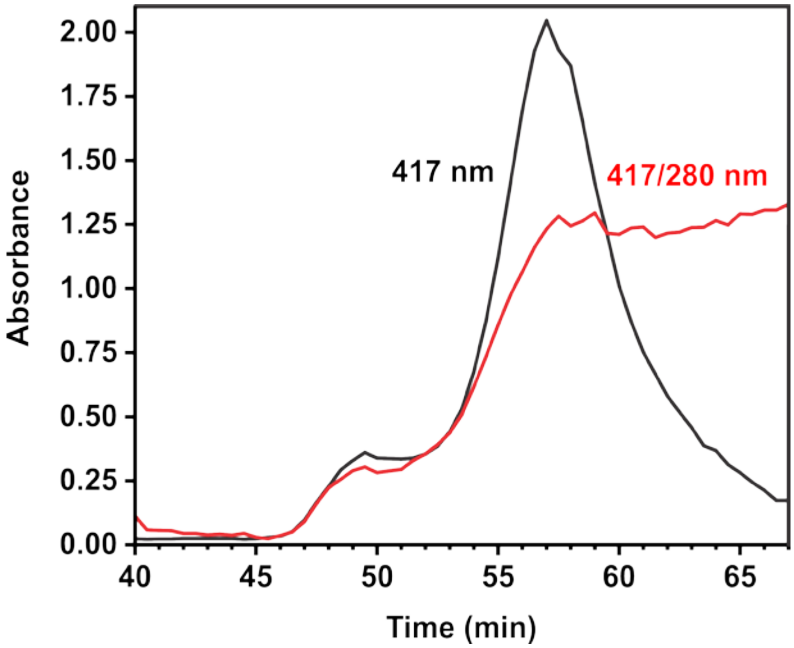

Figure 2.10: Size-exclusion chromatograph of the P450nikQ/L-his-NikP1AT complex. The profiles show P450sky (black) and the P450sky/L-His-NikP1AT complex (red) at a 1:10 ratio. The complex elutes at 49.5 minutes, coinciding with 105 kDa and is similar to the behavior of the complex between P450nikQ and L-His-NikP1AT. Unbound P450sky elutes at 58 minutes, corresponding to 50 kDa.

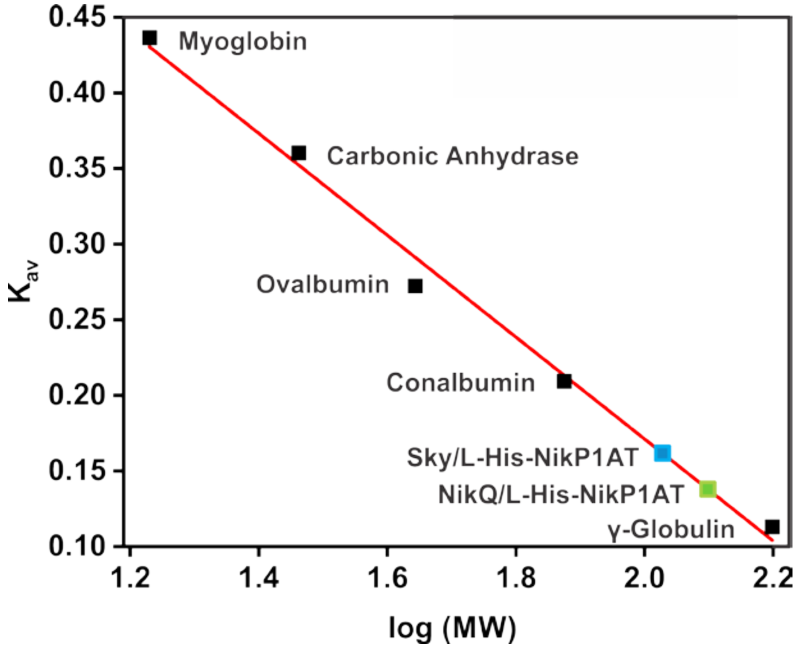

Figure 2.11: Chromatographic partition coefficients (K_{av}) of the hydroxylase/NRPS complexes. The plot shows the K_{av}s for the protein standards and the corresponding hydroxylase/NRPS complexes as a function of the log of molecular weight.

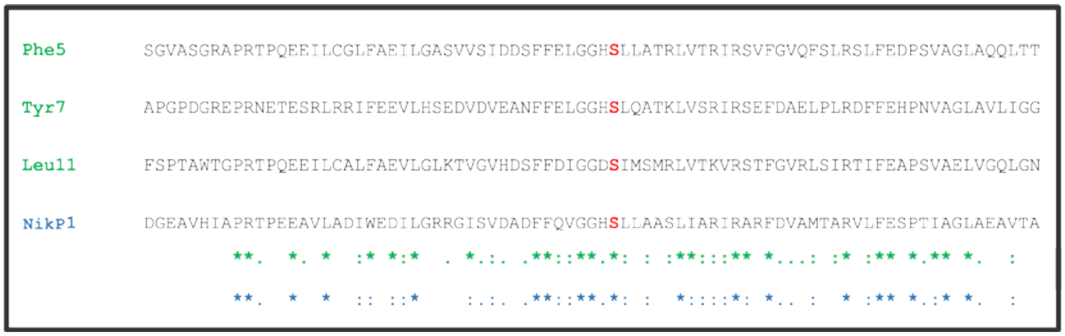

```
Phe5    SGVASGRAPRTPQEEILCGLFAEILGASVVSIDDSFFELGGHSLLATRLVTRIRSVFGVQFSLRSLFEDPSVAGLAQQLTT

Tyr7    APGPDGREPRNETESRLRRIFEEVLHSEDVDVEANFFELGGHSLQATKLVSRIRSEFDAELPLRDFFEHPNVAGLAVLIGG

Leu11   FSPTAWTGPRTPQEEILCALFAEVLGLKTVGVHDSFFDIGGDSIMSMRLVTKVRSTFGVRLSIRTIFEAPSVAELVGQLGN

NikP1   DGEAVHIAPRTPEEAVLADIWEDILGRRGISVDADFFQVGGHSLLAASLIARIRARFDVAMTARVLFESPTIAGLAEAVTA
                **.  *. *  :* *:*  . *.:. .**::**.*: : :**:::** *...: :* :** *.** *.  :

                **.  *  *  :: ::*    :.:. .**::**.*: :  *::::*: *.. :  * :** *.:* *.  :
```

Figure 2.12: Sequence alignment for PCPs of skyllamycin and nikkomycin pathways. PCPs natively hydroxylated by P450sky are shown in green and with the addition of the sequence for the NikP1AT PCP in blue. The phosphopantetheinylated serine residue is shown in red. The sequences are similar and suggests the possibility of interactions between the NRPS and the hydroxylase.

```
Sky             MTAHTLPIPDDISTINLTDPRTYEVNDLSEYWRQLRTTRPLYWHPPVGDAPGFWVVSRYA
NikQ            ------------MRVDLSDPLLYRDSDPEPVWSRLRAEHPVYRNER-ANGEHFWAVMTHG
                              ::*:**  *. .* .  * :**: :*:* :   .:.  **.*  :.

Sky             DVMALYKDNKKLTSEKGNVLVTLLAGGDSAAGKMLAVTDGAMHRGLRNVLLKSFSPQALK
NikQ            LCTDMLTDPRVFSSQNGMRLDSDPQVLAAAAGKMLNITDPPRHDKIRKVVSSAFTPRMVS
                    : .* : ::*::*  * :      :****** :**   *  :*:*: .:*:*: :.

Sky             PIVDQIRVNTTRLVVDAARRGECDFAADVAEQIPLNTISDLLGVPAADREFLLKLNKSAL
NikQ            RLEATMRETAAKAIDEALAAGECEFT-RVAQKLPVSVICDMLGVAPADWDFMVERTRFAW
                 :   :* .::: : :*   ***:*:  **:::*:..*.*:***  ** :*::: .: *

Sky             SSEDADQSA-TDAWLARNEILLYFSELVAERRAKPTEDVISVLANSMVDGKPLTEEVIVL
NikQ            SSTALDEAEEARKVRAHTEILLHFQDLAAERRREPKDDLMSALVCGEIDGAPLTDQEILY
                **   *::  :    *:.****:*.:*.**** :*.:*::*.*. . :** ***:: *:

Sky             NCYSLILGGDETSRLSMIDSVQTFTQYPDQWELLRDGKVTLESATEEVLRWATPAMHFGR
NikQ            NCDALVSGGNETTRHATVGGLLALIDNPDQWHRLRDEPALMPSAIQEIVRYTSPVMHALR
                ** :*: **:**:* : :..: :: : ****. ***  . : ** :*::*:::*.**  *

Sky             RAVTDMELHGQVIAAGDVVTLWNNSANRDEEVFADPYAFDLNRSPNKHITFGYGPHFCLG
NikQ            TATEDVEFGGERISAGDHVVAWLPSANRDEKVFDDPDRFDIEREPNRHLGFIQGNHYCIG
                 *. *:*: *: *:*** *. *  ******:** **  **::*.**:*: *  * *:*:*

Sky             AYLGRAEVHALLDALRTYTTGFEITGEPQRIHSNFLTGLSRLPVRIQPNEAAIAAYDSDN
NikQ            SSLAKLELTVMFEELLARVEVAELAGQVRRLRSNLLWGFDSLPVKFVPRA----------
                : *.: *: .::: * : .   *::*: :*::**:* *:. ***:: *.

Sky             GVRS
NikQ            ----
```

Figure 2.13: Sequence alignment for P450sky and P450nikQ. The cysteine that provides the thiolate ligand to the porphyrin is in red. The site of interaction at the F and G helices with the T-domain are in green. There is strong similarity in the G helix, however, more variability is present in the F helix.

CHAPTER 3

THE SUBSTITUTION OF MANGANESE-PROTOPORPHYRIN IX INTO CYTOCHROME P450OLET

3.1 INTRODUCTION

The incorporation of non-native porphyrin cofactors in heme enzymes represents a powerful tool to systematically alter the chemistry, reactivity, spectroscopic properties, or redox potential of enzymes that utilize porphyrin as a co-factor. In its idealized form, this methodology represents a means to retain a complex polypeptide in a native state, preserving critical features of the secondary coordination sphere that are exquisitely tuned to enable substrate recognition, ligand binding, and small molecule activation, among others [1-4]. Historically, many of the protocols that have aimed to substitute porphyrins in heme-enzymes have involved harsh conditions that either partially or fully denature the protein [5, 6]. This includes the removal of the axial ligand through protonation at low pH, and extraction of the porphyrin in a suitable organic solvent [7]. The newly-introduced porphyrin is then added to the denatured protein, followed by careful alteration of the buffer environment to promote proper refolding. For some proteins (e.g. globins) this procedure works reasonably well due to the nature of the more weakly-bound axial ligand (histidine) and exposed nature of the heme in the final folded state [8]. Cytochrome P450s, on the other hand, have been notoriously difficult proteins for heme-exchange studies due to stronger bonding of the iron to the axial ligand (thiolate) and the buried nature of the heme. As a result, reconstitution studies have only reported in a handful of studies due to the low-yield of final protein (typically ~ 5%).

Recently, a number of different strategies have explored the use of *in vivo* pathways for novel heme incorporation. The Marletta laboratory has devised a technique that utilizes the RP523 cell line for porphyrin incorporation, eliminating the need for harsh unfolding conditions [9]. To achieve this, the RP523 cell line of *E. coli* was utilized which contains a knockout of the hemB, a gene that encodes for a zinc enzyme involved in the second step in the biosynthesis of hemin and synthesizes monopyrrole porphyobilinogen from two molecules of 5-aminolevulinic acid [10-13]. This inhibits the production of hemin and consequently promotes the production of the apo-enzyme. An added advantage of this cell line is that the cell wall and membrane are both permeable to non-native hemes that are added to the culture medium [14]. However, a drawback of this procedure is that it requires an anaerobic culture environment due to the lack of production of heme-enzymes such as catalase that are necessary for the detoxification of reactive oxygen species.

Another attractive method involves the co-expression of heme transporters that are utilized by a number of prokaryotes (including pathogenic bacteria) for the uptake of heme. ChuA is a 69-kDa heme receptor located in the outer membrane of *E. coli* O157:H7 that scavenges heme from the surrounding environment under iron-replete conditions [15, 16]. The importation of iron ions works with the cooperation of the siderophore aerobactin and the siderophore importer TonB, which chelates iron and transports the metal to the cytosol [17, 18]. The mechanism for ChuA (Figure 3.1) emphasizes bypasses the need for an iron chelator and the holo-porphyrin can be directly recognized and imported by ChuA into the periplasmic space. Once inside the periplasmic space, the porphyrin is shuttled to the inner membrane by the periplasmic binding protein (PBP), an ATP-binding cassette (ABC) transport protein for movement across the inner membrane into the cytosol [19].

When overexpressed, the ChuA protein proposedly results in a decrease in production of native heme, leading to the incorporation of any non-native porphyrin in the cytosol by the expressed proteins. The only detraction of using this method is the necessity for minimal media, which acts to further decrease the production of native Fe-Protoporphyrin IX [20]. However, since the presence of the added porphyrin can be added at high levels, there is little concern over the incorporation of hemin into the protein of interest. The co-expression of ChuA with a gene of interest can also result in an increase in holo-protein production compared to normal *E. coli* strains that rely on the bacterial porphyrin biosynthetic pathway due to higher concentrations of cytosolic heme [21, 22].

ChuA has been previously used to incorporate Fe-deuteroporphyrin IX into P450BM3 as a tool to determine if the method can be applied to a thiolate-ligated porphyrin enzyme [20]. In conjunction with minimal media, there was 99 % incorporation of the Fe-DPIX into the P450, compared to 63 % when the same procedure was attempted in Luria Broth. Other metallo-PPIXs have been incorporation into cytochrome c to test for effects on activity and inhibition [23].

Although the porphyrins were transported into the cytosol, there were issues with incorporation of zinc and tin based porphyrins into the protein, suggesting that factors such as sterics or electronics may be important factors when attempting to express metalloproteins *in vivo*. Nonetheless, the ChuA system has proven to be a useful tool in concert with directed evolution, with the incorporation of non-native porphyrins into high-throughput screens that test both metal and amino acid substitutions. Brustad and Arnold demonstrated that, in conjunction with *in silico* analysis and a high-throughput testing of modified proteins, that enzymes could be screened for enhanced activity for a native substrate [24]. Although these systems illustrate the value of porphyrin incorporation into a protein scaffold, there are few instances where these proteins have been studied beyond the level of product turnover assays.

The cytochrome P450 OleTJE presents an ideal scaffold for pursuing reactivity studies of high-valent metal oxos. The ability to rapidly activate H2O2, combined with possible contributions from the porphyrin electronics, allows for the stable formation of a highly-accumulating ferryl-oxo π-cation intermediate (Compound I) in the presence of native substrate [25]. The significant kinetic isotope effect of Compound I decay substantiates the need for quantum tunneling for the hydrogen abstraction step [26-28]. Following the hydrogen abstraction step, hydrogen bonds originating from a water molecule stabilized by the carboxylate of the fatty acid and His85 may be involved in stabilization of the ferryl-hydroxo intermediate [29]. The mechanism beyond this point is unclear. However, the fatty acid decarboxylates and Compound II slowly decays over several hundred milliseconds to the starting ferric, low-spin state [30]. The long lifetime of these intermediates make P450oleTJE ideal for testing the spectropscopic properties of this enzyme with porphyrins containing non-iron metals.

As a proof of concept, we have adapted the ChuA coexpression for the incorporation of Mn-PPIX in cytochrome P450oleTJE. Optical spectroscopic and reactivity studies have been used to optimize conditions for high-level incorporation of a non-native metal-containing porphyrin into the enzyme. The reactivity of high-valent Mn-oxo complex with fatty acid substrates is reported.

3.2 MATERIALS AND METHODS

Synthesis of Manganese-Protoporphyrin IX

The synthesis of Mn-PPIX involved minor modifications of existing protocols [31, 32]. In a round bottom flask containing 20 mL pyridine, 100 mg of protoporphyrin IX (Sigma Aldrich) was mixed with 725 mg manganese (II) chloride and refluxed for either 6 hours or until the four characteristic Q-bands of the free PPIX merged into two bands (Qx and Qy). The synthesis was followed by UV-Vis with dissolution in pyridine. The round bottom flask was cooled to room temperature and its contents poured into a separatory funnel. 80 mL of 200 mM HCl were added to the solution to solubilize any unbound metal and the solution was vigorously mixed. 20 mL of chloroform were added to the solution and mixed vigorously, with the organic phase (containing the porphyrin) collected. This procedure was repeated three additional times on the aqueous layer until no color was observed in the organic layer. The porphyrin was crystallized by evaporating the chloroform with a stream of nitrogen for 8 hours. The contents of the container were collected and weighed for percent recovery measurements, usually ranging from 98% - 104%. The purity was verified again determined by dissolving the final product in DMSO and taking an optical measurement and confirming that the metal was not labile during the extraction process.

Expression of Manganese-PPIX OleT

pChuA, pLys, and p283-P450oleTJE Y110C vectors were co-transformed into BL21 (Dε3) chemically competent cells. The function of the pLys gene is to reduce the minimal amounts of T7 polymerase with the use of T7 lysozyme until the culture is properly induced [33]. A single colony from the transformation was selected and used to inoculate an overnight culture consisting of LB media. 10 mL of the overnight culture were used to inoculate one liter cultures of modified M9 minimal media recipe consisting of the following ingredients: 12.8 g sodium phosphate, dibasic, 3 g sodium phosphate, monobasic, 0.5 g sodium chloride, 1 g ammonium chloride, 0.5% glycerol, 2 mM magnesium sulfate, 0.1 mM calcium chloride, 0.1% casamino acids, 0.05 g kanamycin, 0.1 g ampicillin, and 0.02 g chloramphenicol. The culture was the incubated at 37°C, 210 rpm until OD_{600}=0.5, when the temperature was lowered to 20°C and 400 µM magnesium (II) chloride was added to each flask. The addition of the excess metal serves a two-fold purpose in both discouraging demetalation of the porphyrin and inhibit ferrocheletase from incorporating iron into endogenously produced porphyrin [34].

After 20 minutes, 10 mg of Mn-PPIX dissolved in DMSO were added to each liter of culture and incubated for 10 minutes, after which the plasmids were induced with 50 µM IPTG and allowed to incubate for 30 hours. The cultures were spun down at 6000 rpm for 15 minutes and stored at -80^{o}C until lysed.

Purification of Manganese-PPIX protein derivatives

Cells were re-suspended in 200 mL buffer consisting of 50 mM sodium phosphate, monobasic, pH=7.5, 300 mM sodium chloride, 10 mM imidazole (Buffer A) and lysed via sonication for six 2 minute cycles separated by 5 minutes of stirring on ice. The lysate was cleared by centrifugation for 40 minutes, 16000 rpm and the supernatant was decanted onto a 10 mL Ni-NTA column pre-equilibrated with Buffer A. The column was then washed with 30 column volumes of Buffer A + 10 mM imidazole and eluted with Buffer A + 240 mM imidazole. Ammonium sulfate was added to the elution at a final concentration of 25%, centrifuged, and decanted into a separate container. P450Olet was then salt-cut with ammonium sulfate to 60% and centrifuged. The supernatant was discarded and the pellet was resuspended with 100 mM potassium phosphate, pH=7.5 and dialyzed twice in buffer.

The solution was loaded onto DEAE resin equilibrated with 50 mM potassium phosphate, pH=7.5. The column was subsequently washed with phosphate buffer + 50 mM sodium chloride. The protein was eluted using a stepwise gradient of phosphate buffer supplemented with 100, 150, 200, 250, 300, 400, and 500 mM sodium chloride and the fractions containing porphyrin were pooled together. The protein was salt-cut and re-suspended to a final concentration of 70 µM prior to dialysis and storage at -80°C.

Pyridine Hemochromagen Assay

The conditions for the porphyrin hemochromes are similar to published methods [35]. For both PPIX-Olet and Mn-Olet, 500 µL of a 5 µM protein solution was diluted to 1 mL with a 40% pyridine/200 mM sodium hydroxide mixture and mixed. A spectrum of this oxidized sample was taken prior to the addition of solid sodium dithionite, when another spectrum was taken. Similar spectra were taken for an unquantified amount of Fe-PPIX and Mn-PPIX for comparative purposes and to account for contaminants during the preparation of the Mn-PPIX.

General Characterization of Mn-Olet

All measurements were made on an Agilent 8453 UV-Vis Spectrophotometer using quartz cuvettes (Starna Cells, Inc.) with a path length of 10 mm and a 4 mm slit width with or without an anaerobic screw-cap. The concentration of enzyme was calculated using an assumed extinction coefficient of 80 mM^{-1} cm^{-1}. The manganic form of the protein was taken with 5 µM of as-purified enzyme in 200 mM potassium phosphate, pH=7.5. The bound form of the spectrum was taken with treatment of 8 µM of as-purified enzyme with 48 µM C20H fatty acid solubilized with 30% Triton-X/70% ethanol at room temperature for 15 minutes followed by incubation on ice for 1 hour. The sample was spun down at 4°C and the spectrum taken.

The dissociation constant was determined by titration of eicosanoic acid to 5 µM of manganic enzyme and incubation overnight at 4ºC. The samples were centrifuged and measured. The increase of absorbance at 465 nm was plotted against the concentration of fatty acid and fit in OriginPro 2017 using a quadratic function (Morrison equation) reliable for the determination of tight dissociation constants, where A_{max} is the maximal absorbance change at ligand saturation, S is the concentration of eicosanoic acid, E_t is the concentration of enzyme, and K_d is the dissociation constant:

$$Aobs = \left(\frac{Amax}{2Et}\right)(S + Et + Kd) - (((S + Et + Kd)^2 - (4SEt))^{0.5})$$

The manganous form was obtained by first degassing 5 µM fatty acid bound enzyme with 250 nM methyl viologen for 30 minutes. Two molar equivalents of sodium dithionite solution were added to achieve a reduced spectrum. The high-valent oxo complex was observed with the addition of excess hydrogen peroxide to the reduced protein.

Stopped-flow kinetics of Mn-Olet

The measurement of the formation of the high-valent oxo intermediate required the use of an SX20 Stopped-flow spectrophotometer (Applied Photophysics) for accurate visualization and rate measurements. The temperature of the experiment was set to 4ºC and data were collected in logarithmic mode for 60 seconds with 5000 time points with the PDA detector and 5000 time points with the PMT detector. All data fittings and visualizations utilized the Applied Photophysics Pro-Data SX software. 10 µM enzyme present in excess proteated or deuterated eicosanoic acid was loaded into Syringe A with Syringe B containing one of the following oxidants: 5 mM hydrogen peroxide, 160 µM mCPBA, 3.2 mM sodium hypochlorite, or 5.2 mM peracetic acid. The reaction was mainly followed at 420 nm representing the increase of the high-valent oxo intermediate and 376 nm representing the decrease of the Soret band for the manganic form of the enzyme.

Rates were observed for the formation of the high-valent oxo intermediate at 420 nm, which corresponds to a partial depletion of the manganic Soret band at 376 nm, and fit using the following equation,

$$A_{t,obs} = A_{\infty} + \sum_{i=1}^{n} a_i \ e^{-t/t_i}$$

where $A_{t,obs}$ is the observed absorbance, a_i is the amplitude of phase i, t is time in seconds, and A_{∞} is the final absorbance of the trace. Collected data were fitted at 420 nm, the wavelength for the formation of the Mn-oxo intermediate. The traces were fitted using a two-summed exponential representing two distinct phases in the time trace, with the first phase showing the concerted decrease of the manganic Soret at 376 nm and increase of the high-valent oxo species at 420 nm followed by a slow decay phase. This slow decay is composed of two components: the decay of the high-valent oxo species to the manganic form and the overall degradation of the Soret bands as the protein is hydrolyzed in the presence of excess peracetic acid.

A Hammett plot for the reactivity of the high-valent oxo species for phenol derivatives involved hand-mixing 5 mM peracetic acid with 8 µM enzyme and aging for at least 30 seconds prior to loading into Syringe A. Syringe B contained 2 mM of one of the following: phenol, 4-methoxyphenol, 3-chlorophenol, 1,3-benzenediol, 1,4-benzenediol, or 4-cyanophenol. The rates were plotted as the log of the rate for the formation of the high-valent oxo species for each derivative divided by its rate of formation for phenol against the Hammett sigma constant for each derivative. A linear fit was used to determine the ρ-value, which indicates the nuleophilicity of the intermediate and the favorability of the reaction.

Analysis of turnover products

The protocol for turnover analysis has been used previously [30, 36]. In general, 2 mL of 5 µM enzyme supplemented with 500 µM of C20, C16, or C12 fatty acid were stirred at room temperature while a solution of 5 mM hydrogen peroxide was titrated at a rate of 2 mL/hr for approximately one hour. Four drops of concentrated HCl were subsequently added to quench the reaction and protonate excess fatty acid and the solution was mixed for an additional 10 minutes. The products and excess fatty acid were extracted from the aqueous phase with 4 mL chloroform, vortexed at maximum for 1 minute, and centrifuged at 2200 rpm for 3 minutes. The organic layer was transferred to glass vials, where the chloroform was evaporated on ice with a nitrogen stream. The contents were derivatized with 200 µL BSTFA:TMCS (Sigma-Aldrich, 99:1) for 60 minutes at 60°C. Samples were stored at -20°C to prevent degradation of the derivatized products.

Turnover products were analyzed with a Hewlett-Packard 5890 Series II Gas Chromatography (GC) instrument featuring a 30 m DB-5ms column with a column head pressure ranging from 7 and 15 psi and fitted with a flame ion detector. 7 µL of the derivatized sample were injected onto the GC and run on two potential programs depending on the initial fatty acid chain length. For chain lengths greater than C16, the following temperature gradient was established: 3 minutes at 170°C, 5°C/min to 260°C, 10°C/min to 320°C, 2 minutes at 320°C. For chain lengths less than C16, the following temperature gradient was used: 3 minutes at 50°C, 5°C/min to 170°C, 10°C/min to 280°C, 3 minutes at 280°C. All chromatograms were analyzed on HP ChemStation software.

3.3 RESULTS AND DISCUSSION

The synthesis of the Mn-PPIX was according to established protocols, with nearly 100% incorporation of the manganese metal into PPIX. As the oxidized form of the metal does not readily react with oxygen, the reaction did not require anaerobic conditions. Care was taken during the extraction process not to significantly lower the pH of the solution as this will result in demetalation of the porphyrin [37]. There are conflicting measurements concerning long-term storage causing the demetalation of Mn-porphyrins in aqueous solutions. In some cases, manganese porphyrins have been observed to demetalate in aqueous solutions [38, 39]. In other studies, no significant amount of free manganese ions present in solution over an extended period of time [40, 41]. To alleviate these potential issues, the extracted porphyrin was crystallized and stored at -20°C until further use. Furthermore, the required amount needed for growth was measured and solubilized in DMSO just prior to induction of *E. coli* cells. Using these procedures, there has been no evidence indicating the creation of free porphyrin in the final spectrum of the purified protein.

The presence of manganese in the purified enzyme was verified with the hemochromagen assay, which removes the protein scaffold and replaces the distal and proximal ligands of the metalloporphyrin with pyridine. The results show that there is no iron present in the sample, concluding that the porphyrin did not demetallate in solution and the intake of the required porphyrin outpaces the native production of the iron porphyrin (Figure 3.2). This is also verified by incubating a sample containing carbon monoxide with dithionite and not observing a distinct peak at 450 nm, the symbolic location for an iron-loaded P450 (Figure 3.3).

The spectrum of the protein as-purified contains a Soret peak at 376 nm, a red-shift of around 20 nm compared to the Soret maximum for manganese-reconstituted horseradish peroxidase (Mn-HRP) [42], and a blue-shift of around 10 nm compared to manganese-reconstituted P450 BM3 (CYP102A1, Mn-BM3) [43]. The Soret is reminiscent of manganese-reconstituted P450 CAM (CYP101), with the positioning of the features nearly identical to those observed for Mn-OleT, but lacks a pronounced shoulder at 420 nm [44]. It is currently not known whether the Soret differences among these P450s are due to positioning of the porphyrin or subtle difference in the thiolate ligand (e.g. hydrogen bonding). There appears to be minimal differences of the spectrum of Mn-Olet compared to what is observed with manganic myoglobin (Mn-Mb) [45]. There also a shoulder emanating at 420 nm that appears to be present, although in a diminished form, with Mn-Mb and Mn-HRP. The absorbance intensity is reminiscent of manganese-substituted P450 BM3, which portrays a more pronounced shoulder at wavelengths higher than the Soret maximum. A sharp, manganese-specific band emanates from 465 nm. Its ratio of $A_{465/376}$ = 0.15 is more subdued compared to Mn-HRP and Mn-Mb (~0.6-1.0), but not obliterated as is the case with P450s Mn-CYP101 and Mn-BM3. Q bands are present at 560 nm and 590 nm with an additional feature located at 515 nm. Mn-HRP shows Q bands located in a similar region. Mn-BM3 also contains identifiable Q-bands around 525 and 560 nm, similar to their placement in Mn-Olet.

Alterations in the spectrum are noticeable with the addition of C20 fatty acid (Figure 3.4). Unlike Fe-containing P450s, which can exhibit low- to high-spin (HS) shifts upon substrate binding, manganic porphyrins are HS regardless of ligand-binding due to occupancy of the σ* orbital at the d_{z^2} position, which is usually unoccupied in the unbound ferric porphyrin [46, 47]. As a result, the mechanism of this change has yet to be elucidated for Mn-OleT but may signal an environmental change at the thiolate-ligand. The titration of fatty acid to Mn-OleT causes neither shifting nor bleaching of the Soret. However, the Q bands become more pronounced at 550 nm and 585 nm. Other spectra have not been found to confirm the regularity of this behavior since the majority of proteins studies are derivatives of Mb, which start in a ferrous, high-spin state to facilitate binding of molecular oxygen [48]. There is a 1.7-fold increase in the feature at 465 nm with the titratable addition of fatty acid as well as a 2 nm hypsochromic shift.

Titration of the solvent (Triton-X/Ethanol) used to solubilize the eicosanoic acid did not yield a spectral change.

The reduced spectrum for Mn-Olet shows a shift in the 465 nm feature to 432 nm along with an increased prominence (Figure 3.5). In addition, the Soret shifts from 376 nm to 380 nm with a decrease in absorbance intensity to 75% of the original, manganic peak. The Soret behavior is not known for Mn-CYP101; however, the 465 nm feature also forms at around 430 nm with a strong, prominent absorbance. The drastic increase of this feature upon reduction is observed in synthetic manganese-porphyrins. Manganese(III)-meso-tetrapyridinyl-porphyrin (Mn(III)TPyP), in the presence of hydrogen peroxide, displays a bathochromic of the 465 nm feature and the decrease of the Soret [49]. The Soret shifts in this synthetic porphyrin as well, but to higher energy wavelengths and are not observed with Mn-Olet. The Q bands also become stronger while the 515 nm feature decreases, which is also observed in Mn(III)TPyP.

The generation of a high-valent Mn-oxo species was attempted using different oxidants, and led to differing results, summarized in Figure 3.6. There was little to no noticeable oxo formation in the presence of hydrogen peroxide. The addition of meta chloroperoxybenzoic acid (mCPBA) produced a stable oxo complex, but did not accumulate in high yields. There was a great amount of accumulation with sodium hypochlorite, with nearly half of the manganic form converted within one second. However, the species quickly decayed to a new species that most likely signaled the dissociation of the thiolate ligand from the porphyrin. The addition of peracetic acid yields similar quantities of oxo intermediate which remains stable for minutes when using low concentrations of oxidant. At higher concentrations (> 3 molar equivalents), the porphyrin absorbance decays until the signal is completely bleached. The high accumulation of the peracetic acid must be the oxidative species driving the creation of the oxo intermediate.

The absorbance of the Soret band reduces in intensity and shifts to a presumptive high-valent oxo species at 420 nm (Figure 3.7). The expected peroxide shunt pathway would result in a porphyrin that is oxidized by 2 redox equivalents relative to the starting state. In the case of reactions of Mn(III), this would be anticipated to generate a reactive Mn(V) or a Mn(IV) porphyrin pi-cation radical. The absorbance features of the latter would generate an absorbance feature in the visible region at wavelengths > 600 nm. Such a species is not evident from the rapid mixing studies shown here. Alternatively, it is also possible that a highly-reactive Mn(V)=O species is transiently generated but reduced rapidly by redox active amino acids from the protein framework (e.g. a nearby tyrosine and tryptophan) to generate a less-reactive Mn(IV) species. An example of this reaction is illustrated in Figure 3.8.

A scheme that summarizes the anticipated electronics of Mn(IV) and Mn(V) species are shown in Figure 3.9. The formation of the high-valent oxo intermediate is similar to those observed with Mn(IV)-BM3 and Mn(IV)-CYP101, with an increase in absorbance at 420 nm corresponding to a decrease in the manganic Soret at 376 nm. In order to study this intermediate, the manganic form of the enzyme was reacted against different oxidants, with the most stable mechanism used for study. In addition to the changes at 376 nm and 420 nm, peracetic acid bleaches the split Soret present at 465 nm and the manganic Q-bands while the addition of mCPBA or hypochlorite produce minimal yields of the high-valent species. The addition of sodium hypochlorite frees the porphyrin from the protein scaffold quickly after forming the high-valent intermediate, as the spectrum of the porphyrin aligns with free Mn-PPIX in aqueous solution after 30 seconds of incubation. Therefore, the peracetate was chosen for stopped-flow analysis of the presumed Mn(IV) intermediate. Alternatively, creation of the high-valent oxo species has been utilized with the addition of hydrogen peroxide to the manganous form of the enzyme and causing the formation of the peak at 420 nm, giving further credence that the high-valent oxo species produced is Mn(IV) rather than Mn(V) (Figure 3.10).

Kinetic data shows the presence of either two or three phases during the reaction of as-purified Mn-Olet with varying concentrations of peracetic acid, with kinetic traces at 420 nm summarized in Figure 3.11. The reciprocal relaxation times derived from multiple summed-exponential fitting are shown in Table 3.1. Provided that the first phase results from the generation of the oxo intermediate, the saturating behavior suggests a multi-step reaction in which an initial binding step in followed by an irreversible step. Such a scheme would be consistent with formation of the Mn(IV) species as a result of reduction from an exogenous source such as a redox-active amino acid. However, the origin of this first phase could also be the result of peracetate gaining quicker access to the active site in the portion of the sample that did not purify bound to palmitic acid, as is observed in the iron wild-type enzyme [25]. The second, slower growth phase is linearly dependent on peroxide, and may reflect this binding step. The third phase, present at higher concentrations of peracetic acid, is likely a slow decay phase that results from decomposition of the porphyrin, resulting in bleaching.

The kinetics of oxo formation were also examined in the presence of a FA substrate under saturating conditions and a fraction of the accumulation is observed. Under normal circumstances, this small molecule contaminant can be removed by treatment with a few molar equivalents of hydrogen peroxide followed by treatment with BioBeads to remove the alkene product. However, attempts at turnover with hydrogen peroxide with the Mn-substituted enzyme with saturating eicosanoic acid shows no formation of C19-alkene product, as determined by Gas Chromatography. So the use of it is unclear whether this approach will be particularly suitable for the Mn-substituted enzyme.

There is little accumulation of the high-valent oxo intermediate in the presence of eicosanoic acid, so the majority of this analysis involves enzyme that has been untreated with fatty acid prior to treatment with peracetic acid but still contains fatty acid contaminant from the purification process. In the presence of low concentrations of peracetate, the enzyme undergoes a quick burst-phase followed by a slow growth. Increasing the concentration of peracetate above a certain threshold created a third phase representing a slow decay. The first exponential for the formation of the 420 nm peak shows an initial rate of formation for the high-valent oxo intermediate of less than 1 s^{-1} with a peracetic acid concentration at 125-fold excess to the enzyme. Increasing the peracetate concentration above this threshold increases this initial rate to 5 s^{-1}. The composite spectrum extracted from SVD analysis (Figure 3.12) shows this phase reaches completion within five seconds post-mixing with peracetate while slower second phase completes the total accumulation of the oxo intermediate. The comparative quickness of this RRT compared to the latter rates is likely due to peracetate having ease of access to a portion of the sample that purifies non-fatty acid bound, as there likely is difficulty for the peracetate to enter the active site of the enzyme when longer chain fatty acids are bound to the enzyme. However, it is difficult to discern what percentage of the enzyme is bound with fatty acid post-purification due to the lack of an optically observed spin-shift with Mn-PPIX. Titration of Fe-Olet with eicosanoic acid does not shift the enzyme fully high-spin, but rather accumulates between 88%-93% high-spin with the remaining portion assumed to be in an inactive state. An explanation of the initial burst phase may be given if the Mn-substituted enzyme behaves similarly to the iron wild-type and the 7%-12% partitioned as “dead enzyme” is still able to react with peracetate.

The second phase for the non-fatty acid bound sample shows a rate that is one order of magnitude slower than the first phase. There is a consistency to the rates, with oxo formation at less than 0.1 s^{-1} with 50-fold excess of peracetate and goes no higher than 0.12 s^{-1} in the presence of 750-fold excess of oxidant. In the presence of a 24,000-fold excess of peracetate, the rate of oxo formation never reaches greater than 1 s^{-1}, possibly due to difficulty for the oxidant navigating fatty acid contaminant to the manganese metal. The ratio of $A_{420/376}$ remains consistent after full accumulation of the oxo intermediate, indicating that this is a stable, weak oxidant that achieves around 55% accumulation. This contrasts with the formation of Compound I in the iron wild-type enzyme since it is already in a state of decay to Compound II within the first millisecond on the Stopped-flow. Due to its reactivity with the fatty acid substrate, the formation rate of Compound II is around 70 s^{-1}, an order of magnitude quicker than with Mn-Olet.

Rates were also measured for samples treated with eicosanoic acid under saturating conditions to determine if peracetate can navigate past the channel blockage created by the fatty acid contaminant. This data also fit to a two-summed exponential with an initial burst-phase and a slow growth phase. The initial phase for the fatty acid treated sample increases to 0.624 s^{-1}, compared to the rate of the non-fatty acid treated sample of 0.0802 s^{-1} (Figure 3.13). The second rate similarly increases for the fatty acid treated sample from .0155 s^{-1} compared to the non-fatty acid treated sample at 0.0013 s^{-1}. While saturation of the enzyme with eicosanoic acid prior to treatment with peracetic acid increases the rate of formation for the high-valent oxo intermediate, the total accumulation is only about 30% compared to a paired reaction without the addition of eicosanoic acid. The ability for the peracetic acid to access the active site appears to be hindered due blockage by the fatty acid contaminant. The oxo intermediate appears to be stable with no apparent decay of the high-valent intermediate. In fact, the second RRT for the fatty acid bound time trace continues to increase slightly after 60 seconds whereas the non-fatty acid treated enzyme has already begun to decay. In is currently unclear why the rates are quicker for the fatty acid bound enzyme since stearic hindrance should decrease the rate for the formation of the intermediate.

Enzyme with no additional fatty acid bound shows an increase in the bleaching of the Soret band at peracetate concentrations greater than 375-fold excess to the enzyme. The effect of porphyrin degradation is slow at lower concentrations, leading to a decay of less than 0.002 s^{-1} when under a 6000-fold excess of peracetate. At 24,000-fold excess of oxidant, the decay rate climbs to 0.008 s^{-1}. The reason for the decay is still unknown, but it is possible that the peracetate is hydrolyzing the porphyrin after the addition of one equivalent of oxidant and renders the enzyme catalytically inert. Since Fe-Olet turns over substrate, there is less concern for inactivation of the enzyme since excess peroxide in solution may be continuously converted to water molecules.

The substitution of iron with manganese leads to a decrease in reactivity for Olet. The stability of this intermediate is persistent regardless of fatty acid presence in the active site of the enzyme, indicating that the Mn(IV) oxidant is not strong enough to abstract a hydrogen atom from a carbon atom that contains a bond dissociation energy of 98 kcal/mol. This also confirms that the formation of the oxo peak is not due to Compound II formation, which was observed by Grant in Fe-Olet, since there is no apparent decay of the intermediate to a low-spin state. Proteins that have been substituted with Mn-PPIX show the ability to epoxidize styrene and to hydroxylate weak carbon bonds. However, there is no evidence for the conversion of styrene to styrene oxide with Mn-Olet and also no data demonstrating reactivity with C-H with lower BDEs, such as phenols and phenol derivatives.

However, the enzyme is capable of abstracting a hydrogen atom from phenol and phenol derivatives. This was determined through the use of a Hammett plot (Figure 3.14), utilizing phenolic derivatives as substrate. The affinity of the enzyme for hydrogen-abstraction from one of these substrates is dependent on the electron donating character of the substrate and the acidity of the high-valent oxo species within the enzyme. The variation of the rate of formation of the oxo species with electron-donating groups suggests rapid hydrogen abstraction, which follows the pattern of the iron-bound porphyrin in the wild-type enzyme and its affinity for nucleophilic attack on fatty acid substrates. The decrease of oxo decay with electron-withdrawing groups suggests that the porphyrin is still tuned to hydrogen abstraction and does not allow for electrophilic attack. The slope of the variation in the reaction rate against the Hammett (σ) constant, which indicates the effects of the molecule's polarity, gives a ρ value of 1.2. The weakness of the slope implies a weak activation of the substrate and its positive value suggests the decay of the high-valent oxo intermediate is mediated by a hydrogen abstraction step and not the formation of a cationic species. The shift in the Soret from 420 nm to 376 nm in the presence of the strongly activating constitutents further implies that the active intermediate is a Mn(IV)-oxo, as the Mn(V)-oxo intermediate would be sufficiently acidic to perform a hydrogen abstraction from weakly-deactivated phenolic derivatives.

3.4 CONCLUSION

Mn-Olet is a useful tool for determining the feasibility of incorporating non-iron PPIX to an overexpressed P450 in liter quantities with the use of ChuA. The reactivity of the enzyme to multiple forms of oxidative species show that the weaker acidity of the manganese needs a stronger oxidant for activation, with peracetate having more success compared to the hydrogen peroxide cofactor used by Fe-Olet. The protein itself, with its ability to achieve a high valent oxo intermediate, is useful for testing the ability of a variety of small molecules to enter the active site of the protein. Based on treatment with different oxidants containing different physical characteristics, Eicosanoic acid typically blocks bulkier small molecules from entering the pocket. When fatty acid substrate does enter the active site, the lack of reactivity and the stability of the high-valent oxo intermediate demonstrate difficulty in cleaving C-H bonds with high BDEs.

3.5 REFERENCES

[1] Yonetani, T., and Asakura, T. (1969) Studies on cytochrome c peroxidase. XV. Comparison of manganese porphyrin-containing cytochrome c peroxidase, horseradish peroxidase, and myoglobin, *J Biol Chem 244*, 4580-4588.

[2] Waterman, M. R., and Yonetani, T. (1970) Studies on modified hemoglobins. I. Properties of hybrid hemoglobins containing manganese protoporphyrin IX, *J Biol Chem 245*, 5847-5852.

[3] Ikeda-Saito, M., Yamamoto, H., Imai, K., Kayne, F. J., and Yonetani, T. (1977) Studies on cobalt myoglobins and hemoglobins. Preparation of isolated chains containing cobaltous protoporphyrin IX and characterization of their equilibrium and kinetic properties of oxygenation and EPR spectra, *J Biol Chem 252*, 620-624.

[4] Lahaye, D., Muthukumaran, K., Hung, C. H., Gryko, D., Reboucas, J. S., Spasojevic, I., Batinic-Haberle, I., and Lindsey, J. S. (2007) Design and synthesis of manganese porphyrins with tailored lipophilicity: investigation of redox properties and superoxide dismutase activity, *Bioorg Med Chem 15*, 7066-7086.

[5] Teale, F. W. (1959) Cleavage of the haem-protein link by acid methylethylketone, *Biochim Biophys Acta 35*, 543.

[6] Balderas, M. A., Nobles, C. L., Honsa, E. S., Alicki, E. R., and Maresso, A. W. (2012) Hal Is a Bacillus anthracis Heme Acquisition Protein, *J Bacteriol 194*, 5513-5521.

[7] de Jong, E. P., Melanson, J. E., and Lucy, C. A. (2004) Noncovalent labeling of myoglobin for capillary electrophoresis with laser-induced fluorescence detection by reconstitution with a fluorescent porphyrin, *Electrophoresis 25*, 3153-3162.

[8] Hill, R. J., Konigsberg, W., Guidotti, G., and Craig, L. C. (1962) The structure of human hemoglobin. I. The separation of the alpha and beta chains and their amino acid composition, *J Biol Chem 237*, 1549-1554.

[9] Winter, M. B., Woodward, J. J., and Marletta, M. A. (2013) An Escherichia coli expression-based approach for porphyrin substitution in heme proteins, *Methods Mol Biol 987*, 95-106.

[10] Gross, U., Sassa, S., Jacob, K., Deybach, J. C., Nordmann, Y., Frank, M., and Doss, M. O. (1998) 5-Aminolevulinic acid dehydratase deficiency porphyria: a twenty-year clinical and biochemical follow-up, *Clin Chem 44*, 1892-1896.

[11] Chen, C., Samuel, T. K., Sinclair, J., Dailey, H. A., and Hamza, I. (2011) An intercellular heme-trafficking protein delivers maternal heme to the embryo during development in C. elegans, *Cell 145*, 720-731.

[12] Li, J. M., Umanoff, H., Proenca, R., Russell, C. S., and Cosloy, S. D. (1988) Cloning of the Escherichia coli K-12 hemB gene, *J Bacteriol 170*, 1021-1025.

[13] Spencer, P., and Jordan, P. M. (1993) Purification and characterization of 5-aminolaevulinic acid dehydratase from Escherichia coli and a study of the reactive thiols at the metal-binding domain, *Biochem J 290 (Pt 1)*, 279-287.

[14] Umanoff, H., Russell, C. S., and Cosloy, S. D. (1988) Availability of porphobilinogen controls appearance of porphobilinogen deaminase activity in Escherichia coli K-12, *J Bacteriol 170*, 4969-4971.

[15] Nagy, G., Dobrindt, U., Kupfer, M., Emody, L., Karch, H., and Hacker, J. (2001) Expression of hemin receptor molecule ChuA is influenced by RfaH in uropathogenic Escherichia coli strain 536, *Infect Immun 69*, 1924-1928.

[16] Torres, A. G., and Payne, S. M. (1997) Haem iron-transport system in enterohaemorrhagic Escherichia coli O157:H7, *Mol Microbiol 23*, 825-833.

[17] Williams, P. H., and Carbonetti, N. H. (1986) Iron, siderophores, and the pursuit of virulence: independence of the aerobactin and enterochelin iron uptake systems in Escherichia coli, *Infect Immun 51*, 942-947.

[18] Torres, A. G., Redford, P., Welch, R. A., and Payne, S. M. (2001) TonB-dependent systems of uropathogenic Escherichia coli: aerobactin and heme transport and TonB are required for virulence in the mouse, *Infect Immun 69*, 6179-6185.

[19] Letoffe, S., Delepelaire, P., and Wandersman, C. (2006) The housekeeping dipeptide permease is the Escherichia coli heme transporter and functions with two optional peptide binding proteins, *P Natl Acad Sci USA 103*, 12891-12896.

[20] Reynolds, E. W., McHenry, M. W., Cannac, F., Gober, J. G., Snow, C. D., and Brustad, E. M. (2016) An Evolved Orthogonal Enzyme/Cofactor Pair, *J Am Chem Soc 138*, 12451-12458.

[21] Sudhamsu, J., Kabir, M., Airola, M. V., Patel, B. A., Yeh, S. R., Rousseau, D. L., and Crane, B. R. (2010) Co-expression of ferrochelatase allows for complete heme incorporation into recombinant proteins produced in E. coli, *Protein Expr Purif 73*, 78-82.

[22] Varnado, C. L., and Goodwin, D. C. (2004) System for the expression of recombinant hemoproteins in Escherichia coli, *Protein Expr Purif 35*, 76-83.

[23] Richard-Fogal, C. L., Frawley, E. R., Feissner, R. E., and Kranz, R. G. (2007) Heme concentration dependence and metalloporphyrin inhibition of the system I and II cytochrome c assembly pathways, *J Bacteriol 189*, 455-463.

[24] Brustad, E. M., and Arnold, F. H. (2011) Optimizing non-natural protein function with directed evolution, *Curr Opin Chem Biol 15*, 201-210.

[25] Grant, J. L., Hsieh, C. H., and Makris, T. M. (2015) Decarboxylation of fatty acids to terminal alkenes by cytochrome P450 compound I, *J Am Chem Soc 137*, 4940-4943.

[26] Rittle, J., and Green, M. T. (2010) Cytochrome P450 compound I: capture, characterization, and C-H bond activation kinetics, *Science 330*, 933-937.

[27] Klinman, J. P. (1994) The Role of Hydrogen Tunneling in Enzyme-Catalyzed Reactions, *Abstr Pap Am Chem S 208*, 8-Biol.

[28] Klinman, J. P. (2000) Tunneling in enzyme catalyzed hydrogen atom transfer reactions., *Abstr Pap Am Chem S 220*, 163.

[29] Matthews, S., Belcher, J. D., Tee, K. L., Girvan, H. M., McLean, K. J., Rigby, S. E. J., Levy, C. W., Leys, D., Parker, D. A., Blankley, R. T., and Munro, A. W. (2017) Catalytic Determinants of Alkene Production by the Cytochrome P450 Peroxygenase OleT(JE), *Journal of Biological Chemistry 292*, 5128-5143.

[30] Grant, J. L., Mitchell, M. E., and Makris, T. M. (2016) Catalytic strategy for carbon-carbon bond scission by the cytochrome P450 OleT, *Proc Natl Acad Sci U S A 113*, 10049-10054.

[31] Borovkov, V. V., Lintuluoto, J. M., and Inoue, Y. (1999) Convenient method for efficient iron and manganese ion insertion into various porphyrins under mild conditions, *Synlett*, 61-62.

[32] Boucher, L. J. (1968) Manganese Porphyrin Complexes .I. Synthesis and Spectroscopy of Manganese(3) Protoporphyrin 9 Dimethyl Ester Halides, *J Am Chem Soc 90*, 6640-&.

[33] Ticebaldwin, K., Fink, G. R., and Arndt, K. T. (1989) Bas1 Has a Myb Motif and Activates His4 Transcription Only in Combination with Bas2, *Science 246*, 931-935.

[34] Martin, J. E., Waters, L. S., Storz, G., and Imlay, J. A. (2015) The Escherichia coli small protein MntS and exporter MntP optimize the intracellular concentration of manganese, *PLoS Genet 11*, e1004977.

[35] White, K. A., and Marletta, M. A. (1992) Nitric-Oxide Synthase Is a Cytochrome-P-450 Type Hemoprotein, *Biochemistry-Us 31*, 6627-6631.

[36] Hsieh, C. H., Huang, X., Amaya, J. A., Rutland, C. D., Keys, C. L., Groves, J. T., Austin, R. N., and Makris, T. M. (2017) The Enigmatic P450 Decarboxylase OleT Is Capable of, but Evolved To Frustrate, Oxygen Rebound Chemistry, *Biochemistry-Us 56*, 3347-3357.

[37] Fleischer, E. B., Chapman, R. D., and Krishnamurthy, M. (1979) Synthesis and Oxidative Demetallation of 2 New Tungsten Porphyrins, *Inorg Chem 18*, 2156-2159.

[38] Morehouse, K. M., and Neta, P. (1984) Kinetics of Demetallation of Manganese(Ii) Porphyrins in Aqueous-Solutions, *J Phys Chem-Us 88*, 3118-3120.

[39] Hambright, P. (1977) Acid Solvolysis Kinetic Study of Manganese(Ii)-Tetra(2-N-Methylpyridyl)Porphine, *J Inorg Nucl Chem 39*, 1102-1103.

[40] Harriman, A., and Porter, G. (1979) Photochemistry of Manganese Porphyrins .1. Characterization of Some Water-Soluble Complexes, *J Chem Soc Farad T 2 75*, 1532-1542.

[41] Batinic-Haberle, I., Reboucas, J. S., and Spasojevic, I. (2010) Superoxide dismutase mimics: chemistry, pharmacology, and therapeutic potential, *Antioxid Redox Signal 13*, 877-918.

[42] Nick, R. J., Ray, G. B., Fish, K. M., Spiro, T. G., and Groves, J. T. (1991) Evidence for a Weak Mn=O Bond and a Nonporphyrin Radical in Manganese-Substituted Horseradish-Peroxidase Compound-I, *Journal of the American Chemical Society 113*, 1838-1840.

[43] Lelyveld, V. S., Brustad, E., Arnold, F. H., and Jasanoff, A. (2011) Metal-substituted protein MRI contrast agents engineered for enhanced relaxivity and ligand sensitivity, *J Am Chem Soc 133*, 649-651.

[44] Gelb, M. H., Toscano, W. A., Jr., and Sligar, S. G. (1982) Chemical mechanisms for cytochrome P-450 oxidation: spectral and catalytic properties of a manganese-substituted protein, *Proc Natl Acad Sci U S A 79*, 5758-5762.

[45] Cai, Y. B., Yao, S. Y., Hu, M., Liu, X. Y., and Zhang, J. L. (2016) Manganese protoporphyrin IX reconstituted myoglobin capable of epoxidation of the C=C bond with Oxone (R), *Inorg Chem Front 3*, 1236-1244.

[46] Day, V. W., Stults, B. R., Tasset, E. L., Marianelli, R. S., and Boucher, L. J. (1975) Stereochemistry of 5-Coordinate and 6-Coordinate High-Spin Manganese(Iii) Porphyrins and Their Structural Analogues, *Inorg Nucl Chem Lett 11*, 505-509.

[47] Luther, G. W. (2005) Manganese(II) oxidation and Mn(IV) reduction in the environment - Two one-electron transfer steps versus a single two-electron step, *Geomicrobiol J 22*, 195-203.

[48] Vickery, L., Nozawa, T., and Sauer, K. (1976) Magnetic Circular-Dichroism Studies of Myoglobin Complexes - Correlations with Heme Spin State and Axial Ligation, *j Am Chem Soc 98*, 343-350.

[49] Roux, Y., Ricoux, R., Avenier, F., and Mahy, J. P. (2015) Bio-inspired electron-delivering system for reductive activation of dioxygen at metal centres towards artificial flavoenzymes, *Nat Commun 6*, 8509.

Figures and Tables

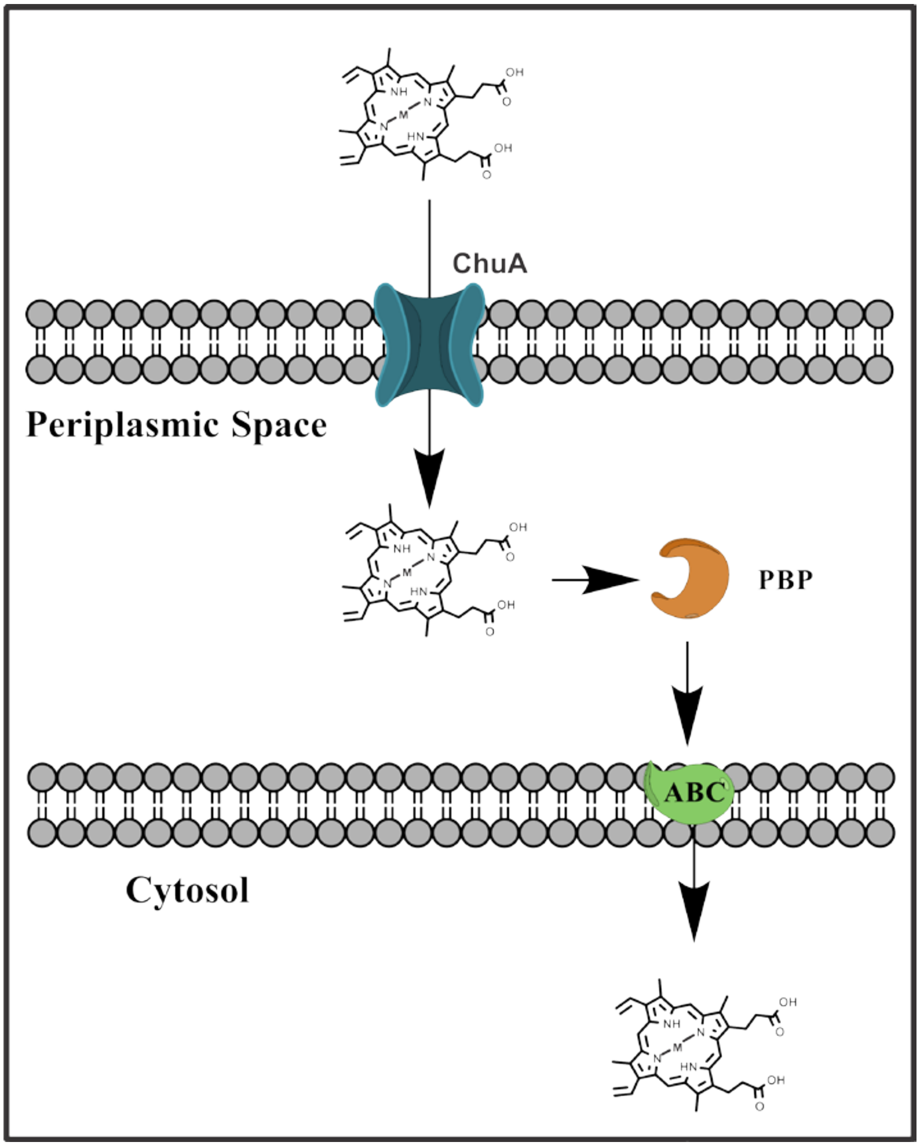

Figure 3.1: Diagram of non-native porphyrin incorporation into the cell with ChuA. “M” is any metal capable of seating correctly in Protoporphyrin IX. ChuA is the importer protein, PBP is the periplasmic binding protein, and ABC is the ATP-dependent binding cassette.

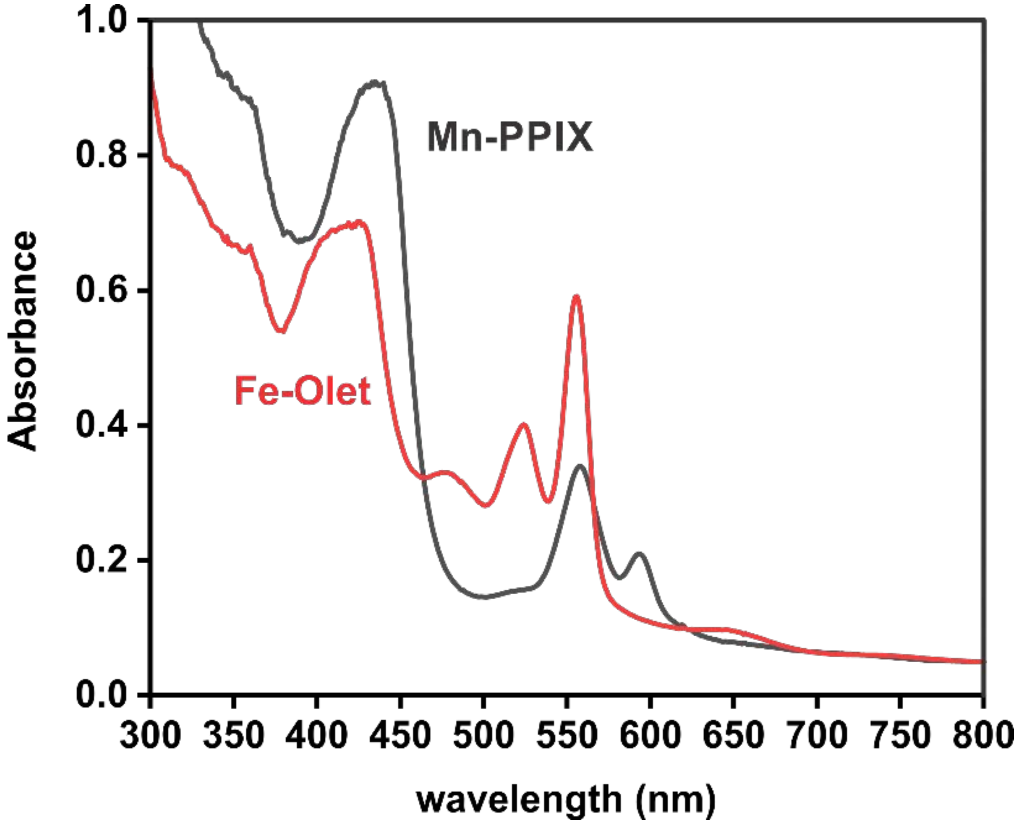

Figure 3.2: Pyridine hemochromagen assay for Mn-Olet and Fe-Olet. Assay conducted with 10 µM of either Fe-Olet or Mn-Olet. For both comparison and validation that the enzyme is iron-free, 8 µM Fe-Olet was used as a control. The lack of an overlap at the α-band for the Mn-Olet confirms undetectable amounts of iron in the protein (< 95%).

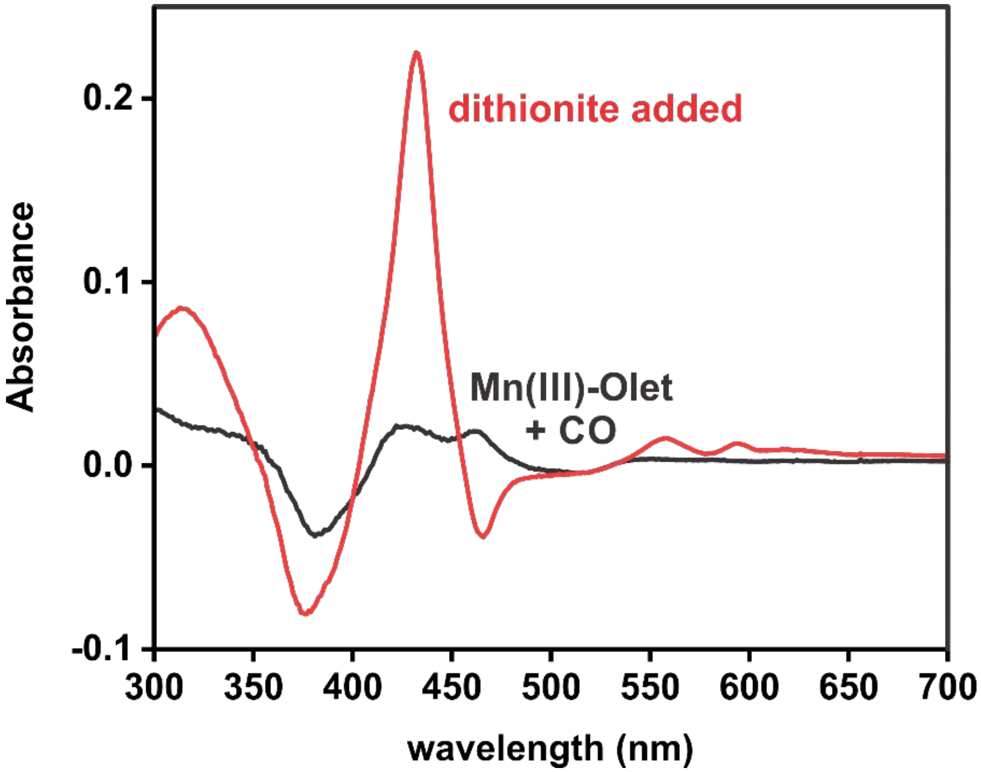

Figure 3.3: CO difference spectrum for Mn-Olet. Assay conducted with 4 µM reduced Mn-Olet. The black trace is anaerobic Mn(III)-Olet incubated with carbon monoxide. The red trace is upon the addition of excess sodium dithionite solution. There is no obvious peak formed at 450 nm, suggesting the lack of Fe-Olet present in the solution.

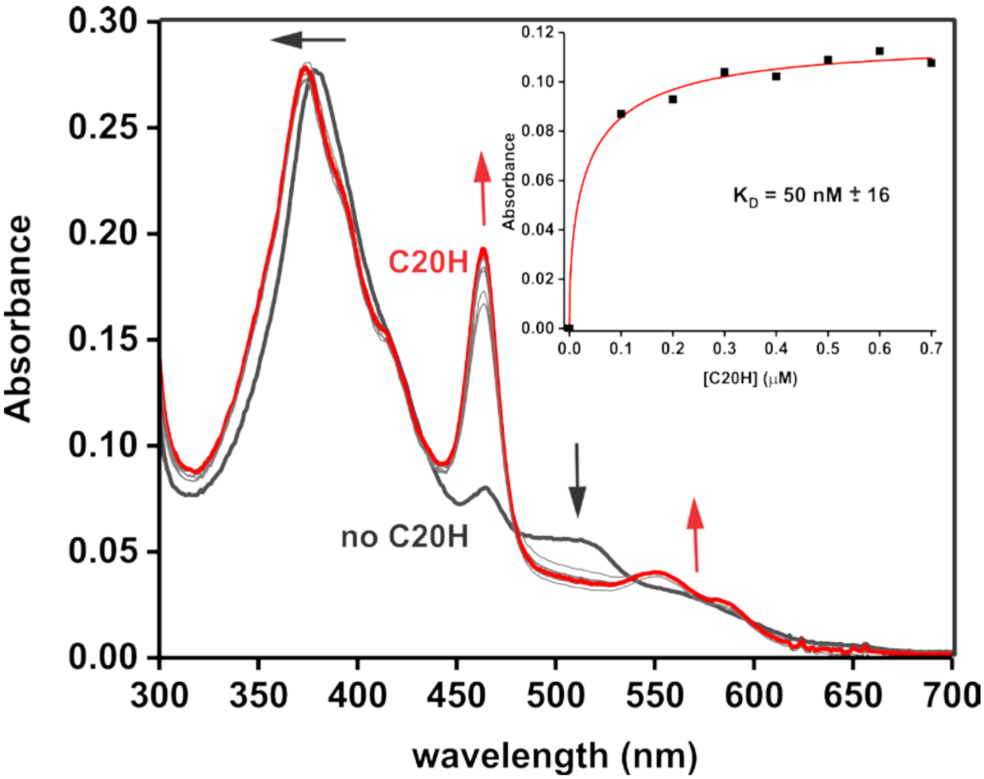

Figure 3.4: Determination of K_D using the optical changes at 463 nm for Mn-Olet. The dissociation constant was determined with 4 μM Mn-Olet and eicosanoic (C20:0) fatty acid in triplicate. The K_D is similar to one obtained for Fe-Olet, which is 110 nM (Chapter 4).

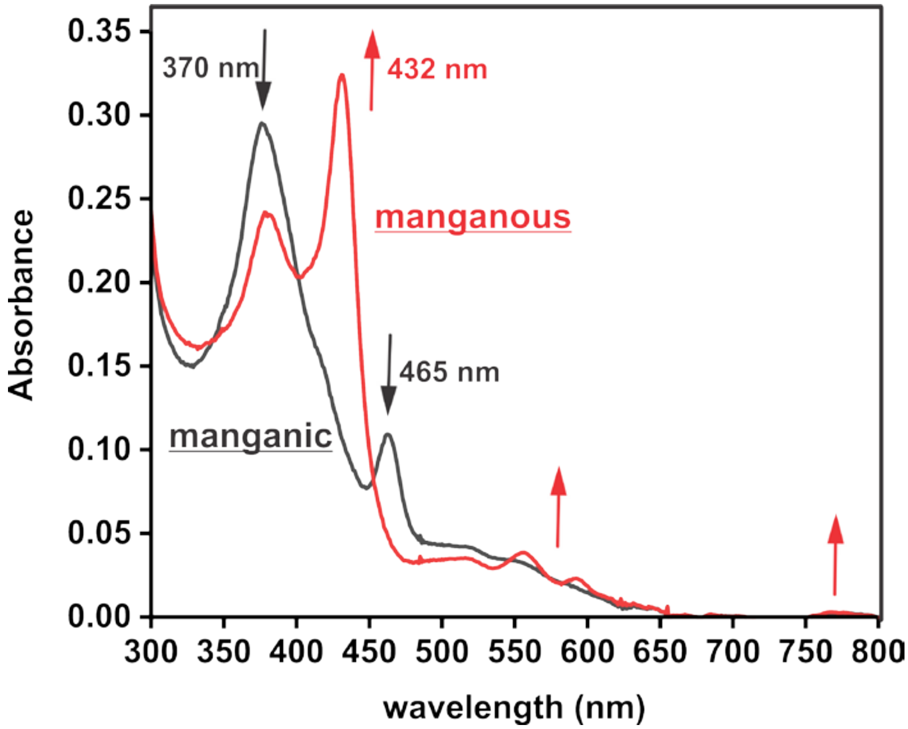

Figure 3.5: Optical characterization of Mn-Olet. 4 µM Mn(III)-Olet (in black) is reduced with excess sodium dithionite in an anaerobic environment to form Mn(II)-Olet (in red).

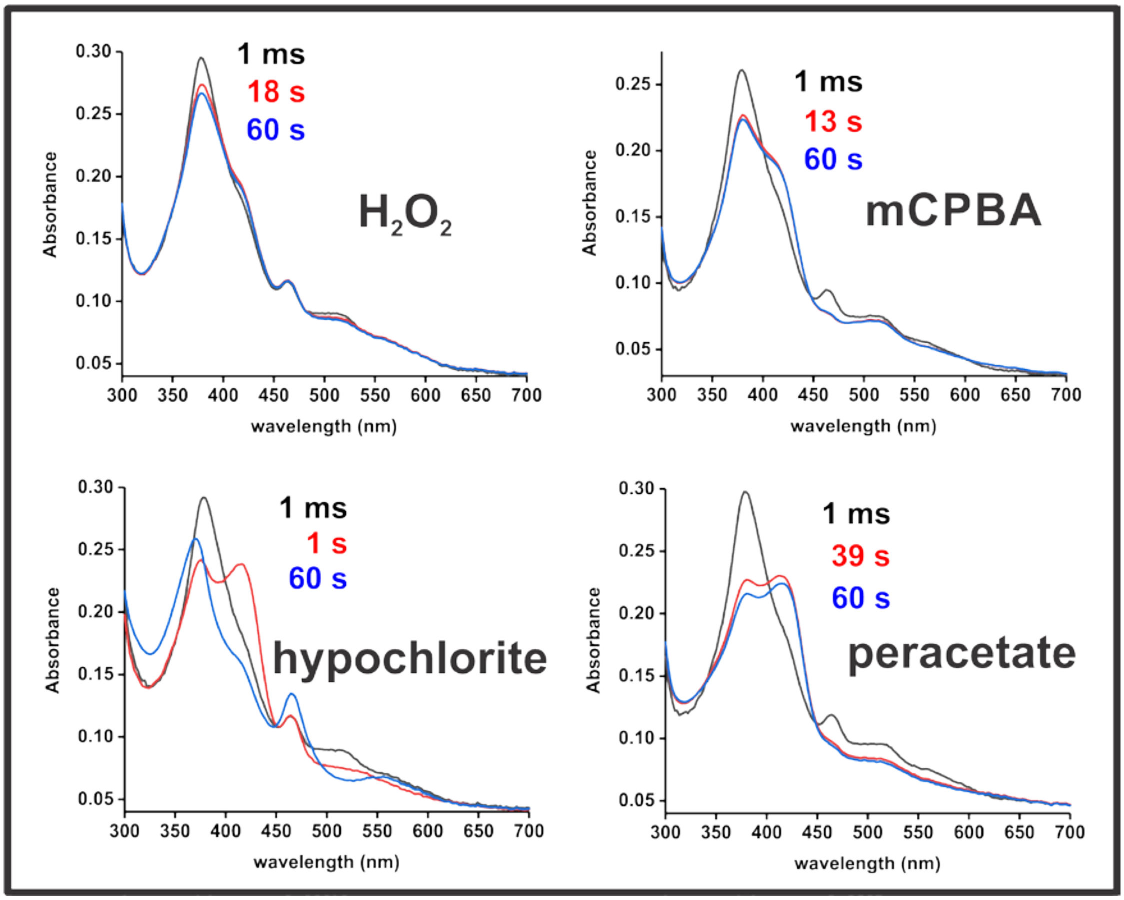

Figure 3.6: High-valent oxo species formed by Mn-Olet utilizing different oxidants. For all traces, 10 µM of Mn(III)-Olet were reacted against differing oxidants, whose concentrations were dependent on protein stability. 5 mM hydrogen peroxide reacts, but does not achieve high accumulation. 0.16 mM mCPBA yields a small, but stable accumulation of the intermediate species. 3.2 mM sodium hypochlorite reacts to briefly form high accumulation of intermediate, but subsequently decays to a form of the enzyme where the thiolate ligand is removed from the Mn-PPIX. 5.2 mM peracetic acid forms and maintains high a high accumulation of high-valent oxo complex with minor bleaching dependent on the peracetate concentration. The lack of formation for hydrogen peroxide indicates that the peracetate is the active reagent in this reaction.

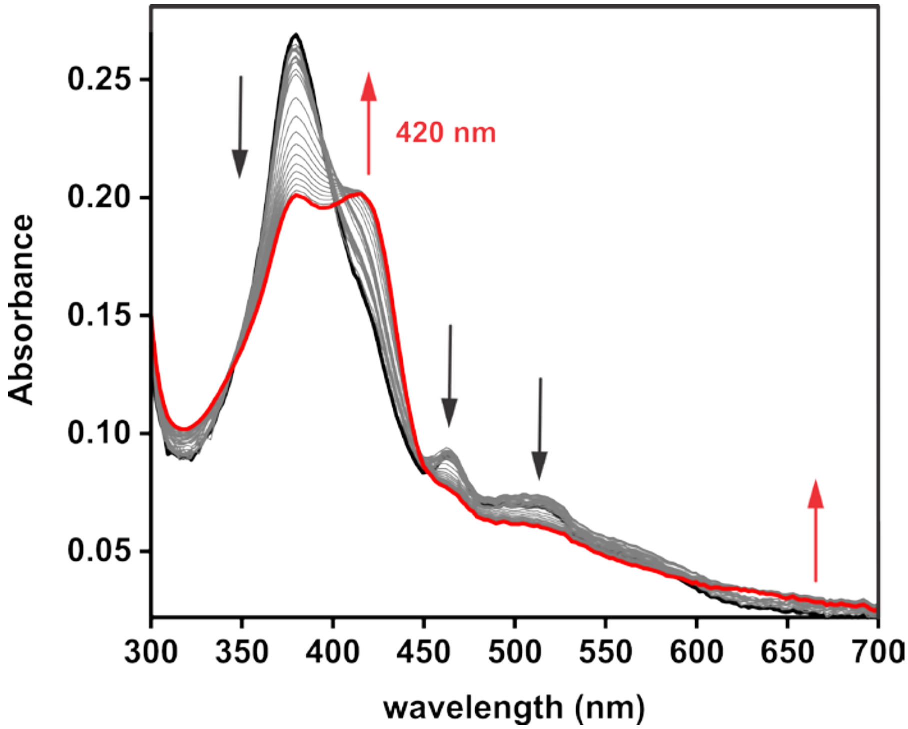

Figure 3.7: Stopped-flow spectra of high-valent oxo formation in Mn-Olet. This details the first 39 seconds of the peracetate panel in Figure 3.6 at 4^{o}C. Final concentrations after mixing are 8 µM manganese OleT and 1.5 mM peracetic acid.

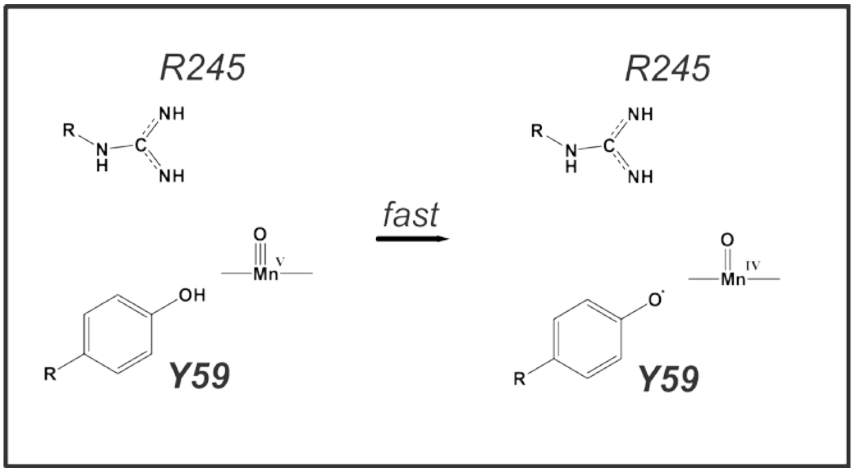

Figure 3.8: Proposed reduction pathway from the Mn(V)=O to Mn(IV)=O.

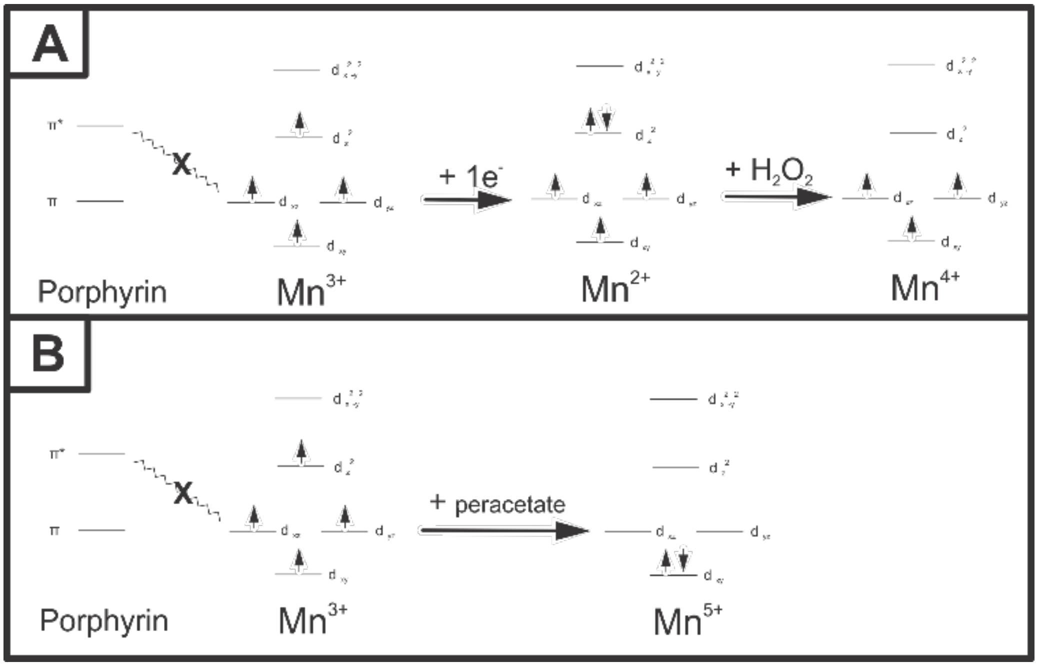

Figure 3.9: Molecular orbitals for proposed oxidation state transitions for Mn-Olet upon addition of oxidants. A) The pathway for the formation of the Mn(IV) oxo species beginning with the manganous form of the enzyme and the addition of hydrogen peroxide. B) The pathway for the formation of the Mn(V) oxo species with the addition of peracetate to the manganic form of the enzyme.

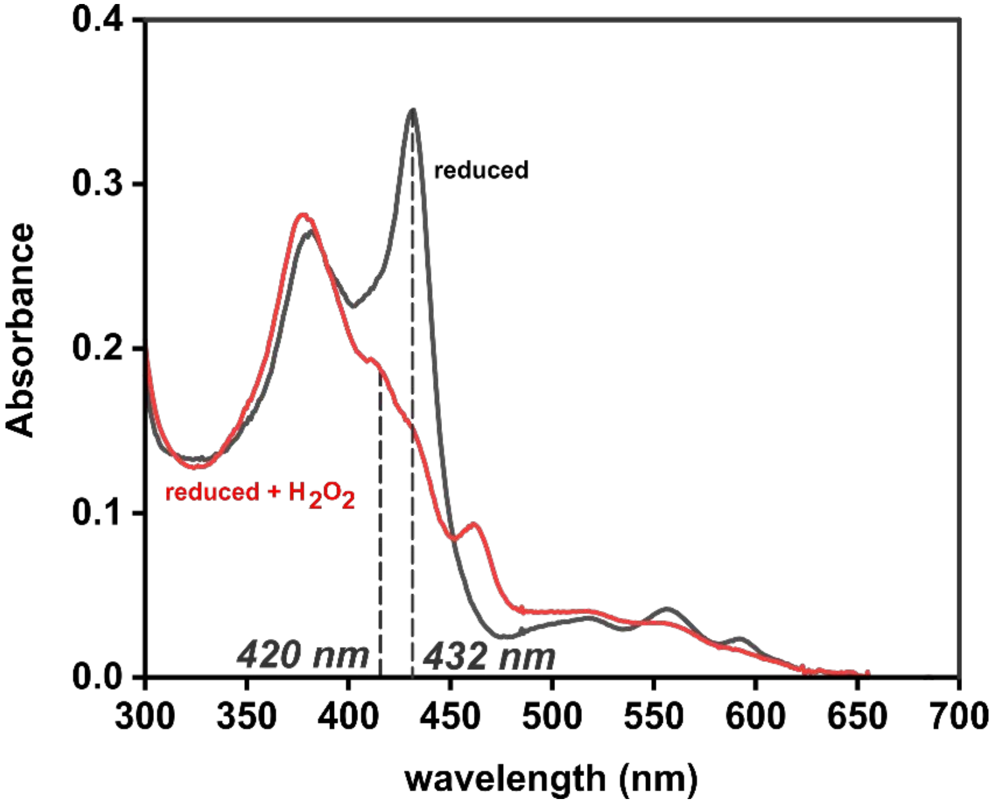

Figure 3.10: Optical spectra of Mn(IV)=O formation with reduced Mn-Olet and hydrogen peroxide. 4 µM Mn-Olet (as-purified) is reduced with 1.5 molar equivalents of sodium dithionite in an anaerobic environment. After full reduction, 50 µM hydrogen peroxide was added to the cuvette and mixed. Spectra were taken until the enzyme oxidized back to its manganic state. The peak at 420 nm is likely a high-valent oxo intermediate forming prior to its decay to an Mn(III) state.

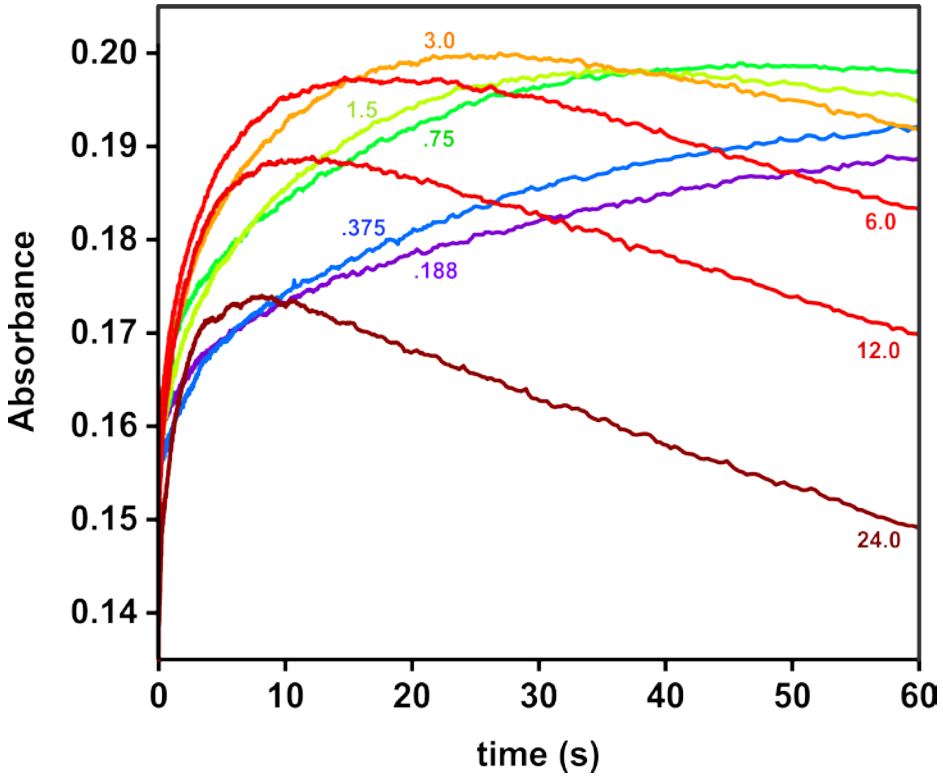

Figure 3.11: Time traces of differing concentrations of peracetate mixed with Mn-Olet. Measurements were taken by Stopped-flow at 4^{o}C with 8 µM Mn(III)-Olet rapidly mixed with peracetate and observed for the formation of the oxo intermediate at 420 nm. The decay phase constitutes the bleaching of the porphyrin absorbance, and not a decay to the Mn(III) form of the enzyme.

Table 3.1: Rates of Mn(IV)-oxo formation reacted with differing concentrations of peracetic acid.

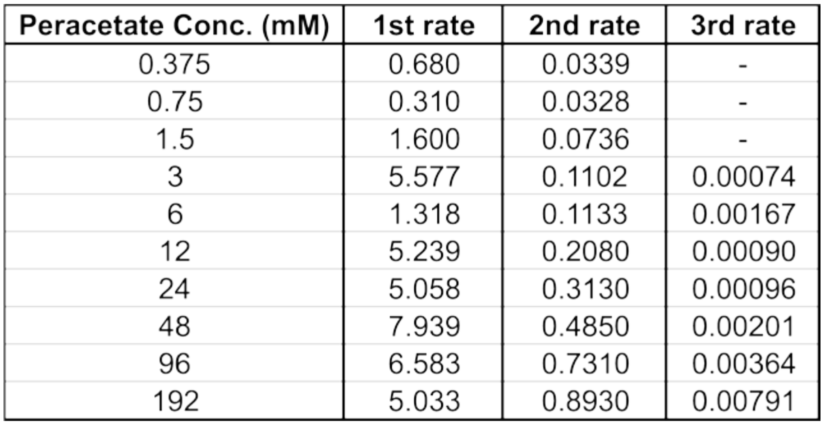

Peracetate Conc. (mM)	1st rate	2nd rate	3rd rate
0.375	0.680	0.0339	-
0.75	0.310	0.0328	-
1.5	1.600	0.0736	-
3	5.577	0.1102	0.00074
6	1.318	0.1133	0.00167
12	5.239	0.2080	0.00090
24	5.058	0.3130	0.00096
48	7.939	0.4850	0.00201
96	6.583	0.7310	0.00364
192	5.033	0.8930	0.00791

A quick burst phase is present in each trace, represented by the first rate. This is either followed by or coincides with the slow accumulation of the oxo species to its maximum concentration, represented by the second rate. The third rate exerts itself at high concentrations of peracetic acid and is representative of the bleaching of the porphyrin absorbance, not the regression of the high-valent oxo intermediate back to the manganic form of the enzyme.

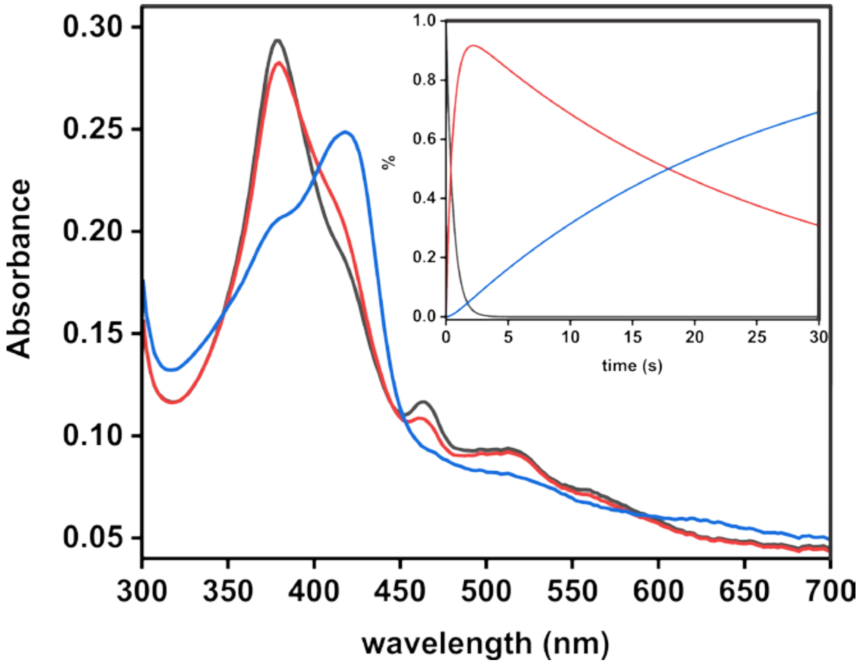

Figure 3.12: SVD spectra of the proposed pure Mn(IV)=O species with the speciation plot. These spectra were extracted from the two growth phases occurring during the first 30 seconds of the reaction of 8 µM Mn-Olet with 1.5 mM peracetate. The black trace is the manganic form of the enzyme, the red trace is the fast growth rate of the reaction, and the blue trace is the slow growth rate of the reaction. The inset shows the concentration of each state as a function of time.

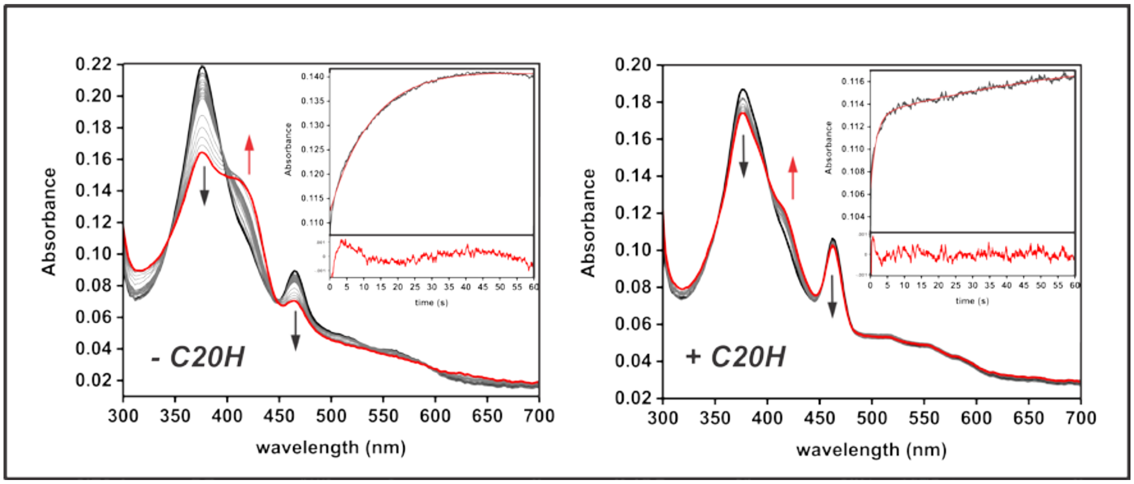

Figure 3.13: Stopped-flow spectra of Mn(IV)=O formation of Mn-Olet with (right) and without (left) eicosanoic acid. 2 µM Mn-Olet treated with 70 µM peracetic acid post-mix on the Stopped-flow at 4^{o}C. Treatment with C20 fatty acid inhibits entry of the peracetate into the active site of the enzyme, allowing for a smaller accumulation of the high-valent oxo intermediate. The first oxo formation rate without additional fatty acid is 0.0802 s^{-1} and a second rate of 0.0013 s^{-1}, while the first rate with additional fatty acid is 0.624 s^{-1} and a second rate 0.0155 s^{-1}

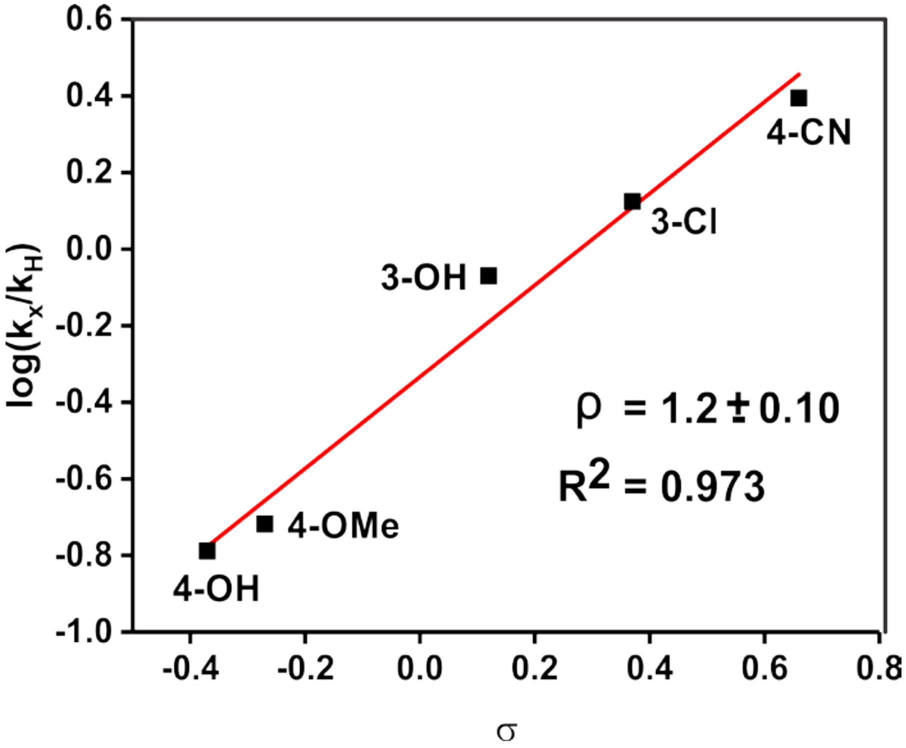

Figure 3.14: Hammett plot for Mn-Olet with phenol derivatives. The plot was prepared from measuring the rate of oxo formation at 420 nm for each derivative followed by normalization with phenol. The log of this normalized factor is then plotted against the known Hammett coefficient (sigma) for each derivative. The formation rates were measured by stopped-flow at 4^{o}C by rapidly mixing 5 mM peracetic acid with 8 µM Mn-Olet incubated with 1 mM of phenolic derivative.

CHAPTER 4

RE-TUNING THE REACTIVITY OF THE FERRYL-OXO INTERMEDIATES IN P450OLET THROUGH SUBSTITUTION WITH IRON-MESOPORPHYRIN IX

4.1 INTRODUCTION

Alteration of the redox potential of an enzyme is a technique often used to study its change in catalytic behavior and develop a catalyst that promotes the production of a highly desired product that is not normally produced by the native enzyme. Traditional techniques involve one of two methods. The first method relies on the identification and mutagenesis of residues providing the first or second shell interaction with the catalytic metal while the second method requires the denaturation and removal of the native metal porphyrin and incorporation of the desired one. However, these studies rarely involve thiolate-ligated P450s that perform decarboxylase-specific chemistries. Both of these methods have potential difficulties, since mutagenesis requires alteration of the environment surrounding the sole endogenous ligand to the metal and the incorporation of a non-native porphyrin finishes with low yields due to the harshly acidic conditions involved with denaturation and removal of the thiolate-ligated porphyrin.

More modern methods that have been successfully used for the incorporation of non-native porphyrins through the use of knockout mutations involved in porphyrin biosynthesis in the RP523 cell line [1-3]. Unfortunately, these require stringent growth conditions involving minimal media in an anaerobic environment, as to disfavor the formation of radical oxygen species [4, 5]. A softer approach is the use of the bacterial heme importer ChuA for the acceptance of a non-native porphyrin [6]. Previously, it had been used to transport Mn, Fe, Co, and Zn PPIX cofactors into E. coli for incorporation into P450 BM3 (CYP102A1) with full incorporation of the added porphyrin [7]. The use of this system with hemin has also been reported to result in higher protein expression levels compared to the reliance on native porphyrin synthesis in E. *coli* [8].

Myoglobin was among the first porphyrin-based proteins to be studied in terms of studying the alteration of the redox potential. Mutations of the second coordination sphere have been successfully incorporated into the protein scaffold. Mutagenesis of the S92 residue involved in the second coordination sphere for the proximal ligand of the F33Y mutant of myoglobin increases the potential by 28 mV [9]. Two distinctive changes to the porphyrin itself may also be used, with the addition/reduction of carbons in the porphyrin and the alteration of the porphyrin's prosthetic groups. Alteration from vinyl groups to those with electron withdrawing character, such as formyl groups, will decrease the affinity of oxygen towards myoglobin due to the loss of π-electrons [10]. Alteration of the ring itself through the addition of more carbons without breaking aromaticity, as with hemiporphycene, will increase the potential and as well as the affinity for oxygen and oxygen-like substrates [11, 12]. Alteration this sort will allow myoglobin to activate O_2 and perform hydroxylation chemistries and epoxidation on weak carbon bonds.

Similar experiments involving the alteration of the reduction potentials in cytochromes have also led to similar results. Mutation of the histidine ligand to a methionine in the electron carrier cytochrome c3 increases the redox potential by up to 200 mV [13], a trend comparable to same mutation in cytochrome c increasing the potential by 230 mV [14]. The shortening of the Fe-S bond length decreases the potential of the protein, while its elongation provides an increase in the potential [15]. Bovine cytochrome b5, which functions as an electron carrier to membrane-bound oxygenase enzymes, decreases the potential of the enzyme by 83 mV when replaced with 2,4 dimethyldeuteroporphyrin [16]. Model systems mimicking myoglobin and cytochrome active sites have been used to calculate equivalent redox potentials of various iron-porphyrins. Fe-PPIX has a redox potential of -115 mV and Fe-Mesoporphyrin IX (Fe-MPIX) has a redox potential of -158 mV, due to the lack of donating character through the transformation of the 2,4 vinyl groups to alkyl groups [15].

Experiments involving the incorporation of non-native porphyrins into enzymes with thiolate ligands have been performed to study the effect of substrate interaction with an enzyme as a function of redox potential. Nitric Oxide Synthase (NOS) demonstrates a decrease in the redox potential by around 50 mV and an increased rate of peroxide activation when PPIX is substituted with MPIX [17]. Furthermore, Woodward attributed this to the concentration of the electrons within the porphyrin ring, leading to a “push” effect to dissociate the distal oxygen of the bound H_2O_2 and the subsequent stabilization of the Compound I intermediate and a decrease in the rate of product formation.

Porphyrin biosynthetic pathways within the cell are specific for the type of metal that is to be incorporated into a given porphyrin. However, misincorporation of the metal *in vivo* do occur and may also contribute to an improperly installed porphyrin. There are occurrences when this effect has a negative impact on the survivability of the cell, as is the case with an non-catalytically active metal such as zinc or copper is incorporated into PPIX [18]. Incorporation of these unreactive porphyrins will significantly reduce the oxygen carrier’s, such as hemoglobin and myoglobin, activity or render them inert [19]. However, this also provides a useful mechanism to counteract excess metals within the cytosol by incorporating them in an inert form [20]. However, not all porphyrins may be utilized as a replacement for hemin. Incubation of apocytochrome c with iron-deuteroporphyrin (DPIX) does not yield a holoprotein, but the apoprotein does reconstitute into its *holo* form after incubation with Fe-PPIX [21].

P450olet performs decarboxylation upon its substrate [22] rather than the hydroxyl radical rebound mechanism prevalent among P450 monooxygenases [23-25]. The acid-alcohol pair present in CYP101A1 [26] is replaced with an arginine-proline pair which forms a salt bridge to the carboxylate of the fatty acid [27] and, as observed on the C20H-bound crystal structure, inhibits the tail of the fatty acid from accessing a cavity present between the carboxylate residues of the porphyrin (PDB ID: 4L40). Hydrogen peroxide binds to the ferric heme by taking advantage of the “peroxide-shunt” mechanism usually present as a release mechanism in canonical P450 oxygen activation [28]. This allows two electron equivalents to be incorporated by the oxygen species in lieu of two rounds of one electron transfers with a ferredoxin. This makes the enzyme ideal for study *in vitro* since all accumulated spectra carry no interference from iron-sulfur or flavin contaminant signals. The binding of hydrogen peroxide is followed by the removal of the proximal proton to give a ferric-hydroperoxo intermediate, although the specifics of this portion of the mechanism is presumably not elucidated with respect to P450olet due to its high reactivity [29].

The proton rebounds to the distal oxygen of the peroxide to form water and subsequently pushed off, forming a ferryl-oxo π-cation intermediate known as Compound I (Cpd. I), which is the first biologically observed species obtained through its native mechanism [30]. The life-span of this intermediate is notable since it is rarely observed in the presence of the enzyme’s native substrate, usually being isolated from a reaction between low-spin, ferric enzyme and an activated peroxo-species such as mCPBA or peracetic acid [31]. The rate of Cpd. I decay is consistent with differing chain lengths, as it is always observed abstracting a hydrogen atom from the β-position of the fatty acid. Although the decay rate is similar, the accumulation of intermediate decreases with decreasing fatty acid chain lengths-probably due to a decreased quantity of starting high-spin enzyme. As Cpd. I decays, the ferryl-hydroxo intermediate known as Compound

II (Cpd. II) forms. The lifetime of Cpd. II was verified through the use of the radical clock norcarane [30], which confirm its stabilization in the range of milliseconds, rather than on the level of picoseconds as is the case for canonical P450 hydroxylases [32]. QM/MM studies link the stability of Cpd. II to hydrogen bonding networks that raise the activation barrier gating the rebound of the hydroxyl radical back to the substrate, but it does allow for the extraction of a second electron from the substrate [33]. The exact nature of this stability still unknown, as there are no studies confirming the method of decay of Cpd. II and no structures firmly dictating the presence of stabilizing forces.

The mechanistic steps involved with the decay of Cpd. II back to the ferric, low-spin form are still debated with two different mechanisms proposed. The missing step involving rebound of the hydroxyl radical implies that a second electron must be removed from the substrate in order to maintain a stoichiometric number of electrons for the formation of an alkene and carbon dioxide. However, the origin of this second electron is unknown, as it may be located on the oxygen of the carboxylate, as proposed by Belcher [27] and verified on other alkene-producing P450s [34, 35]. This mechanism relies on a radical rearrangement involving heterolytic cleavage between the carboxylate carbon and Cα, with one electron to the carboxylate to form carbon dioxide and the other to joining with the radical on Cβ to form a Cα=Cβ bond. The alternative mechanism involves extraction of the second electron from the β-carbon radical, leaving a cation intermediate [36]. The electron pair on the carboxylate anion would form a π-bond with the carbon and homolytically cleave the bond between the carboxylate carbon and the Cα, forming a Cα=Cβ bond.

Upon metabolism of C10-C16 fatty acids by P450olet, the formation of hydroxylated fatty acids as minor products becomes apparent [30]. The exact reason for this is unknown, but it is likely that residues holding the ω-carbon in place no longer have an effect, leading to more mobility for the fatty acid within the enzyme's active site. Although the amount of hydroxylated product increases as fatty acid chain length decreases, the ratio of products remains constant in the order of decreasing accumulation: alkene, β-OH, γ-OH, and α-OH fatty acid [37]. This suggests limits to the freedom for these shorter fatty acids within the active site due to the presence of other residues responsible for stabilizing the fatty acid that hydroxylation beyond Cγ.

Other peroxidase enzymes related to P450olet are known to metabolize fatty acid substrates, notably the hydroxylation reaction of P450 BSβ [38, 39] and P450SPα [40] and the decarboxylation chemistry of P450staph (not published). However, no studies have been performed to test the effect altering the redox potential will have on the product distribution for these enzymes. Ideally, the enzyme would alter its current product count leading to a higher distribution of alkene production for use as drop-in biofuels or the creation of new functional groups easily for use in polymer chemistry, such as epoxides, would be essential for the manufacture of polymers [41]. The change in the potential observed through modification of the porphyrin is driven by the change in electron density of the ring and allows the formation of products that may be utilized in fields other than biofuels. Changing the metal from iron to manganese in PPIX raises the redox potential, as mentioned in Chapter 3, leading to creation of epoxides with certain molecules, such as the conversion of styrene to styrene oxide. On the other hand, the reduction of the 2,4 vinyl groups in PPIX -creating MPIX- leads to a decrease of the potential and provides a baseline in P450olet for products catalyzed by a porphyrin with stronger affinity for oxygen adducts. Although this may not be noticeable with fatty acids greater than C18 due to their inherent stability within the pocket, the variation in products would be indicative of whether it is more prudent to decrease or increase the potential of the porphyrin to alter the current balance of hydroxylated product. In addition, the ability to discern information concerning the intermediate steps of the reaction would also be useful, especially given how the portion of the mechanism extending from Cpd II decay to Ferric, low-spin has not been elucidated.

The redox potential of native P450olet is unusually positive, lying around -100 mV in both the Ferric, low-spin and Ferric, high-spin states [27]. This is peculiar since the low-spin redox potential for canonical P450s is below -300 mV, as with CYP101A1 [42] and P450cin (CYP176A1) [43], and prevents the transfer of the first electron by their associated ferredoxin rather than position itself where a redox partner is able to transfer electrons to the enzyme [44].   Of interest are the effects of altering the potential of the enzyme through non-native porphyrins and two porphyrins were chosen. Fe-Mesoporphyrin IX (Fe-MPIX) lowers the potential by about 50 mV and into the range of the redox potential for ferric, high-spin CYP101A1 (Figure 4.1). 2,4-diformyldeuteroporphyrin IX (Fe-dfDPIX) raises the potential by about 70 mV, far outside the redox potential of known P450s. Unfortunately, dfDPIX could not be incorporated due to hydrophobic residues surrounding the 4-position of the porphyrin and stearically hinders polar groups from seating correctly, as determined by the crystal structure referenced earlier. This led to attempts at incorporation of stronger electron withdrawing group being unsuccessful, leading to a single alteration of the redox potential for the purposes of this study.

4.2 MATERIALS AND METHODS

Expression of MP_{Olet}

The plasmid containing the P450olet Y110C mutant [45], cloned into a pET283 vector with a T7 promoter and C-terminal 6x polyhistidine tag, was co-transformed with the vector pChuA (purchased from Addgene [plasmid #42539], deposited by Alan Jasanoff) containing the gene for the expression of the porphyrin importer ChuA into chemically-competent BL21 (Dε3) cells previously transformed with the pLysS plasmid which reduces cellular background signal. A single colony was transferred to an overnight culture and incubated for 12-16 hours. From this starter culture, 10 mL of inoculant were added to each liter of M9 minimal media, which consists of the following: 12.8 g sodium phosphate, dibasic, 3 g sodium phosphate, monobasic, 0.5 g sodium chloride, 1 g ammonium chloride, 0.5% glycerol, 2 mM magnesium sulfate, 0.1 mM calcium chloride, 0.1% casamino acids, 0.05 g kanamycin, 0.1 g ampicillin, and 0.02 g chloramphenicol. The culture grew at 37^oC, 210 rpm until it reached an OD_{600}=0.5. Upon reaching this OD, the temperature was dropped to 20^oC and incubated for an additional 20 minutes, when 10 mg of Fe-MPIX (dissolved in DMSO) were added to each flask. The culture incubated for an additional 10 minutes prior to induction with 50 µM IPTG and grown for 30 hours followed by centrifugation for 15 minutes at 16000 rpm and freezing the pellet at -80ºC.

Purification of MPolet

The pellet was resuspended in 50 mM potassium phosphate, dibasic, pH=7.5, 300 mM sodium chloride, 10 mM imidazole (Buffer A) and sonicated at 2 minute cycles seven times with 5 minute breaks between cycles where the solution was stirred on ice. The lysate was cleared by centrifuging at 16000 rpm for 45 minutes and the supernatant was loaded onto a 25 mL Ni-NTA column that had been pre-equilibrated with Buffer A. The column was subsequently washed with Buffer A + 10 mM imidazole and the protein eluted with Buffer A + 240 mM imidazole. The eluent was diluted with one equivalent of 55% ammonium sulfate solution in 100 mM potassium phosphate, dibasic and cleared by centrifuging at 4400 rpm for 10 minutes to remove unwanted precipitant. The supernatant was loaded onto a butylsepharose column pre-equilibrated with 30% ammonium sulfate and washed with the same buffer. The protein was eluted with a gradient from 30%-0% ammonium sulfate for 200 mL and 5 mL fractions collected. The fractions containing $A_{412/280}$ > 0.9 were pooled and precipitated with by adjusting the concentration to 60% ammonium sulfate and centrifuged as above. The precipitated protein was resuspended in a minimal volume of 200 mM potassium phosphate, dibasic, pH=7.5 and dialyzed twice in 2 L of buffer. A 12% SDS-

PAGE gel confirmed the purity of the enzymes prior to their experimentation (Figure 4.2). The purified protein was flash-frozen and stored at -80ºC.

UV-Vis

All UV-Vis spectra were taken with an Agilent 8453 UV-Vis Spectrophotometer and analyzed on their proprietary data collection software and with the Origin software package. The spin-state spectra were determined by taking 5 μM protein and adding one equivalent of hydrogen peroxide, shifting any high-spin protein to a low-spin form. Four molar equivalents of eicosanoic acid were subsequently added and incubated for one hour on ice, centrifuged at 14000 rpm for 10 minutes, and the spectrum taken for the fully high-spin spectrum. Two molar equivalents of hydrogen peroxide were mixed with the fully high-spin protein to ensure that it was still fully active. The CO spectrum was taken by degassing 5 μM protein in an anaerobic cuvette in the presence of 0.1 molar equivalents of methyl viologen. CO was bubbled into the cuvette for 5 minutes and the initial spectrum was taken. 3-6 molar equivalents of degassed sodium dithionite solution were added to the cuvette, mixed, and the spectrum immediately taken.

The dissociation constant (K_D) was measured in triplicate by taking aliquots of 4 μM protein and adding 1 molar equivalent of hydrogen peroxide to each tube, ensuring the spectrum is in a fully low-spin state prior to the start of the titration. Eicosanoic acid (dissolved in 30% Triton-X/70% ethanol) was added in 0.5 μM increments. The solutions incubated at 4ºC overnight and centrifuged for 5 minutes at 14000 rpm. Spectra were taken for all tubes, averaged, and the

K_D was calculated with the Morrison equation, a derivative of the Michaelis-Menten equation for use on data that contains a dissociation constants tighter than several micromolar.

Pyridine Hemochromagen assay

To determine the percentage of MPolet to PPolet, the pyridine hemochromagen assay was used to detect the separation of band distinct for both MPIX and PPIX. This protocol is a modification of a published protocol by Barr [46]. Briefly, one equivalent of a 40% pyridine/200 mM sodium hydroxide solution was mixed with 6 µM MPolet and an oxidized spectrum taken on the UV-Vis. To obtain the reduced species, several grains of sodium dithionite were mixed into the sample. This was repeated for PPIX as an additional reference and also to discern differences between Fe-PPIX and PPolet. Impurities were visually determined based on the absorbance of the α-band in the Q-region of the spectra.

Stopped-flow measurements

The Stopped-flow observes the presence of enzymatic intermediates and calculates the rates for any observable intermediates. All data were collected on an Applied Photophysics Stopped-flow instrument using either a photodiode array for full spectral collection or a photomultiplier tube for a single, high resolution wavelength. Specific wavelengths observed were at 357 nm (Compound I Soret), 410 nm (ferric, low-spin), 430 nm (Compound II), and 680 nm (Compound I π-cation radical). Unless otherwise stated, spectra were collected under aerobic conditions at 4°C. All data were analyzed with the Pro-

Data SX software program from Applied Photophysics and the Origin software package.

To determine the rate of decay for Compound I, rate of formation for Compound II, and the decay of Compound II, Syringe A was loaded with 10 µM MP_{Olet} incubated with a 4 molar excess of proteated or deuterated fatty acid (C20, C16, or C12) and spun down for 10 minutes at 4400 rpm. Syringe B was loaded with 10 mM hydrogen peroxide. Data were collected with one second, logarithmic shots.

In order to determine the rate for peroxide association and dissociation constants, 10 µM enzyme was treated with deuterated or proteated eicosanoic acid as above and loaded into Syringe A. Syringe B contained hydrogen peroxide ranging from 80 µM to 10 mM. The data was plotted as a function of k vs peroxide concentration, with the y-intercept indicating the K_D of peroxide and the slope identifying the peroxide association with the enzyme.

An Arrhenius dependence plot was developed with a single-mix experiment involving 8 µM MP_{Olet} with deuterated eicosanoic acid prepared as above and loaded into Syringe A. Syringe B was loaded with 10 mM hydrogen peroxide. PMT data at the 430 nm wavelength, associated with the decay of Compound I to Compound II and the decay of Compound II to low-spin, were collected at three second intervals at a temperature range from 2^oC to 23^oC. The rates were plotted as a function of ln(k) vs 1/T in Kelvin. The activation energy was determined with the Arrhenius equation $k=Ae\text{^}-(E_a/RT)$, where k is the rate of the decay from either Cpd. I to Cpd. II or Cpd. II to low-spin, A is a multivariable parameter that contains distance to the substrate, E_a is the activation energy necessary to proceed to the next intermediate, R is the ideal gas constant in kcal/mol, and T is the temperature in Kelvin.

Determination of turnover products

Turnover products were measured with a Hewlitt-Packard 5890 Series II Gas Chromatography (GC) instrument featuring a 30 m DB-5ms column with a column head pressure ranging between 7 and 15 psi and fitted with a flame ion detector. For chain lengths greater than C16, the protocol is as follows: 3 minutes at 170°C, 5°C/min to 260°C, 10°C/min to 320°C, 2 minutes at 320°C. For chain lengths less than C16, the protocol is as follows: 3 minutes at 50°C, 5°C/min to 170°C, 10°C/min to 280°C, 3 minutes at 280°C. The turnover experiment involved 2 mL of 5 µM untreated protein + 500 µM of proteated fatty acid (C20, C16, C14, and C12) in a flat-bottom glass vial. While stirring at room temperature, a 5 mM solution of hydrogen peroxide was slowly titrated using a multichannel pipettor at a rate of 2 mL/hr. After one hour, the titration was stopped and the solution stirred for an additional 10 minutes. Four drops of 12 M HCl were mixed for 5 minutes in each vial to aggregate the protein and protonate the fatty acid.

The fatty acid was extracted using an equivalent volume of chloroform, vortexed for 1 minute, and spun down for 3 minutes at 2200 rpm. The organic layer was collected, transferred to a separate vial, and evaporated on ice under nitrogen gas. The extracted material was derivatized with 200 µL BSTFA:TCMS (Sigma-Aldrich) at a 99:1 ratio and incubated at 60°C for 1 hour. 7 µL of the derivatized contents were injected onto the GC with the program dependent on the fatty acid chain length. Samples were stored at -20^{o}C until shot to prevent degradation of the derivatized products. The data for the chromatographs were collected and peaks integrated on proprietary software from Hewlitt-Packard.

4.3 RESULTS

Characterization by UV-Vis

Post-purification, all peaks for MPolet associated with π-π* transitions are hypsochromically shifted by 10 nm, leading to a Soret band at 408 nm, high-spin band at 382nm, and α/β Q-bands at 565 nm and 530 nm, respectively. In addition, there is a 10 nm shift for the Soret and Q-bands for the ferric, low-spin, ferrous, and ferrous-CO complex in MPolet (Figure 4.3) when compared to PPolet (Figure 4.4). This is similar to the spectral shift with MPIX incorporation into horseradish peroxidase, which also observes a hypsochromic shift in these peaks [47]. The formation of the ferrous spectrum is similar to PPolet as well, again with peak maxima blue-shifted by 10 nm to 402 nm. There is difficulty with the shift from the ferric state to the ferrous state, with 3 molar equivalents of sodium dithionite to successfully reduce the sample. This may be due to an equilibration issue among the electron exchange that is not present with PPolet, but common among NADPH and surrounding redox partners [48] or the lengthy equilibration times for P450 BM3 redox potentiometry [49]. The formation of the carbon monoxide complex shows a uniform peak centered at 442 nm with no indication of accumulation at 450 nm, which is the wavelength of the CO complex with PPolet. The Q-bands merge to form a single band, which indicates an iron-thiolate ligand present in the sample. This intermediate is short lived as the sample quickly decays from 442 nm to 410 nm, which corresponds to a 10 nm difference observed by PPolet for a severed iron-thiolate bond and catalytically inert enzyme [50-52].

The quantity of high-spin present post-purification is about 40%, which is lower than the 50% for PPolet. The co-purification of substrate is not specific to P450 peroxidases [53], but the low K_D of long chain fatty acid provides an estimate concerning the molecule in the active site. Although the enzyme does not purify in an entirely high-spin state, two days of purification in continuously fresh buffer undoubtedly rids a portion of the fatty acid from the enzyme preparation. Upon the addition of excess eicosanoic acid, the spin-state shifts to about 80% high-spin, which is around 10%-15% less than PPolet. However, the dissociation constant for the MPolet/C20 pair is similarly low at 112 nM (Figure 4.5). This supports that the porphyrin is properly seated and not in a position to influence binding of the fatty acid. The high-spin transition also shows an alteration in the Q-bands which are similar to PPolet with a blue-shift of 10 nm. This may infer that lowering the potential increases the stability of the water ligand attached to the Fe-MPIX, leading to difficulty in transitioning to a high-spin state. Association have been reported between enzymes with lower potential and the accumulation of high-spin, notably forming a decreased amount of high-spin with respect to the decrease in potential [54, 55].

The hemochromagen assay shows no significant amount of Fe-PPIX present in the folded protein (Figure 4.6). The Q-bands show a small peak at

522 nm with a larger peak at 566 nm for PPolet, whereas there is a splitting of two peaks at 506 and 518 nm with a larger peak at 546 nm. The reason for the splitting of the β-band is unclear, but the 20 nm difference for the α-band may be due to the loss of the thiol ligand after treatment with pyridine. In addition, the absorbance ratios for the proteins as-purified ($A_{408/280} \approx 1.0$ for MPolet and $A_{418/280} \approx 1.2$ for PPolet) are equivalent, indicating that there is little, if any, non-Fe-MPIX bound enzyme in solution. This also confirms that there were no issues concerning bacterial uptake of the porphyrin or difficulty with incorporation of the non-native porphyrin into the enzyme. The distinct separation between the α and β Q-bands also assist in confirming the absence of Fe-PPIX, since a mixture would likely merge the bands into a single signal rather than two distinct features. To ensure the protein folded correctly and confirm that the reduction of the vinyl groups did not interfere with seating in the enzyme active site, spectra were taken using Circular Dichroism which displayed no significant differences between PPolet and MPolet (Figure 4.7).

Identification of intermediate species for Meso-Olet

The addition of a 300-fold excess of hydrogen peroxide led to the formation of a ferryl-oxo Soret for Compound I at 357 nm and the formation of a π-cation radical at 685 nm, the latter observed to blue-shift by 5 nm instead of the 10 nm observed in every other peak (Figure 4.8). The origin of the π-cation radical may be from a transition between the π-orbital and the cationic σ-orbital, so the wavelength shift is not comparable to the $\pi \rightarrow \pi^*$ transitions present in the other peaks [56]. The lack of an Fe-PPIX absorbance band in the hemochromagen spectrum shows that the total formation of the Cpd. I intermediate is from MPolet, so no contributions needed to be subtracted out. The kinetic isotope effect (KIE) of K_H/K_D in the presence of eicosanoic acid gives a value of ~18, which is higher compared to other P450 enzymes and $PP_{Olet,}$ whose KIE is 8.1 with C20 fatty acid [30], CYP101A1 = 3.8 with norcamphor [57], and HRP B-C = 10.1 with N-methylaniline [58]. The high KIE concludes that the hydrogen abstraction step is the rate-limiting step in the reaction of MPolet with fatty acid. A plot of Cpd. I decay in MPolet from the first kinetic rate measured at 428 nm at different concentrations of hydrogen peroxide gives a dissociation constant for hydrogen peroxide of 70 µM, a similar value found for PPolet (Figure 4.9). The absence of significant differences conclude that the sidechains involved with stabilizing the hydrogen peroxide (H85 and R245) are not displaces and are still within a reasonable distance to the distal oxygen of the peroxide for an interaction to occur.

The total accumulation of Cpd. I is greater with MPolet than PPolet, indicating a difference between the two proteins in the activation energy (E_a) of this intermediate. This is verified through Arrhenius measurements, which gives an E_a=15 kcal/mol for MPolet, around twice the energetic barrier of 7 kcal/mol present in PPolet (Figure 4.10). Both of these barriers are high compared to HRP, which has a calculated E_a=3.5 kcal/mol [59] but the values match CYP119 bound with benzyl alcohol, which has an E_a=15.1 kcal/mol [60]. Interestingly, the total accumulation of Cpd. I at 1 ms is about the same at both 4°C and 23°C, indicating the presence of a highly stable Cpd. I intermediate. All rates and fittings are present in Figure 4.11 and Table 4.1 below and applies for all rate data shown hereafter for MPolet and PPolet. In addition, the rate of Cpd I decay for MPolet is 30 s^{-1}, about 2.5x slower than PPolet at 75 s^{-1}. These Cpd. I decay rates are quicker than the rate of 9 s^{-1} calculated by Rittle for CYP119 [31] or 29.4 s^{-1} calculated by Kellner for CYP119 [61]. The presence of the thiolate ligand does make the intermediate react quicker than the more catalytically stable Hemoglobin I, which has a rate of 0.03 s^{-1} [62]. These data conclude that MPolet has a more stable Cpd I intermediate than PPolet.

The decay of Cpd. I coincides with the formation of the Cpd. II intermediate. The Soret is centered at 422 nm and appears as a shoulder to the low-spin form of the enzyme but has smaller absorbance due to a lower extinction coefficient compared to the ferric, low-spin species. The appearance of the Q-bands is similar to the low-spin form of the enzyme while the hyperporphyrin absorbance increases at 350 nm. The decay of the Cpd. II species back to low-spin is equivalent to, although slightly faster than, the rate of PP_{Olet} Cpd. II decay of 10 s^{-1}. This rate is quicker than myeloperoxidase Cpd. II decay, which has a rate of 0.0008 s^{-1} [63], but there are not many examples of Cpd. II accumulation, much less decay rates back to the ferric state. However, Meso-Olet has a slightly lower E_a for the formation of Compound II, resting at 15 kcal/mol instead of 18 kcal/mol. The combination of the rate of Cpd. II decay and the lower activation energy gives an explanation for the increased quantity of hydroxylated fatty acid present for fatty acid chain lengths < 18.

Turnover of Meso-Olet with variable chain length fatty acids

All reported turnover data are present in Table 4.2 below, with contributions for all PPolet data from Jose Amaya and Cooper Rutland. The percent product conversion for MPolet is around 20% lower than with PPolet, possibly due to the higher energy barrier for hydrogen abstraction from the substrate. A similar dip in product conversions were observed with the conversion of arginine to citrulline by MP_{NOS}, which also showed a decrease of 14% in product distribution [17]. However, both MPolet and PPolet show exclusive conversion of eicosanoic acid to C19 alkene and carbon dioxide, inferring that the amount of alkene observed is greater than 99% for C18 and higher for both MPolet and PPolet. This exclusive creation of alkene for C20 fatty acid is also observed for a variety of mutants [64] and homologs, specifically P450staph (data not shown). As the chain length of the fatty acid shortens below C18, the amount of alkene produced decreases, compensated by an increase in the production of hydroxylated fatty acid. MPolet produces primarily β-OH fatty acid followed by γ-OH and finally α-OH products. This partially mimics the product preferences for PPolet, as β-OH is the primary hydroxylated product followed by α-OH, although previously published work did not indicate the presence of γ-OH fatty acid [64]. For all fatty acid chain lengths, there were no observable products outside of the alkene and three hydroxylated products for the MPolet construct. It is currently unclear why this change in product distribution occurred, given that alteration of the porphyrin should not interfere with the binding behavior of the fatty acid or the activation/orientation of the hydrogen peroxide oxidant.

4.4 DISCUSSION

The potential use of PPolet as a biosynthetic catalyst for the creation of alkene-based biofuels has been studied for several years. One deviation from ongoing research that has not garnered much attention is determining how much of an effect the electronics of the porphyrin itself regulate the product distribution of the enzyme, with a primary reason stemming from the difficulty of incorporating non-native porphyrins into the protein scaffold. This traditionally was accomplished by growing the culture under a strictly anaerobic environment with RP523 cells, which allowed the passage of non-native porphyrins and contains a knockout for native porphyrin production. Attempts to express protein in this cell line yielded low pellet weight due to excess cell death, presumably from oxygen leakage during protein expression. However, the use of ChuA provides a cheap and facile alternative for the incorporation of porphyrins while growing the culture aerobically.

Fe-MPIX has a redox potential that is about mV lower than Fe-PPIX due to the absence of additional resonance stabilization provided by the vinyl groups into the porphyrin ring. This leads to a hypsochromic shift in the $\pi \rightarrow \pi^*$ absorbance bands by 10 nm. However, the activation of hydrogen peroxide is not affected, with the K_D and K_{off} rates are similar to PPolet. Reports describing MPIX substitution in monooxygenase enzymes show changes in the K_D of molecular oxygen. For instance, substitution of Fe-MPIX into CYP101A1 led to an increase in the rate of autoxidation [65], but there is no evidence this applies to peroxide activation.

The formation of Cpd. I with MPolet is likely accompanied by a decrease in basicity and increased difficulty for the ferryl-oxo to proceed with the hydrogen abstraction from the substrate. The addition of deuterated substrate and excess hydrogen peroxide leads to equivalent accumulations of Cpd. I observed at 2ºC as 23ºC, but the reasons for this stability are unknown. One explanation may lie in the Arrhenius value for the E_a for decay to Cpd. II being 12 kcal/mol for MPolet, a higher value than 7.2 kcal/mol for PPolet. The higher temperature would allow the Cpd. I intermediate to be more stable at higher temperatures for MPolet. Also, the total conversion of fatty acid to product is lower than with PPolet, possibly due to this longer lifespan of the Cpd. I intermediate at 25ºC. This subsequently increases the amount of time that substrate or product is in the active site. In addition, studies of the kinetic isotope effects show that MPolet has a KIE (k_H/k_D) ≈ 18 compared to a KIE of ~7 observed in PPolet. Both values are suggestive that the method of hydrogen abstraction mechanistically lies in an electron tunneling event rather than a traditional proton transfer. However, tunneling cannot overcome the decrease in the redox potential of the system and this corresponds to a longer-lived Cpd. I.

Although the rate of Cpd. I decay for Cpd. I is higher in MPolet than it is for PPolet, the rate of decay for Cpd. II back to ferric, low-spin is similar, with MPolet exhibiting a rate of 15 kcal/mol compared to 18 kcal/mol for PPolet. This is reflected by the lower ratio of alkene to hydroxylated product observed during turnover experiments, as the rebound efficiency would increase slightly. However, there does not be a rearrangement of hydroxylated products with

MPolet, with the dictation of ratios showing a greater percentage of β-OH products followed by γ-OH and α-OH. Since the position of hydroxylation should not be determined by the porphyrin but rather by the residues in the distal pocket, this infers the porphyrin is not improperly seated and does not lead to a shift in the binding motif of any fatty acid substrates.

The enzyme allows the entry of MPIX, but rejects the incorporation of diformyl-deuteroporphyrin IX (df-DPIX). According to the structural analysis of PPolet from a published structure of the protein (PDBID #4L54), multiple phenylalanine residues on the protein scaffold are positioned in a manner to reject the transformation of the vinyl group at the 4 position into a polar functional group, as this would prevent the porphyrin from seating correctly. However, reduction of a 2,4-divinyl protoporphyrin to a 2,4-diethyl protoporphyrin has no deleterious effect on its incorporation into the protein *in vivo*. This reinforces the importance of the local environment when choosing specific porphyrin derivatives to introduce into the active site of a P450, although porphyrins with polar substituents at the 2,4 positions have been successfully implemented into histidine-ligated proteins, such as myoglobin [9] and HRP [47].

4.5 CONCLUSION

Attempts to form alternative products for P450olet conclude that methods must move beyond tuning the electronics of the porphyrin. The shift in the redox potential for MPolet creates a greater amount of hydroxylated product, but there are no observable changes upon reduction of the two vinyl groups, with all possible products similar to PPolet. The sole product in the presence of eicosanoic acid is the C19 alkene while the percent turnover of fatty acid for all chain lengths is lower than with PPolet, possibly due to the prolonged stability of Cpd. I observable at room temperature, leading to longer time to perform a single turnover.

4.6 REFERENCES

[1] Rhie, G., Avissar, Y. J., and Beale, S. I. (1996) Structure and expression of the Chlorobium vibrioforme hemB gene and characterization of its encoded enzyme, porphobilinogen synthase, *J Biol Chem 271*, 8176-8182.

[2] Woodward, J. J., Martin, N. I., and Marletta, M. A. (2007) An Escherichia coli expression-based method for heme substitution, *Nat Methods 4*, 43-45.

[3] Sudhamsu, J., Kabir, M., Airola, M. V., Patel, B. A., Yeh, S. R., Rousseau, D. L., and Crane, B. R. (2010) Co-expression of ferrochelatase allows for complete heme incorporation into recombinant proteins produced in E. coli, *Protein Expr Purif 73*, 78-82.

[4] Winter, M. B., Klemm, P. J., Phillips-Piro, C. M., Raymond, K. N., and Marletta, M. A. (2013) Porphyrin-Substituted H-NOX Proteins as High-Relaxivity MRI Contrast Agents, *Inorg Chem 52*, 2277-2279.

[5] Winter, M. B., McLaurin, E. J., Reece, S. Y., Olea, C., Jr., Nocera, D. G., and Marletta, M. A. (2010) Ru-porphyrin protein scaffolds for sensing O2, *J Am Chem Soc 132*, 5582-5583.

[6] Varnado, C. L., and Goodwin, D. C. (2004) System for the expression of recombinant hemoproteins in Escherichia coli, *Protein Expr Purif 35*, 76-83.

[7] Lelyveld, V. S., Brustad, E., Arnold, F. H., and Jasanoff, A. (2011) Metal-Substituted Protein MRI Contrast Agents Engineered for Enhanced Relaxivity and Ligand Sensitivity, *J Am Chem Soc 133*, 649-651.

[8] Villarreal, D. M., Phillips, C. L., Kelley, A. M., Villarreal, S., Villaloboz, A., Hernandez, P., Olson, J. S., and Henderson, D. P. (2008) Enhancement of recombinant hemoglobin production in Escherichia coli BL21(DE3) containing the Plesiomonas shigelloides heme transport system, *Appl Environ Microbiol 74*, 5854-5856.

[9] Bhagi-Damodaran, A., Petrik, I. D., Marshall, N. M., Robinson, H., and Lu, Y. (2014) Systematic tuning of heme redox potentials and its effects on O2 reduction rates in a designed oxidase in myoglobin, *J Am Chem Soc 136*, 11882-11885.

[10] Sono, M., and Asakura, T. (1975) Decrease in oxygen affinity of myoglobin by formylation of vinyl groups of heme, *J Biol Chem 250*, 5227-5232.

[11] Neya, S., Imai, K., Hori, H., Ishikawa, H., Ishimori, K., Okuno, D., Nagatomo, S., Hoshino, T., Hata, M., and Funasaki, N. (2003) Iron hemiporphycene as a functional prosthetic group for myoglobin, *Inorg Chem 42*, 1456-1461.

[12] Gisselbrecht, J. P., Gross, M., Vogel, E., Scholz, P., Broring, M., and Sessler, J. L. (2001) Redox properties of hemiporphycene and

isoporphycene - Comparison with those of porphyrin and other porphyrin isomers, porphycene and corrphycene, *J Electroanal Chem 507*, 244-249.

[13] Mus-Veteau, I., Dolla, A., Guerlesquin, F., Payan, F., Czjzek, M., Haser, R., Bianco, P., Haladjian, J., Rapp-Giles, B. J., Wall, J. D., and et al. (1992) Site-directed mutagenesis of tetraheme cytochrome c3. Modification of oxidoreduction potentials after heme axial ligand replacement, *J Biol Chem 267*, 16851-16858.

[14] Raphael, A. L., and Gray, H. B. (1989) Axial ligand replacement in horse heart cytochrome c by semisynthesis, *Proteins 6*, 338-340.

[15] Moore, G. R., and Williams, R. J. (1977) Structural basis for the variation in redox potential of cytochromes, *FEBS Lett 79*, 229-232.

[16] Lee, K. B., Jun, E. S., Lamar, G. N., Rezzano, I. N., Pandey, R. K., Smith, K. M., Walker, F. A., and Buttlaire, D. H. (1991) Influence of Heme Vinyl-Protein and Carboxylate Protein Contacts on Structure and Redox Properties of Bovine Cytochrome-B5, *J Am Chem Soc 113*, 3576-3583.

[17] Woodward, J. J., Chang, M. M., Martin, N. I., and Marletta, M. A. (2009) The Second Step of the Nitric Oxide Synthase Reaction: Evidence for Ferric-Peroxo as the Active Oxidant, *J Am Chem Soc 131*, 297-305.

[18] Hunter, G. A., Sampson, M. P., and Ferreira, G. C. (2008) Metal ion substrate inhibition of ferrochelatase, *J Biol Chem 283*, 23685-23691.

[19] Sigman, J. A., Kim, H. K., Zhao, X., Carey, J. R., and Lu, Y. (2003) The role of copper and protons in heme-copper oxidases: kinetic study of an

engineered heme-copper center in myoglobin, *Proc Natl Acad Sci U S A 100*, 3629-3634.

[20] Aguirre, J. D., and Culotta, V. C. (2012) Battles with iron: manganese in oxidative stress protection, *J Biol Chem 287*, 13541-13548.

[21] Hennig, B., and Neupert, W. (1981) Assembly of cytochrome c. Apocytochrome c is bound to specific sites on mitochondria before its conversion to holocytochrome c, *Eur J Biochem 121*, 203-212.

[22] Rude, M. A., Baron, T. S., Brubaker, S., Alibhai, M., Del Cardayre, S. B., and Schirmer, A. (2011) Terminal olefin (1-alkene) biosynthesis by a novel p450 fatty acid decarboxylase from Jeotgalicoccus species, *Appl Environ Microbiol 77*, 1718-1727.

[23] Ogliaro, F., Harris, N., Cohen, S., Filatov, M., de Visser, S. P., and Shaik, S. (2000) A model "rebound" mechanism of hydroxylation by cytochrome P450: Stepwise and effectively concerted pathways, and their reactivity patterns, *J Am Chem Soc 122*, 8977-8989.

[24] He, X., and de Montellano, P. R. (2004) Radical rebound mechanism in cytochrome P-450-catalyzed hydroxylation of the multifaceted radical clocks alpha- and beta-thujone, *J Biol Chem 279*, 39479-39484.

[25] Guengerich, F. P. (2007) Mechanisms of cytochrome P450 substrate oxidation: MiniReview, *J Biochem Mol Toxicol 21*, 163-168.

[26] Poulos, T. L., Finzel, B. C., and Howard, A. J. (1987) High-resolution crystal structure of cytochrome P450cam, *J Mol Biol 195*, 687-700.

[27] Belcher, J., McLean, K. J., Matthews, S., Woodward, L. S., Fisher, K., Rigby, S. E., Nelson, D. R., Potts, D., Baynham, M. T., Parker, D. A., Leys, D., and Munro, A. W. (2014) Structure and biochemical properties of the alkene producing cytochrome P450 OleTJE (CYP152L1) from the Jeotgalicoccus sp. 8456 bacterium, *J Biol Chem 289*, 6535-6550.

[28] Prasad, S., and Mitra, S. (2004) Substrate modulates compound I formation in peroxide shunt pathway of Pseudomonas putida cytochrome P450(cam), *Biochem Bioph Res Co 314*, 610-614.

[29] Tajima, K. (1989) A Possible Model of a Hemoprotein Hydrogen-Peroxide Complex, *Inorg Chim Acta 163*, 115-122.

[30] Grant, J. L., Mitchell, M. E., and Makris, T. M. (2016) Catalytic strategy for carbon-carbon bond scission by the cytochrome P450 OleT, *Proc Natl Acad Sci U S A 113*, 10049-10054.

[31] Rittle, J., and Green, M. T. (2010) Cytochrome P450 compound I: capture, characterization, and C-H bond activation kinetics, *Science 330*, 933-937.

[32] Auclair, K., Hu, Z., Little, D. M., Ortiz De Montellano, P. R., and Groves, J. T. (2002) Revisiting the mechanism of P450 enzymes with the radical clocks norcarane and spiro[2,5]octane, *J Am Chem Soc 124*, 6020-6027.

[33] Faponle, A. S., Quesne, M. G., and de Visser, S. P. (2016) Origin of the Regioselective Fatty-Acid Hydroxylation versus Decarboxylation by a Cytochrome P450 Peroxygenase: What Drives the Reaction to Biofuel Production?, *Chemistry 22*, 5478-5483.

[34] Whitehouse, C. J., Bell, S. G., and Wong, L. L. (2008) Desaturation of alkylbenzenes by cytochrome P450(BM3) (CYP102A1), *Chemistry 14*, 10905-10908.

[35] Skiles, G. L., and Yost, G. S. (1996) Mechanistic studies on the cytochrome P450-catalyzed dehydrogenation of 3-methylindole, *Chem Res Toxicol 9*, 291-297.

[36] Zhu, D., Seo, M. J., Ikeda, H., and Cane, D. E. (2011) Genome mining in streptomyces. Discovery of an unprecedented P450-catalyzed oxidative rearrangement that is the final step in the biosynthesis of pentalenolactone, *J Am Chem Soc 133*, 2128-2131.

[37] Hsieh, C. H., Huang, X., Amaya, J. A., Rutland, C. D., Keys, C. L., Groves, J. T., Austin, R. N., and Makris, T. M. (2017) The Enigmatic P450 Decarboxylase OleT Is Capable of, but Evolved To Frustrate, Oxygen Rebound Chemistry, *Biochemistry-Us*.

[38] Lee, D. S., Yamada, A., Sugimoto, H., Matsunaga, I., Ogura, H., Ichihara, K., Adachi, S., Park, S. Y., and Shiro, Y. (2003) Substrate recognition and molecular mechanism of fatty acid hydroxylation by cytochrome P450 from Bacillus subtilis. Crystallographic, spectroscopic, and mutational studies, *J Biol Chem 278*, 9761-9767.

[39] Matsunaga, I., Ueda, A., Fujiwara, N., Sumimoto, T., and Ichihara, K. (1999) Characterization of the ybdT gene product of Bacillus subtilis: novel fatty acid beta-hydroxylating cytochrome P450, *Lipids 34*, 841-846.

[40] Fujishiro, T., Shoji, O., Nagano, S., Sugimoto, H., Shiro, Y., and Watanabe, Y. (2011) Crystal structure of H2O2-dependent cytochrome P450SPalpha with its bound fatty acid substrate: insight into the regioselective hydroxylation of fatty acids at the alpha position, *J Biol Chem 286*, 29941-29950.

[41] Uyama, H., Kuwabara, M., Tsujimoto, T., and Kobayashi, S. (2003) Enzymatic synthesis and curing of biodegradable epoxide-containing polyesters from renewable resources, *Biomacromolecules 4*, 211-215.

[42] Sligar, S. G., and Gunsalus, I. C. (1976) A thermodynamic model of regulation: modulation of redox equilibria in camphor monoxygenase, *Proc Natl Acad Sci U S A 73*, 1078-1082.

[43] Kimmich, N., Das, A., Sevrioukova, I., Meharenna, Y., Sligar, S. G., and Poulos, T. L. (2007) Electron transfer between cytochrome p450cin and its FMN-containing redox partner, cindoxin, *J Biol Chem 282*, 27006-27011.

[44] Smith, E. T., and Feinberg, B. A. (1990) Redox Properties of Several Bacterial Ferredoxins Using Square-Wave Voltammetry, *J Biol Chem 265*, 14371-14376.

[45] Grant, J. L., Hsieh, C. H., and Makris, T. M. (2015) Decarboxylation of fatty acids to terminal alkenes by cytochrome P450 compound I, *J Am Chem Soc 137*, 4940-4943.

[46] Barr, I., and Guo, F. (2015) Pyridine Hemochromagen Assay for Determining the Concentration of Heme in Purified Protein Solutions, *Bio Protoc 5*.

[47] Makino, R., and Yamazaki, I. (1972) Effects of 2,4-Substituents of Deuterohemin Upon Peroxidase Functions .1. Preparation and Some Properties of Artificial Enzymes, *J Biochem-Tokyo 72*, 655-&.

[48] Gutierrez, A., Lian, L. Y., Wolf, C. R., Scrutton, N. S., and Roberts, G. C. (2001) Stopped-flow kinetic studies of flavin reduction in human cytochrome P450 reductase and its component domains, *Biochemistry 40*, 1964-1975.

[49] Coelho, P. S., Wang, Z. J., Ener, M. E., Baril, S. A., Kannan, A., Arnold, F. H., and Brustad, E. M. (2013) A serine-substituted P450 catalyzes highly efficient carbene transfer to olefins in vivo, *Nat Chem Biol 9*, 485-487.

[50] Bui, S. H., McLean, K. J., Cheesman, M. R., Bradley, J. M., Rigby, S. E., Levy, C. W., Leys, D., and Munro, A. W. (2012) Unusual spectroscopic and ligand binding properties of the cytochrome P450-flavodoxin fusion enzyme XplA, *J Biol Chem 287*, 19699-19714.

[51] Chenge, J. T., Duyet, L. V., Swami, S., McLean, K. J., Kavanagh, M. E., Coyne, A. G., Rigby, S. E. J., Cheesman, M. R., Girvan, H. M., Levy, C. W., Rupp, B., von Kries, J. P., Abell, C., Leys, D., and Munro, A. W. (2017) Structural Characterization and Ligand/Inhibitor Identification Provide Functional Insights into the Mycobacterium tuberculosis Cytochrome P450 CYP126A1, *J Biol Chem 292*, 1310-1329.

[52] McLean, K. J., Warman, A. J., Seward, H. E., Marshall, K. R., Girvan, H. M., Cheesman, M. R., Waterman, M. R., and Munro, A. W. (2006) Biophysical characterization of the sterol demethylase P450 from Mycobacterium

tuberculosis, its cognate ferredoxin, and their interactions, *Biochemistry 45*, 8427-8443.

[53] Lee, C. W., Lee, J. H., Rimal, H., Park, H., Lee, J. H., and Oh, T. J. (2016) Crystal Structure of Cytochrome P450 (CYP105P2) from Streptomyces peucetius and Its Conformational Changes in Response to Substrate Binding, *Int J Mol Sci 17*, 813.

[54] Wise, C. E., and Makris, T. M. (2017) Recruitment and Regulation of the Non-ribosomal Peptide Synthetase Modifying Cytochrome P450 Involved in Nikkomycin Biosynthesis, *ACS Chem Biol 12*, 1316-1326.

[55] Rein, H., Ristau, O., Blanck, J., and Ruckpaul, K. (1989) The Spin-Redox Couple as Regulator of the Catalytic Activity of Cytochrome-P-450, *Arch Biochem Biophys*, 284-287.

[56] Li, Z. H., Liu, J. L., Qiao, M. H., and Fan, K. N. (2009) A theoretical study on the metal cation-pi complexes of Zn2+ and Cd2+ with benzene and cyclohexene, *Mol Phys 107*, 1271-1282.

[57] Atkins, W. M., and Sligar, S. G. (1987) Metabolic Switching in Cytochrome-P-450cam - Deuterium-Isotope Effects on Regiospecificity and the Monooxygenase Oxidase Ratio, *J Am Chem Soc 109*, 3754-3760.

[58] Miwa, G. T., Walsh, J. S., Kedderis, G. L., and Hollenberg, P. F. (1983) The Use of Intramolecular Isotope Effects to Distinguish between Deprotonation and Hydrogen-Atom Abstraction Mechanisms in Cytochrome-P-450-Catalyzed and Peroxidase-Catalyzed N-Demethylation Reactions, *J Biol Chem 258*, 4445-4449.

[59] Hewson, W. D., and Dunford, H. B. (1975) Horseradish-Peroxidase .18. Arrhenius Activation-Energy for Formation of Compound-1, *Can J Chem 53*, 1928-1932.

[60] Wang, Q., Sheng, X., Horner, J. H., and Newcomb, M. (2009) Quantitative production of compound I from a cytochrome P450 enzyme at low temperatures. Kinetics, activation parameters, and kinetic isotope effects for oxidation of benzyl alcohol, *J Am Chem Soc 131*, 10629-10636.

[61] Kellner, D. G., Hung, S. C., Weiss, K. E., and Sligar, S. G. (2002) Kinetic characterization of compound I formation in the thermostable cytochrome P450 CYP119, *J Biol Chem 277*, 9641-9644.

[62] De Jesus-Bonilla, W., Cortes-Figueroa, J. E., Souto-Bachiller, F. A., Rodriguez, L., and Lopez-Garriga, J. (2001) Formation of compound I and compound II ferryl species in the reaction of hemoglobin I from Lucina pectinata with hydrogen peroxide, *Arch Biochem Biophys 390*, 304-308.

[63] Galijasevic, S., Saed, G. M., Hazen, S. L., and Abu-Soud, H. M. (2006) Myeloperoxidase metabolizes thiocyanate in a reaction driven by nitric oxide, *Biochemistry 45*, 1255-1262.

[64] Matthews, S., Belcher, J. D., Tee, K. L., Girvan, H. M., McLean, K. J., Rigby, S. E., Levy, C. W., Leys, D., Parker, D. A., Blankley, R. T., and Munro, A. W. (2017) Catalytic Determinants of Alkene Production by the Cytochrome P450 Peroxygenase OleTJE, *J Biol Chem 292*, 5128-5143.

[65] Dolphin, D., James, B. R., and Welborn, H. C. (1980) Oxygenation, and Carbonylation, of a Reduced P450cam Enzyme and Derivatives

Reconstituted with Mesodeuteroheme, Dibromodeuteroheme, and Diacetyldeuteroheme, *J Mol Catal 7*, 201-213.

Figures and Tables

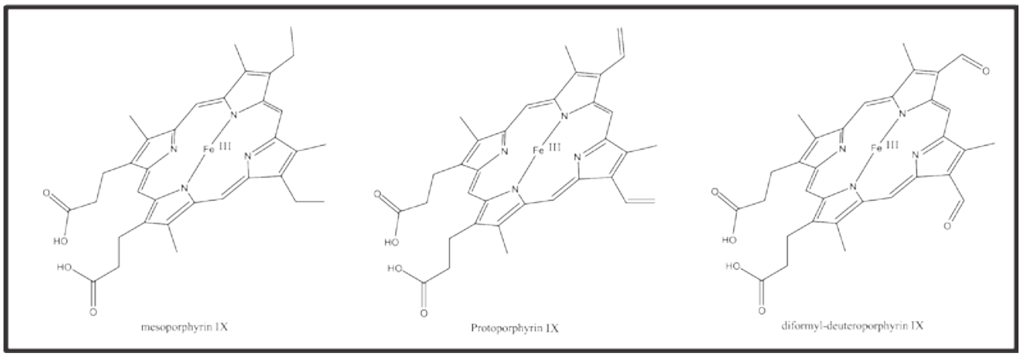

Figure 4.1: Structures of mesoporphyrin IX, protoporphyrin IX, and diformyldeuteroporphyrin IX. Note the aldehyde placements on the diformyl-deuteroporphyrin, which is repelled by the hydrophobic environment of the protein around that 4 position.

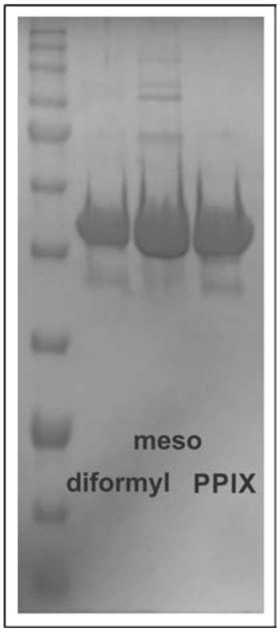

Figure 4.2: 12% SDS-PAGE gel of pure P450olet after dfDPIX, MPIX, and PPIX incorporation. The proteins are pure and express well, but the 2,4 diformylPPolet is a mixture of apo and Fe-PPIX bound.

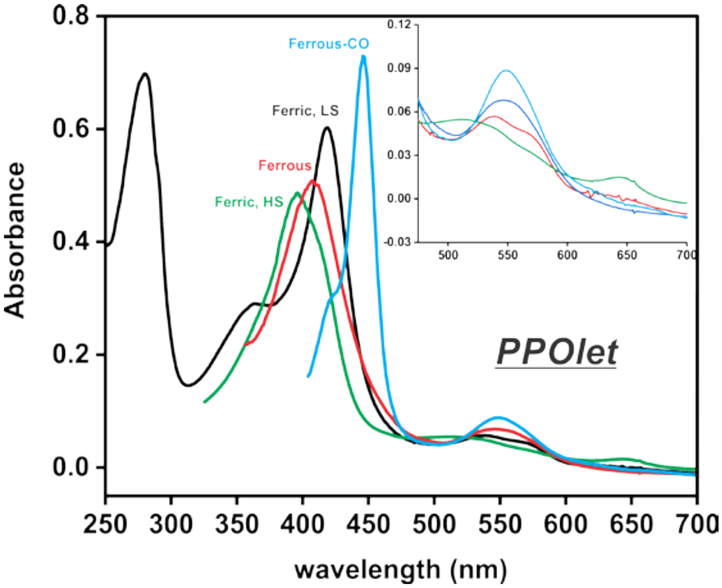

Figure 4.3: Optical characterization of PPolet. The spectra show the ferric, low-spin (black), ferric, high-spin (green), ferrous (red), and ferrous-CO complex (cyan).

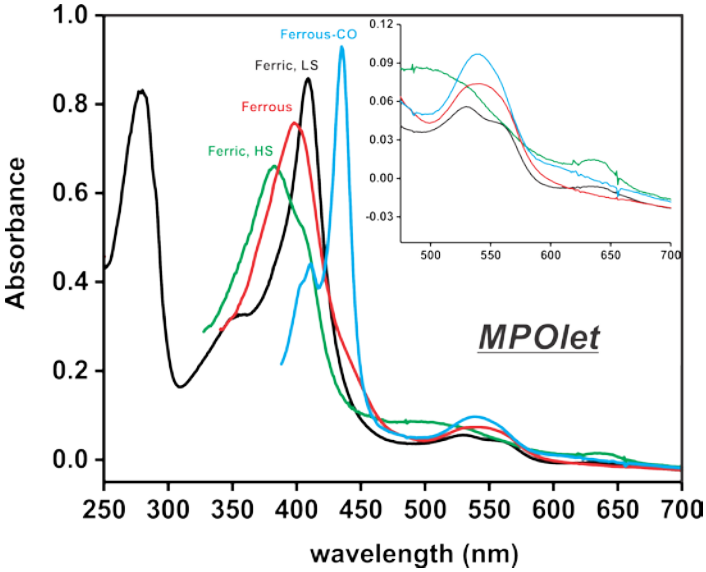

Figure 4.4: Optical characterization of MPolet. The spectra show the ferric, low-spin (black), ferric, high-spin (green), ferrous (red), and ferrous-CO complex (cyan).

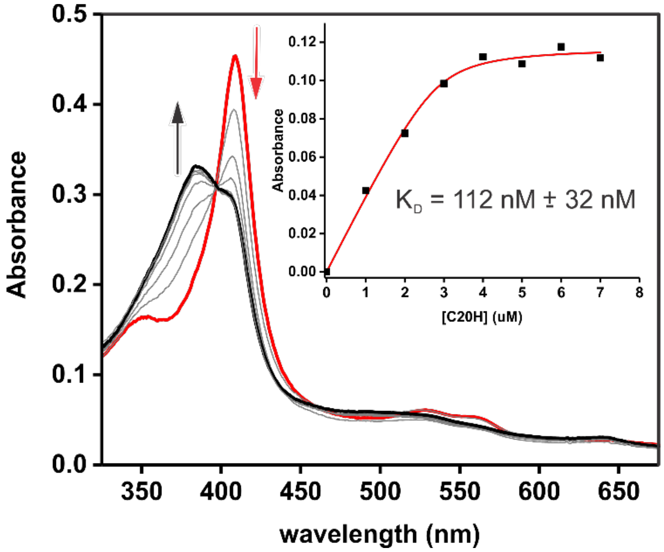

Figure 4.5: Determination of K_D using the optical changes at 417 nm and 396 nm for MPolet. 5 µM ferric, low-spin MPolet was mixed with eicosanoic acid at 1 µM intervals. Fitting the plot with the Morrison equation gives a dissociation constant of 112 nm, similar to the K_D of PPolet.

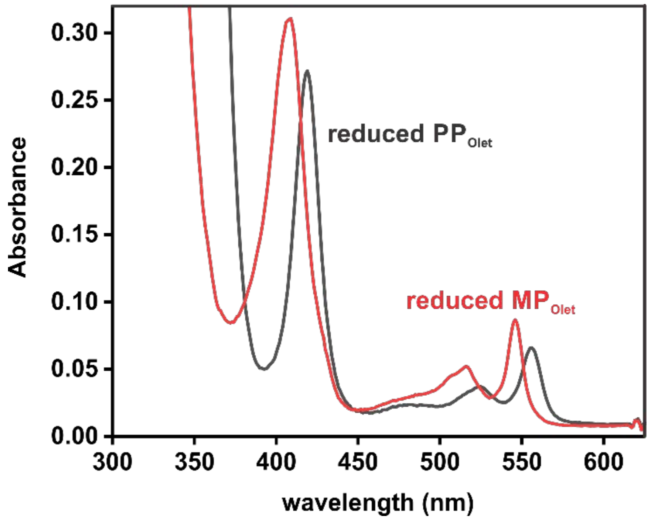

Figure 4.6: Pyridine hemochromagen assay of MPolet and PPolet. The absence of signal at 565 nm for MPolet is an indication there are negligible quantities of Fe-PPIX present in the sample.

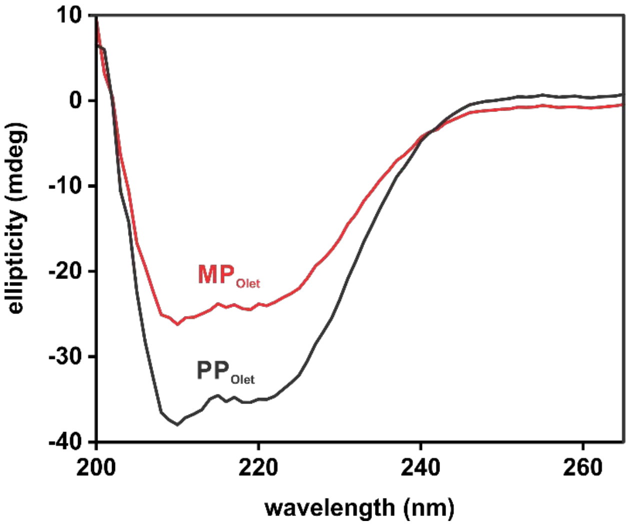

Figure 4.7: CD spectra of purified MPolet and PPolet. This verifies that there is no change in the secondary structure of the construct after incorporation of a non-native porphyrin. The lower absorbance for MPolet is due to the instability of P450olet in the given buffer and disproportionate crashing out between MPolet and PPolet.

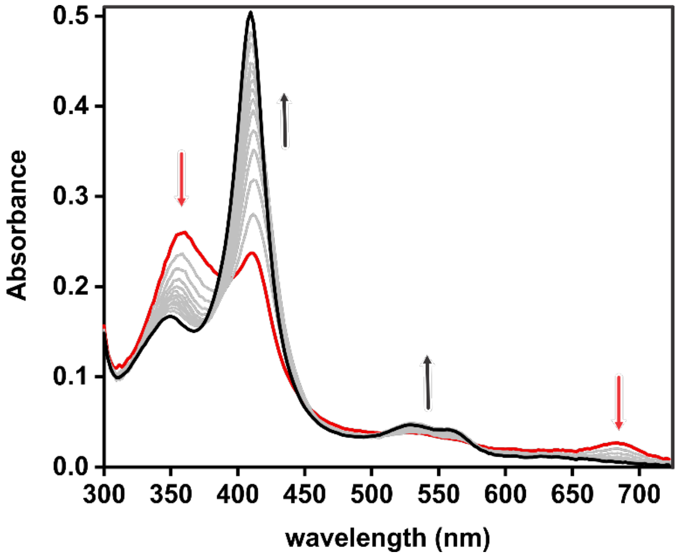

Figure 4.8: Stopped-flow spectra of 10 µM MPolet rapidly mixed against 10 mM hydrogen peroxide. This plot shows the conversion from Cpd. I (red spectrum) to ferric, low-spin (black spectrum) over 1 second with 5 µM MPolet in the presence of 5 mM hydrogen peroxide. Note the presence of the feature at 685 nm indicative of the π-cation of Cpd. I.

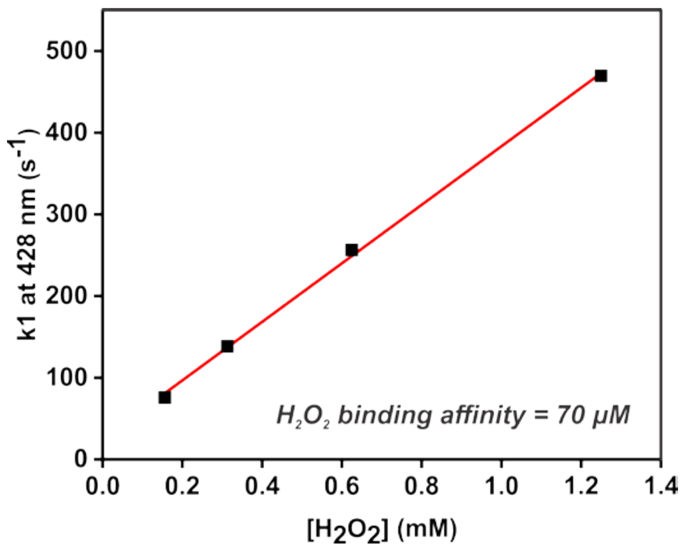

Figure 4.9: Plot of Cpd. I decay as a function of hydrogen peroxide concentration. The initial kinetic rate measured at 428 nm was utilized for this plot at different concentrations of hydrogen peroxide. The slope is 358.2 s^{-1} and the y-intercept is 25.1 mM^{-1} s^{-1}. The dissociation constant of hydrogen peroxide is 70 μM.

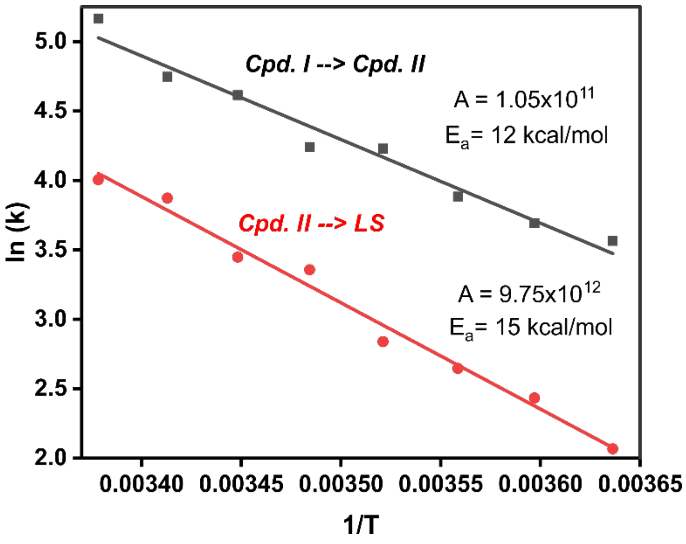

Figure 4.10: Arrhenius plot for Cpd. I and Cpd. II decay. The data was collected at temperature points from 2°C-23°C at 3°C intervals. The activation energy for the decay of Cpd. I (black) is 12 kcal/mol, a higher value than 7 kcal/mol for PPolet. The activation energy (E_a) for the decay of Cpd. II (red) is 15 kcal/mol, a similar value to PPolet. The pre-exponential A values are several orders of magnitude higher than calculated for PPolet.

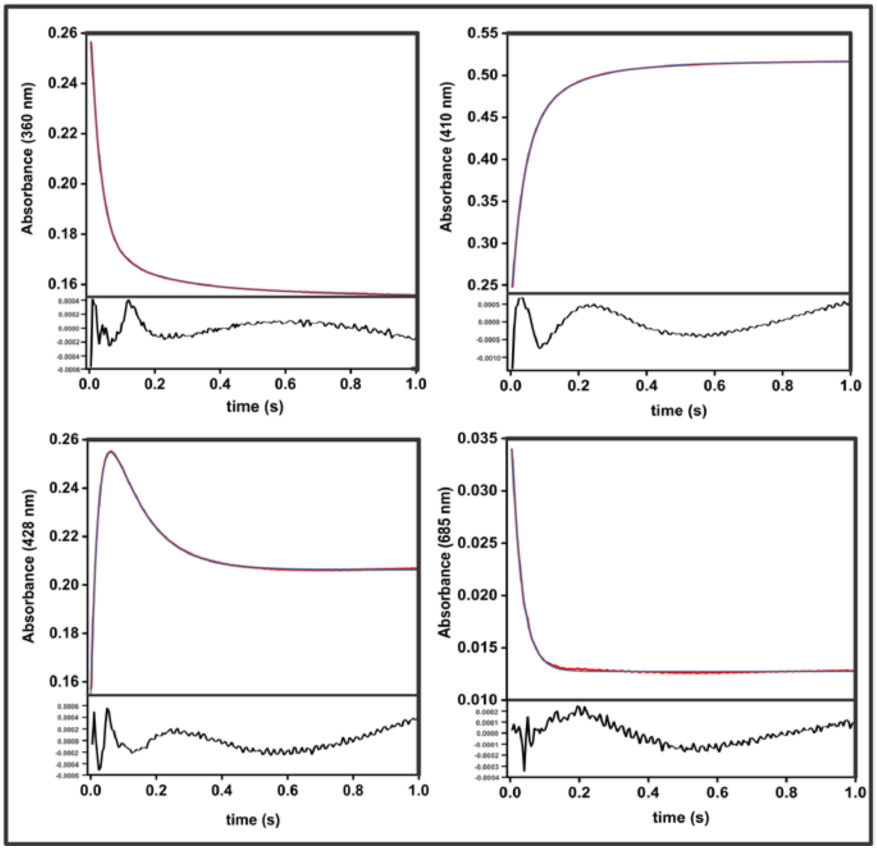

Figure 4.11: Kinetic traces for intermediates formed with 5 µM MPolet with 10 mM hydrogen peroxide. Time traces were taken over a one second time-course and reflect the spectral changes shown in Figure 4.8. Black lines are the collected data and the red lines are the fitting. The residuals are placed below their respective traces. The top left shows the decay of Cpd. I and recorded at its Soret at 360 nm. The top right shows overall formation of ferric, low-spin measured at its Soret at 410 nm. The bottom left shows the formation and decay of Cpd. II measured at 428 nm. The bottom right shows the decay of Cpd. I measured at the π-cation feature at 685 nm.

Table 4.1: Kinetic rates associated with PPolet and MPolet for Cpd. I decay and Cpd. II decay.

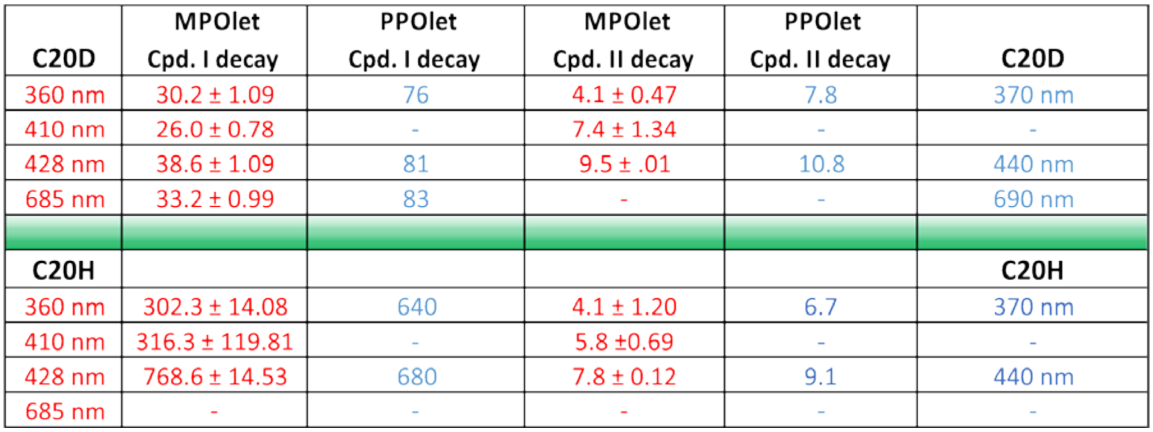

C20D	MPOlet Cpd. I decay	PPOlet Cpd. I decay	MPOlet Cpd. II decay	PPOlet Cpd. II decay	C20D
360 nm	30.2 ± 1.09	76	4.1 ± 0.47	7.8	370 nm
410 nm	26.0 ± 0.78	-	7.4 ± 1.34	-	-
428 nm	38.6 ± 1.09	81	9.5 ± .01	10.8	440 nm
685 nm	33.2 ± 0.99	83	-	-	690 nm
C20H					**C20H**
360 nm	302.3 ± 14.08	640	4.1 ± 1.20	6.7	370 nm
410 nm	316.3 ± 119.81	-	5.8 ±0.69	-	-
428 nm	768.6 ± 14.53	680	7.8 ± 0.12	9.1	440 nm
685 nm	-	-	-	-	-

The PPolet wavelengths and rates are shown in blue and are provided from Jose Amaya and Cooper Rutland. The MPolet wavelengths and rates are shown in red.

Table 4.2: Turnover data for MPolet and PPolet

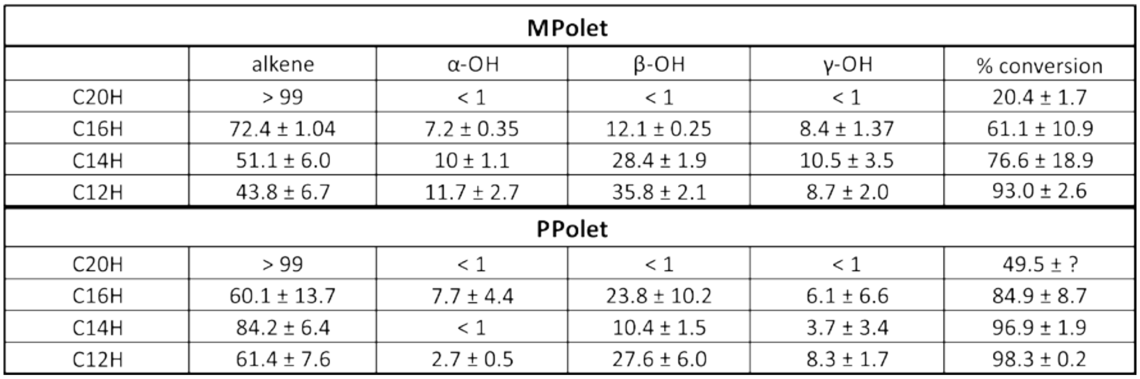

MPolet					
	alkene	α-OH	β-OH	γ-OH	% conversion
C20H	> 99	< 1	< 1	< 1	20.4 ± 1.7
C16H	72.4 ± 1.04	7.2 ± 0.35	12.1 ± 0.25	8.4 ± 1.37	61.1 ± 10.9
C14H	51.1 ± 6.0	10 ± 1.1	28.4 ± 1.9	10.5 ± 3.5	76.6 ± 18.9
C12H	43.8 ± 6.7	11.7 ± 2.7	35.8 ± 2.1	8.7 ± 2.0	93.0 ± 2.6
PPolet					
C20H	> 99	< 1	< 1	< 1	49.5 ± ?
C16H	60.1 ± 13.7	7.7 ± 4.4	23.8 ± 10.2	6.1 ± 6.6	84.9 ± 8.7
C14H	84.2 ± 6.4	< 1	10.4 ± 1.5	3.7 ± 3.4	96.9 ± 1.9
C12H	61.4 ± 7.6	2.7 ± 0.5	27.6 ± 6.0	8.3 ± 1.7	98.3 ± 0.2

MPolet data is derived from this work and data from PPolet is from Amaya and Rutland. Note the lower total conversion for MPolet and the presence of more hydroxylated product for the lower chain lengths.